Spring 1-1-2013

Lattice Dynamics and Thermal Transport Properties of Nanophononic Materials

Bruce Lockwood Davis
University of Colorado at Boulder, bld175@gmail.com

LATTICE DYNAMICS AND THERMAL TRANSPORT PROPERTIES OF NANOPHONONIC MATERIALS

by

BRUCE LOCKWOOD DAVIS

B.S., The Pennsylvania State University, 2006

M.S., The University of Colorado Boulder, 2008

A thesis submitted to the

Faculty of the Graduate School of the

University of Colorado in partial fulfillment

of the requirement for the degree of

Doctor of Philosophy

Department of Aerospace Engineering Sciences

2013

This thesis entitled:

Lattice Dynamics and Thermal Transport Properties of Nanophononic Materials

written by Bruce Lockwood Davis

has been approved for the Department of Aerospace Engineering Sciences

_____

Mahmoud I. Hussein (Chair)

_____

Kurt Maute (Committee Member)

Date_____

The final copy of this thesis has been examined by the signatories, and we find that both the content and the form meet acceptable presentation standards of scholarly work in the above mentioned discipline.

Davis, Bruce L. (Ph.D., Department of Aerospace Engineering Sciences)

Lattice Dynamics and Thermal Transport Properties of Nanophononic Materials

Thesis directed by Mahmoud I. Hussein.

The phenomenon of thermoelectric energy conversion holds great promise in harvesting wasted heat and improving thermal energy management. This technology, however, is not widely used due to its generally poor efficiency stemming from intrinsic material-level limitations. This dissertation proposes to utilize the concepts of phononic crystals and metamaterials at the nanoscale in order to manipulate phonon lattice vibrations in a manner that qualitatively alters the thermal transport mechanisms and improves the thermoelectric energy conversion figure-of-merit. Phononic crystals utilize Bragg scattering while metamaterials use subwavelength properties to manipulate wave propagation in an elastic medium. With the advent of the nanotechnology revolution, the ability to fabricate material systems with nanostructured geometric features renders the concepts promised practically feasible.

First, a Lagrangian formulation is derived to obtain the phonon dispersion spectrum of nanophononic crystals (NPCs) based on a simple three-dimensional mass-spring model. The formulation is then used to examine the opening of frequency band gaps due to the introduction of point-mass lattice defects.

Next, models of silicon utilizing the Tersoff inter-atomic potential are then developed with a focus on investigating the effects of incorporating the full dispersion characteristics of 3D NPCs. The role that dispersion plays in shaping the nonlinear scattering properties as well as the thermal conductivity of the nanostructured material as a whole is thoroughly investigated. The results show that for relatively small voids and void spacing–where boundary scattering is dominant–dispersion at the NPC unit cell level plays a noticeable role in determining the thermal conductivity.

Finally, the focus shifts to 2D thin-films which has significant differences in the phonon band structure and exhibits lower values of thermal conductivity. A thorough modeling scheme is proposed that provides substantially more accurate results compared to the conventional formulation, which uses bulk dispersion in the prediction of the phonon thermal conductivity. The results show that the thin-film full dispersion model better fits with the experimental data over a large temperature range. Finally, features are added to the thin-film forming a nanoscale phononic metamaterial–a novel concept that yields further reduction in thermal conductivity and potentially a substantial improvement in the thermoelectric figure-of-merit.

Dedication

To my family: Lee, Sally, Lindy, Julie, Michael & Steve
...happiness is sharing life with those you love

and

To those who dream of exploring space
...and who work to make this next frontier a reality for all

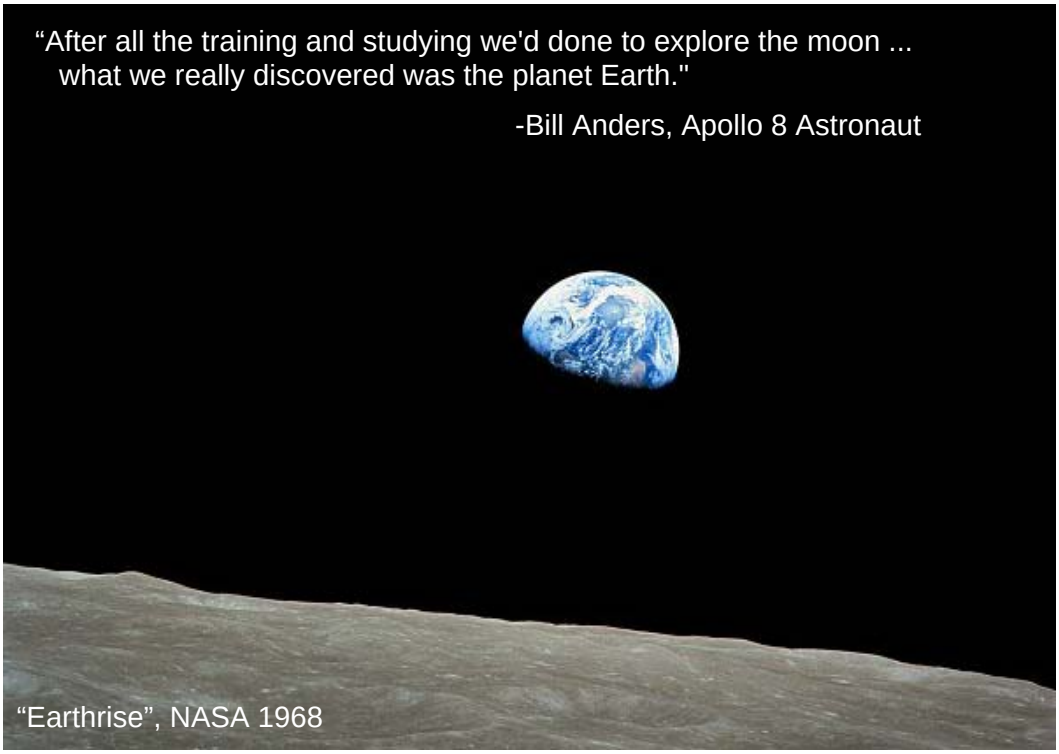

Acknowledgements

I am humbled by the support and guidance I have received from my colleagues and friends during my academic career, all of whom were instrumental in making this dissertation a reality. Foremost, I would like to thank my adviser Dr. Mahmoud Hussein for his scholarly mentorship, creative insights and encouragement over the past five years. I am grateful to have worked with a person who is enthusiastic, excited and open to discuss results on a daily interval. In addition, I would like to thank Dr. Ihab El-Kady for inviting me to work with him at The Sandia National Laboratory for six months in 2010. I enjoyed the many candid conversations we had concerning our research developments and advice regarding my career choices. I would like to thank my committee members – Kurt Maute, Carlos Felippa, Matt Glaser and Juliet Gopinath – for the discussion and feedback in their respective fields. I also would like to extend my gratitude to the entire Hussein research group – Osama, Mike, Sven, Dimitri and Romik –for your analytical conversations and for keeping daily life in the lab grounded and interesting. Special thanks to Osama Bilal for your high performance computational assistance and compilation of finite element codes; as well as Andrew Tomchek, Edgar Flores and Liao Liu for your partnership regarding our work with periodicity truncation. Finally, I give my thanks to the National Science Foundation which financially supported this work under a 2009 CMMI Grant #0927322 under the direction of Dr. Eduardo A. Misawa and the Sandia National Laboratory under grant No. 1113289.

During my seven years at the University of Colorado, I have been involved with several groups/organizations and have cherished the friendships and experiences that they have brought. Specifically, thanks to all those I have collaborated with at *The Laboratory of Atmospheric and Space Physics*, the *DANDE team at The Colorado Space Grant Consortium* and *The CU chapter of the Students for the Exploration and Development of Space*. I would also like to thank Dr. David Klaus and Dr. Scott Palo who provided advisement during my early years as a graduate student and Tim Wheeler an influential adviser while I was and undergraduate student who helped sparked my interest in building spacecraft.

In closing, I would like to thank my extended family in Colorado who made me feel so welcome following my move to the region for graduate study. Thank you to Aaron, Matt, Brian, Caroline, Justin and Garett for your long-term friendship. Finally, I would like to give a special shout-out to Ben and Amanda for routinely reminding me of the joys in exploring the great outdoors and for sharing your adventures with me.

Table of Contents

List of Figures

List of Tables

1 INTRODUCTION

The pursuit of efficient energy generation and consumption is perhaps one of the most significant challenges facing our global community today. In this modern era, energy consumption in the form of electricity is central to our economic activity and is fundamentally tied to improving the societal quality of life. There are, however, growing concerns that the increasing demand for energy coupled with dwindling resources and adverse environmental impacts are limiting economic growth. Hence, the ability to increase efficiency of power generation and consumption is of paramount importance.

One prominent direction for improving electric power generation is through thermoelectric energy conversion, or the process of converting energy in the form of heat into electricity and vice-versa. This solid-state process is attractive as most of the world's electricity is generated from heat energy. Furthermore, the established paradigm for efficient conversion from heat into electricity involves mechanical motion of some sort (i.e., spinning turbines) and is therefore inherently limited in its potential for drastic improvements in efficiency. Many concepts exist that utilize thermoelectric materials to harvest excess heat within power plants or to more ideally replace the need for mechanical motion all together. While intense research has been underway to advance and integrate thermoelectric devices for common uses, their relatively poor efficiency remains a major hurdle. Today these devices only exist within a few niche markets where efficiency is not a primary concern, such as portable heat and refrigeration devices or for radioisotope thermoelectric generators (RTGs) often used in spacecraft where solar power generation is not advantageous.

With the advent of the nanotechnology revolution, a new focus surrounding thermoelectric devices utilizing nanostructured materials has emerged with great promise. This dissertation seeks to explore new avenues in this area of research.

1.1 Introduction to Thermoelectric Materials

The thermoelectric effect, or the solid-state conversion of heat and electricity, occurs due to the difference in electric charge carrier transport of two conjoined materials. The intrinsic measure of how well these carriers diffuse with temperature is known as the Seebeck coefficient and is one of the primary indicators of thermoelectric performance. When joining two dissimilar metals together, an applied thermal gradient on the device will induce a voltage that is proportional to the difference of the Seebeck coefficients for the two metals and the applied temperature across the device. Semiconductor materials are found to have some of the highest known Seebeck coefficients and are primarily used in commercial devices. In Figure 1.1, a schematic of a common thermoelectric device is portrayed utilizing two doped semiconductor materials of both n-type and p-type. Here we see the *Seebeck Effect* (left) in which an

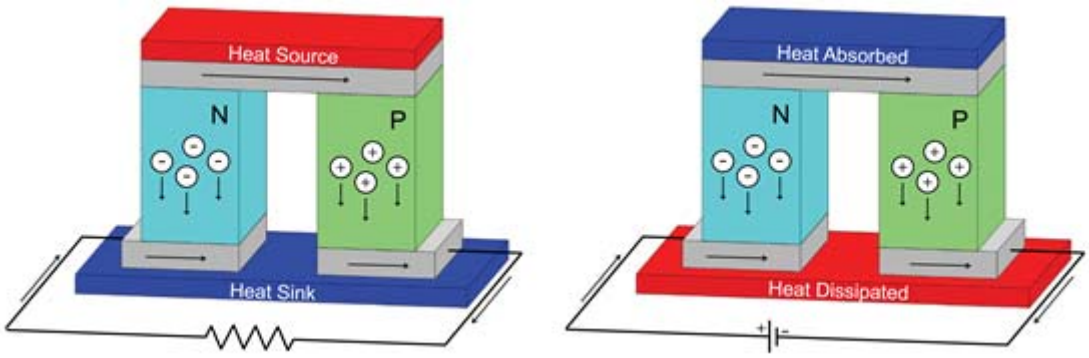

Figure 1.1: A schematic of a common thermoelectric device consisting of two different semiconductors. The conversion of heat into energy, otherwise known as the *Seebeck Effect*, is shown on the right while the reversible process known as the *Peltier Effect* is shown on the left.

applied temperature gradient induces a current and the reversible process known as the *Peltier Effect* (right) in which an applied power source induces a temperature gradient. On the left side of this schematic, a heat source is applied at the top (red) and the heat sink or cold surface is applied at the bottom (blue). The resulting thermal gradient across the materials causes a net flow of electrons in the n-type semiconductor and holes (i.e., electron absence as a charge carrier) in the p-type to diffuse towards

the cold surface. This creates a net voltage potential and hence an applied current load on the resister shown in the schematic. This process can also be reversed by eliminating the temperature gradient and replacing the resister with a power source as shown in the left side of Figure 1.1. The implied power creates a heat pump in which energy is absorbed at the top (blue) and dissipated at bottom (red).

The performance of a thermoelectric material is commonly measured by the *figure-of-merit*, *Z,* multiplied by the average temperature, *T*, across the device. The relationship of *ZT* with respect to the Seebeck coefficient, *S*, electrical conductivity, σ, and thermal conductivity *k* is:

$$ZT = \frac{S^2\sigma}{k}T \tag{1.1}$$

As discussed above, an improved Seebeck coefficient leads to increased performance. In addition, an improved electrical conductivity leads to more electron mobility and less resistance for the flow path of electrons thus improving the figure-of-merit. Finally, a reduced thermal conductivity in the materials across the thermal path allows for a greater thermal gradient and hence a higher *ZT*. Current *ZT* measurements of thermoelectric devices utilizing bulk materials hover just above 1 or roughly 10% efficiency [Pichanusakorn and Bandaru, 2010]. It has been hypothesized that a figure-of-merit greater than 3 is needed in order to make the technology of solid state thermoelectric devices a competitive alternative approach to energy conversion within industry, as stated by Vineis et al. [2010].

1.1.1 Challenges with Thermoelectric Materials

The 1950s was a period of remarkable advances in thermoelectrics. Most notable was the incorporation of semiconductor materials and the development of the Bi_2Te_3 alloy, which led to the first integrated commercial uses of thermoelectric devices for niche markets [Goldsmid and Douglas, 1954]. However, despite these improvements–which mainly focused on incorporating bulk materials into

thermoelectrics–the figure-of-merit effectively stagnated around $ZT = 1$, a value too low to be competitive with existing power generating and fluid-based refrigeration technologies in industry.

The difficulty in increasing efficiency utilizing bulk materials stems from the intrinsic inter-connection between the three variables determining the figure-of-merit. Utilizing techniques to improve one variable such as electron doping or the incorporation of impurities inherently manipulates the remaining variables in a manner that nullifies the benefits. The following are two prominent conflicts:

1) Thermal and electrical conductivity: both electrons and phonons (i.e., lattice vibrations) contribute to the thermal conductivity of a material. Since the intention is to increase the electrical conductivity while decreasing the thermal conductivity one must turn to manipulating phonons to increase the figure-of-merit. A common practice to inhibit phonons in bulk materials is to increase nonlinear wave scattering by incorporating random defects or impurities into the material. This however also leads to an increase in electron scattering thus tends to cancel out the benefits of lowering the thermal conductivity.
2) Seebeck and electrical conductivity: The electrical conductivity increases as the intensity of electron scattering decreases. However, this is contrary to the Seebeck coefficient which depends on disorder to enable electron diffusion. On a related note, one avenue for significantly improving the electrical conductivity in a semiconductor is through electron doping. However, addition of more electrons saturates the material and hence inhibits its Seebeck properties, thus cancelling out the benefits of raising the electrical conductivity.

Over the following three decades, these noted challenges arguably led to a period of relative inactivity and subdued interest in the field. It was not until the early 1990s when the focus reemerged after a series of studies–with one of the most notable by Hicks and Dresselhaus [1993] –which suggested

that vast improvements in the figure-of-merit could be achieved by using nanoscale techniques to independently control electron and phonon transport. The idea initially focused on incorporating nanostructured devices to confine the electron flow through a material thus increasing the Seebeck coefficient and electrical conductivity. This concept was later applied to thermal transport with more success by G. Chen [1998] and others with a baseline idea of using low dimensional and/or layered materials to specifically scatter phonons with as little interference as possible to the electron transport. During this development it was found that improvements to electron transport and the Seebeck coefficient were limited and, as a result, greater focus transitioned to reducing the thermal conductivity to improve *ZT* [Dresselhaus et al., 2007]. The idea of nanostructuring has led to a resurgence in thermoelectrics. Today, research in the field is being pursued globally with a wide variety of approaches in analytical modeling, fabrication and experimental testing.

1.1.2 Recent Advancements in Thermoelectrics

At present, there are two main approaches focused on the idea of inhibiting phonon transport in thermoelectrics. The first continues with the traditional track of utilizing bulk materials with complex crystalline microstructures. This work mainly focuses on a class of materials which contain a highly regular lattice structure with loosely bounded atoms or 'rattlers'. Several materials with these atomic scatterers have been documented to benignly scatter phonons with minimal impact on the electron transport. Skutterudites and clathrates are a class of materials that contain a strong cage-like core and can trap atoms or molecules inside to act as scatterers. Recent studies by Nolas et al. [1999] and Kleinke [2010] look at the feasibility of utilization of these materials for thermoelectric energy conversion and the realization of an improved figure-of-merit. Li et al. [2010] reviews a series of bulk thermoelectric materials and notes how the peak performance is approaching a $ZT = 1.5$ for a diverse group of materials at select temperatures.

The second focus area aims to use a superlattice (i.e., layered medium) configuration and/or low dimensional materials such as thin-films, nanowires and quantum dots to confine the electron transport and control the dispersion Balandin and Wang [1998] and scattering of thermal conductivity. There are a few studies of particular note: Venkatasubramanian et al. [2001] reported a $ZT = 2.4$ when utilizing thin-film superlattices with ultra-thin periodic layering (~1nm) of Bi_2Te_3/Sb_2Te_3 at room temperature. Harman et al. [2005] measured an even larger improvement, a $ZT = 3$, utilizing quantum dot superlattices of PbSeTe/PbTe at high temperatures. In the field of low dimensional materials, recent measurements of ZT for silicon nanowires have received much attention. Boukai et al. [2008] measured a $ZT = 1$ (a 100-fold improvement over bulk) while Hochbaum et al. [2008] had similar findings ($ZT = 1$) for nanowires with rough surfaces.

Despite the dramatic measurements of improved figure-of-merit for these nanostructured devices, there remain a few key difficulties/areas for improvements. It should be noted that a thermoelectric device requires both an n-type and p-type semiconductor material to function; as a result the reported ZT of a particular material does not represent the performance of the entire thermoelectric device. In addition, the complex fabrication techniques and experimental setup to measure ZT make it difficult for independent confirmation from other research groups. Snyder and Toberer [2008] have compiled a review which details further difficulties of ZT measurement accuracy. Another issue is concerned with the manufacturing complexity and delicate nature of these nanostructured devices, which makes it difficult to incorporate the technologies into wide-scale commercial use. As a result, there is an effort to embed superlattice and low-dimensional materials into a bulk setting. As pointed out by Dresselhaus et al. [2007], the two main approaches (utilization of bulk and nanostructured materials) which have grown apart over in the past are on the verge of coming back together as the future of thermoelectric devices may be centered on integrated devices.

1.2 Introduction to Phononic Materials

In this work, we are particularly interested in a new class of artificial materials that may be referred to as "phononic materials". Phononic materials may be divided into two categories: phononic crystals and acoustic metamaterials. In the following sections, an introduction is given on each of these two types of very promising materials.

1.2.1 Phononic Crystals

Phononic crystals (PC; a subclass of phononic materials) are synthetic elastic materials that by nature of their spatial periodicity exhibit unique properties concerning wave propagation. A primitive *unit cell* is the most basic construction of a PC; it is repeated in an orderly fashion essentially following the standard rules of crystallography. With careful selection of the intrinsic geometric and constituent material properties, wave scattering occurs at the periodic boundaries enabling wave interferences. The resulting dispersion relation effectively summarizes these wave interference mechanisms which, depending on the frequency, could be constructive (causing propagation) or destructive (causing attenuation). Of particular interest in a dispersion relation (also referred to as a frequency band structure) is the possibility of existence of a *band gap* or a frequency range in which waves cannot propagate. With proper tuning of the primitive *unit cell*, a PC can exhibit large band gaps enabling the design of materials with inherent dynamical filtering and waveguiding (among other) properties.

At the macro scale (μm-m) the dynamical characteristics of PCs lead to applications such as vibration isolators, radio frequency sensors, and imaging devices. In this size regime, PCs are commonly modeled as a continuum where a numerical discretization technique such as the finite element method is employed, or as a lumped parameter model with masses and springs to roughly represent a continuous configuration.

1.2.2 *Acoustic Metamaterials*

Acoustic metamaterials represent another type of PnMs; they are also periodic materials except they differ from PCs in that they exhibit local resonance properties. These properties may be realized by numerous configurations. The first realization was presented by Liu et al. [2000] in which a three-dimensional array of lead spheres was coated with a very thin (2.5-mm) layer of silicone rubber (i.e., a very soft material) and stacked in a simple cubic arrangement within an epoxy matrix. The heavy spheres were then able to resonate in their slots and as such introduce a new type of elastic band gap in the frequency band structure. This type of band gap emerges due to the interaction between a local resonance mode and the dispersion modes of the underlying periodic medium. This interaction is often referred to as hybridization. The most attractive feature of a locally resonant band gap is that it can appear at subwavelength frequencies since its creation is independent of Bragg scattering. Another practical realization of a locally resonant acoustic metamaterial is one that is based on a formation of a periodic array of resonating pillars on a flexural plate [Pennec et al., 2008, Wu et al., 2008]. This configuration will be utilized later in Chapter 5, albeit at the nanoscale.

1.3 Nanoscale Phononic Materials

The concept of a phononic material as described in Section 1.2 may very well be realized at the nano, or sub-continuum, scale (nm-μm). In the thermal transport regime, the wavelengths of the propagating waves are now on the order of the atomic spacing of a crystalline material. Therefore it is most accurate to model the unit cell at the atomic level, i.e., incorporating information about the number and location of individual atoms. Consequently, the dispersion relation now provides insight into the atomic motions associated with the crystal lattice as well as the added periodicity in the nanoscale phononic material. Such atomic scale resolution is essential when predicting phonon thermal transport properties. At this scale, lattice dynamics (LD) is employed to model the inter-atomic dynamics of the primitive unit cell and obtain the dispersion relation (further details are provided in Section 1.4.1).

When forming a nanoscale phononic crystal (NPC), a *supercell* is introduced to represent the basic periodic geometry of the nanostructured medium. Given that the selected material must obey the proper atomic arrangement, a supercell must be formed by following the order of the material lattice (i.e., consistent with the geometry of a primitive cell, or more conveniently, a conventional cell as will be shown later). As a result one can say that in principle a NPC is a crystalline material that has two levels of periodicity: (1) the natural underlying material lattice (defined by a primitive cell forming the baseline crystalline structure) and (2) the NPC lattice (defined by a supercell describing a unit cell of the nanoscale phononic material yet still containing the underlying material lattice information). This enables the ability to create large supercells with complicated features such as voids, boundaries and extensions utilizing the baseline material.

1.3.1 Methodology for Reducing Thermal Conductivity with Nanoscale Phononic Materials

Following on the above discussion, nanoscale phononic materials clearly present a promising candidate for the design of materials for desired thermal transport properties, and subsequently desired thermoelectric energy conversion properties. The main attractive aspect of nanoscale phononic materials in this context is their ability to be tailored, via unit cell design, to achieve desired dynamical/thermal properties. Motivated by this attractive trait, this dissertation aims to explore new nanoscale phononic material configurations for controlling the thermal conductivity, especially in semiconducting materials.

In this section, different configurations of nanoscale phononic materials are discussed. The different unit cell geometries studied in this dissertation are introduced along with the unique benefits and challenges which occur. In Section 1.3.2, an overview is presented that explains the reasoning behind the selection of silicon as a baseline material for these studies. Finally, in Section 1.3.3, a brief overview of similar recent research in the literature is presented.

In this work, two general material systems are considered: 3D bulk and 2D thin-films. For the 3D case, phonon wave propagation is admitted in all directions, while for the 2D case wave propagation is confined along only in-plane directions. There are two different ways to manipulate phonon dispersion within these material systems: 1) through NPCs where the introduction of periodicity enables Bragg scattering at the internal boundaries at the supercell level and 2) via nanophononic metamaterials (NPMs) where the presence of a feature such as pillars introduce local resonances. While the first route has been studied before in the literature (see Section 1.3.3), the concept of a NPM is being proposed for the first time in this dissertation.

In Figure 1.2, the combinations of the various material systems studied in this work are illustrated. Here the lattice geometry is rendered as a continuous solid for ease of viewing. The top row displays 3D bulk material systems, and the bottom row displays thin-film based material systems. For each, the nominal default case is a regular, uniform crystal. This is displayed in the left column and is used as a baseline representation of each class. Along the center column are the NPCs which are formed by introducing periodicity in the forms of voids. The last column on the right showcases the NPMs. When investigating 2D thin-films, the finite boundary (i.e., exposed surface) provides the opportunity to mount additional features and in this case resonating pillars are added to turn the thin-film into a metamaterial. NPCs and NPMs both fall under the classification of a nanoscale phononic material.

The differences in dimensionality and/or the presence of internal/external features have a dramatic effect on the dispersion spectrum. This is significant because as we explain later (in Section 1.4.2), the thermal conductivity is highly dependent on the dispersion. The phonon dispersion band diagram for each of the five material configurations is displayed in Figure 1.3. Shown in each of the subfigures is a plot of the temporal frequency versus the spatial frequency, or wavenumber (wave vector), of the vibrational modes propagating in the medium along a prescribed direction, in this case along one of the

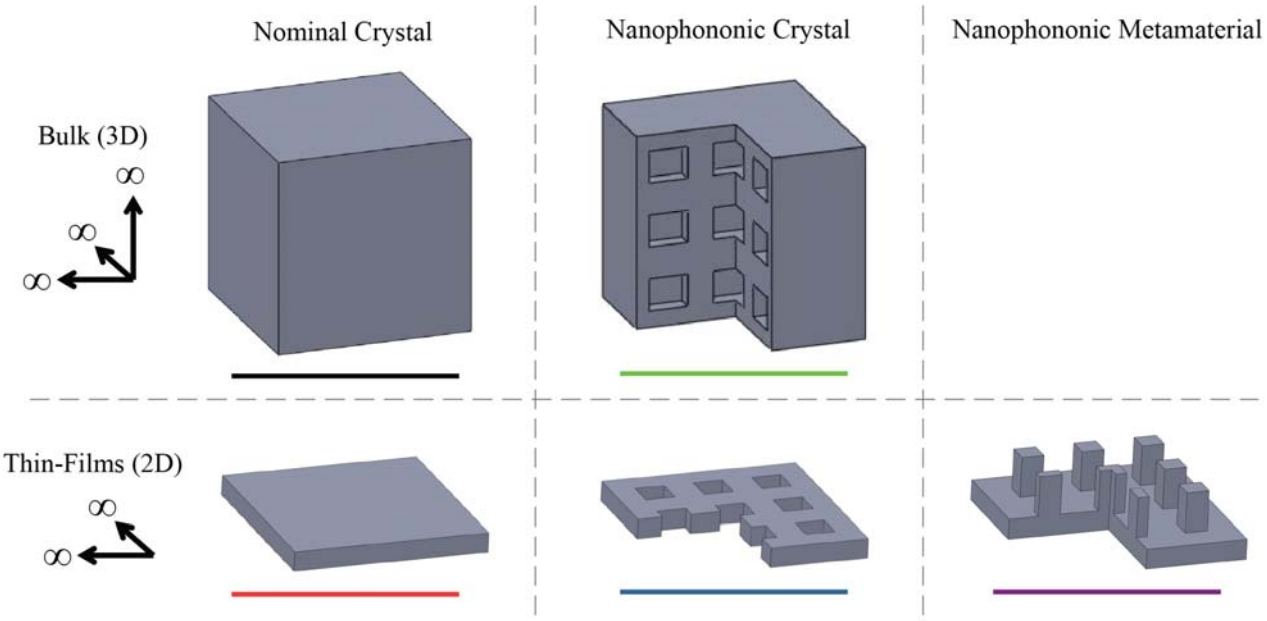

Figure 1.2: Configurations of silicon crystals considered in this work, shown as continuous solids for simple viewing. The top row displays a 3D bulk nominal crystal (left) and a 3D bulk NPC (center). The bottom row shows a 2D nominal thin-film (left), a 2D NPC thin-film (center) and a 2D NPM thin-film (right).

two in-plane orthogonal directions (referred to as the ΓX path in crystallography). The dispersion for the simplest case, a 3D bulk nominal material, is shown in black. It can be noted that many of the branches are degenerate due to the symmetry in this nominal material and that there are two distinct acoustic branches that start from zero at the Γ point. Upon introducing periodicity in the 3D bulk material to form a NPC, the dispersion branches (shown in green) are generally reduced in frequency, flatter, no longer degenerate and the acoustic branches are now split at the X point. Upon moving from 3D to 2D, for the nominal crystal there is a significant change in the dispersion (shown in red). Here there is a reduction in frequency, a few of the branches are no longer degenerate and finally there are three distinct acoustic branches, with the lowest one being near flat at the Γ point which is a trait of flexural plate-like motion. As periodicity is incorporated for the thin-film the changes in dispersion (shown in blue) mirror the bulk NPC, such as a general reduction in frequency, broken degeneracy, and flatter branches. However, the dispersion maintains a few key thin-film properties such as the three unique acoustic branches. Finally

when pillars are added onto the thin-film to form a NPM, the dispersion curves (shown in purple) looks similar to the default dispersion (red) with the primary, and significant, difference of exhibiting several very low flat frequency branches that cut through the underlying dispersion curves to form pseudo band gaps. These flat branches are associated with the pillars' resonating modes. Reduced degeneracy is also observed as in the NPC cases.

The key takeaway message from Figure 1.3 is that by modifying the dimensionality and/or periodic features, significant changes occur in the phonon dispersion. Given that the thermal properties in a material are dictated by the phonon dispersion, opportunities exist to engineer the unit cell configuration to improve thermoelectric efficiency. A unique aspect of the work presented in this dissertation is that the full dispersion of the nanostructure is used to compute the thermal conductivity of the material (see Section 1.4). Many studies in the literature often rely on approximate dynamical analysis by relying on bulk dispersion properties, which limits the accuracy of the predictions.

In this dissertation, the first material models studied are 3D bulk supercells which utilize voids to create the NPC. By focusing on a 3D nominal bulk system, a comparison could first be made between the thermal conductivity predictions of primitive silicon (the most basic atomic structure containing 6 degrees of freedom) and silicon supercells of a desired size and shape containing n degrees of freedom (black plot in Figure 1.3). Upon this understanding, a direct comparison of the thermal conductivity of supercells for nominal bulk and bulk NPCs (green plot in Figure 1.3) could be realized. Limitations however appeared in the treatment of phonon scattering, especially when boundaries were introduced from the void walls. In addition, uncertainties in the manufacturing process and how the electron transport would be interrupted by the voids needed to be addressed. The natural next move was to focus on nominal or homogenous 2D thin-films (red plot in Figure 1.3) which had readily available empirical data across various thicknesses. Because of this, the scattering parameters were fitted to accommodate the

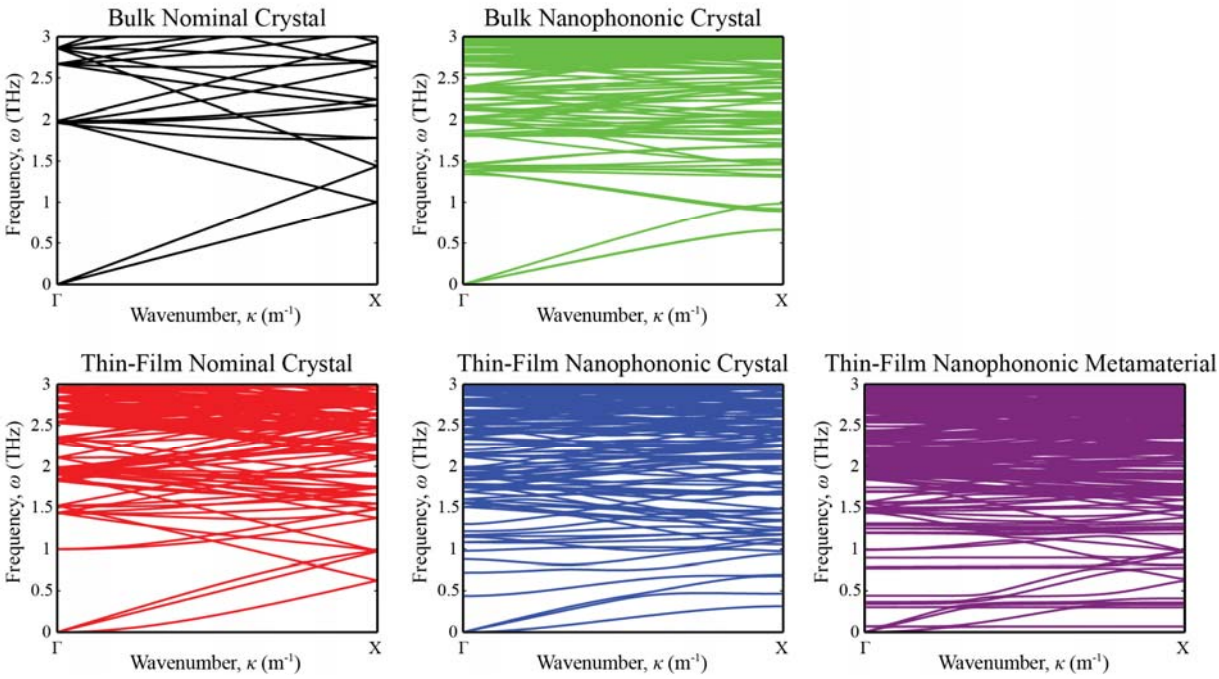

Figure 1.3: Dispersion for 3D bulk crystal (black), 3D NPC crystal (green), 2D thin-film (red) 2D thin-film NPC (blue) and a 2D thin-film metamaterial (purple). These plots offer a comparison between phonon dispersion for the various nanostructured configurations. For example note the difference in the acoustic branches between the 3D and 2D dispersion. In addition to phonon branch flattening, the modal degeneracy is broken by the insertion of voids which turns a default bulk material and thin-film into a NPC. The presence of pillars creates several flat branches cutting through the acoustic branches.

boundaries of the film. Upon understanding the thermal properties of thin-films, the next step was to insert voids to create the NPC (blue plot in Figure 1.3); however it was determined that the elimination of material along the electron path and the effects of phonon scattering due to the void created additional pitfalls in the physical behavior or uncertainties in the modeling. These concerns were eliminated by focusing on the proposed 2D NPM which was created by erecting an array of periodic pillars to the top free surface of a thin-film (purple plot in Figure 1.3) and thus not obstructing the electron path, nor causing any modeling concern on the effects of internal boundary scattering.

1.3.2 Selection of Silicon

For the entirety of this work, silicon is used as a baseline material for a variety of reasons: 1) Silicon is ubiquitous within the electronic industry and continues to hold a central part in the semiconductor

revolution. As a result, this material is well understood and embraced across the electronics industry with abundant capability and knowhow to manufacture complex, cost effective nanostructured devices; of which much empirical data already exists. 2) With the exception of thermal conductivity, silicon maintains properties which are excellent for thermoelectrics. Telkes [1947] famously stated that although silicon was electrically an ideal material, the high thermal conductivity properties inhibited it from advancing the field of thermoelectrics. Thus if it is possible to reduce its thermal conductivity without affecting its electrical conductivity, the potential for realizing high value of ZT are significant. And finally, 3) the simplicity of the silicon lattice geometry is advantageous for use as a baseline for future development of more complex crystalline structures. Since the theoretical thermoelectric figure-of-merit *ZT* of bulk silicon is relatively low compared to other materials such as the Bi_2Te_3 class (which are commonly used), it is believed that the improvements achieved in the context of silicon can be transferred to other material classes with magnified outcomes. Vining [2008] provides further assessment on the capabilities for developing silicon-based thermoelectric materials.

1.3.3 Brief Literature Review of Nanoscale Phononic Crystals

Several efforts have been underway to precisely quantify the reduction in thermal conductivity of NPCs in different configurations, e.g., bulk, nanowires, etc. Many of these efforts utilize lattice dynamics to predict the dispersion. Tamura et al. [1999] used LD to obtain the dispersion of 2D layered media. Gillet et al. [2009] and Gillet [2010] used LD in several studies of 3D bulk NPCs consisting of silicon with germanium inclusions. His models were based on supercells in which a large array of "inclusion" atoms is incorporated. These studies however did not establish conditions for the validity of the supercell LD calculations and did not present an analysis on the different underlying transport mechanisms and how they are affected by the periodicity of the NPC.

On the experimental front for patterned thin-films (i.e., thin-film NPCs), recent work by Yu et al. [2010], Tang et al. [2010] and Hopkins et al. [2011] show a significant reduction in thermal conductivity due to the influence of voids. Yu [2010] notes that the "structure exhibits a substantially lower thermal conductivity than an equivalently prepared array of silicon nanowires, even though this array has a significantly higher surface-to-volume ratio." In addition, Hopkins et al. [2011] notes that the thermal reduction is beyond what was expected from boundary scattering at the interfaces which suggests coherent phonon transport effects might be responsible.

1.4 Tools for Modeling Thermal Conductivity of Nanophononic Materials

We recall that our goal is to explore the utility of using 2D and 3D nanoscale phononic materials to inhibit propagating phonon waves that contribute significantly to thermal conductivity. To this end, one must first understand the wave motion behavior in nanoscale phononic materials (phononic crystals and metamaterials) and apply this understanding towards the manipulation of the dispersion relation. In addition, a robust methodology of calculating dispersion and thermal conductivity for an atomic-scale supercell must be developed and understood. In this section, an overview outlining the basic principles of phononic materials, lattice dynamics and the thermal conductivity formulation are overviewed to provide a basis for the work performed in the rest of the dissertation.

1.4.1 Lattice Dynamics

To model wave propagation in a discrete atomic medium, lattice dynamics calculations are conducted. In LD, each atom is treated as an individual point mass that is connected to neighboring atoms with a spatially dependent energy potential. The equations of motion for each atom within the system are compiled and a planewave solution is inserted to form the *dynamical matrix*. Upon treatment as an eigenvalue problem, the phonon frequencies are determined for each mode across all possible

wavenumbers (or wave vectors). In the harmonic approximation, each mode is characterized by a frequency, a wave vector, a polarization, and mode shape.

The conventional LD formulation utilizes Newtonian mechanics to compile the dynamical matrix which represents the inter-atomic interactions within the lattice. As a result, a force relationship is evaluated and balanced at each atomic location requiring a series of nine force constants to represent all orthogonal interactions. In this work (outlined in Chapter 2) an alternative energy-based Lagrangian formulation is proposed, following the identification of a network of springs connecting each atom with the other nearest neighbors, and this, in practice, pins each inter-atomic relationship to a designated axis and thus enables the use of a single force constant to represent the strength of each atomic pair interaction. However, we also use the standard Newtonian approach because of its use in available commercial software.

The NPCs and NPMs considered in this work consist of supercells with voids or a pillar, respectively. As a result, the periodicity is geometrically induced by the removal or addition of clusters of atoms. Although in many cases a band gap may not form by simply removing or adding material, the shifting in the phonon frequencies and the flattening of the dispersion bands have significant effects on the phonon wave propagation characteristics, leading to changes in the thermal transport properties (when compared to the original baseline crystalline material). Further details on lattice dynamics are available in the works of Dove [1993] and Maradudin [1963], and in Chapter 2 in the context of the newly developed Lagrangian-based lattice dynamics.

1.4.2 Thermal Conductivity Prediction

The thermal conductivity k of a material is related to the speed of energy carriers (phonons and electrons) and is inversely related to the resistance that these carriers experience when traveling in a medium. This property can be defined using Fourier's law,

$$q_x = -k\frac{dT}{dx}, \tag{1.2}$$

where the heat flux q_x, along a direction x, is proportional to a the negative of an applied temperature gradient dT/dx. Here the negative sign indicates that the energy flows from a source to a sink.

The Boltzmann Transport Equation (BTE) considers the statistical distribution of energy carriers when subjected to an external force, in this case a temperature gradient. When combined with Fourier's law, the following expression,

$$k_i = \sum_{\lambda}\sum_{\boldsymbol{\kappa}} c_{ph}(\boldsymbol{\kappa},\lambda) v_{g,i}^2(\boldsymbol{\kappa},\lambda)\tau(\boldsymbol{\kappa},\lambda), \tag{1.3}$$

can be extracted to predict thermal conductivity k. Equation (1.3) states that the thermal conductivity is calculated by summing contributions across all phonon branches of dispersion (for branch number or mode λ) at every point spanning the Brillouin Zone (for each wave vector $\boldsymbol{\kappa}$). Here c_{ph} is the specific heat or energy of the mode per unit volume, v_g is the group velocity (along component i) representing the speed of the phonon wave and τ is the scattering rate or the lifetime of the phonon in the lattice. The specific heat and group velocity can be obtained directly from the phonon dispersion while the scattering time is usually fitted to empirical data. Alternatively the scattering parameters can be obtained by either anharmonic LD calculations or molecular dynamics simulations.

The form of Equation (1.3) requires knowledge of the phonon dispersion for every point within the Brillouin Zone which can be computationally costly. The Callaway-Holland formulation [Callaway, 1959, Holland, 1963] for thermal conductivity introduces a simplification by assuming that the material is isotropic and hence the Brillouin Zone is uniform with respect to all directions, thus enabling a simplified evaluation of thermal conductivity. With this approximation, Equation (1.3) becomes

$$k = \frac{4\pi/3}{(2\pi)^3}\sum_{\lambda}\int_0^{2\pi/a} C_{ph}(\kappa,\lambda) v_g^2(\kappa,\lambda)\tau(\kappa,\lambda)\kappa^2 d\kappa \tag{1.4}$$

for a face-centered cubic lattice type such as bulk silicon where the Γ-X path ranges from 0 to $2\pi/a$. Here the summation over wave vector $\boldsymbol{\kappa}$ is replaced with $4\pi\int \kappa^2 d\kappa$ to represent the volume of the now-spherical Brillouin Zone which is roughly similar to the shape of primitive silicon. In addition, the specific heat C_{ph} is now non-dimensionalized with respect to volume and has the units of Joules/Kelvin. The average value of the velocity vector for an isotropic spherical volume produces the factor of 1/3 (and hence allows us to eliminate the dependence of v_g with i) and the normalized volume of the Brillouin Zone in 3D space for a primitive cell, $(2\pi)^3$.

Since this work focuses on dielectric materials at around room temperatures, the contribution to the thermal conductivity from the electrons and photons are negligible. Further details on the fundamentals of nanoscale thermal transport is available in Kittel [2005] and the work of Chen [2005].

1.5 Broad Literature Review

This section provides a thorough, yet non-exhaustive, survey of the current literature regarding the main focus areas of this research and includes discussions on: 1) wave propagation in periodic media, 2) lattice dynamics and finally 3) nanoscale thermal transport.

1.5.1 Wave Propagation in Periodic Media

This section presents a brief and non-exhaustive synopsis of some of the most significant contributions to elastic wave propagation and provides a flavor of the relevant developments to this work. Rich overviews pertaining to the historical development of wave propagation and periodic media research are provided by Brillouin [1953] and Graff [1991].

1.5.1.1 Early Studies

One of the first worked examples of wave propagation in a periodic medium occurred in 1686 by Newton in an attempt to model the speed of sound in air. He assumed that the waves could be modeled as

a one dimensional series of point masses and springs, Newton [1686]. This was only eight years after Hooke [1678] formulated the *law of proportionality* between stress and strain, the basis for the modern theory of elasticity. Developments in wave propagation in isotropic solids followed with significant contributions by Taylor, Euler, Bernoulli, Lagrange, Navier among others, which provided insight for vibrations in lumped parameter models, energy methods and simple elastic solids. Poisson [1827] was among the first to investigate wave propagation in elastic solids and distinguish the difference between longitudinal and transverse modes. Advances soon followed that incorporated complex solids (beams, thin plates, surfaces etc.) which set the basis for our modern day understanding of elastic wave propagation theory.

An early study of wave propagation in continuous periodic structures can be traced back to Rayleigh [1887] who used Floquet's theorem for one-dimensional elastic composites. The mathematical expressions to model a unit cell in a three-dimensional media were formulated by Bloch [1928] in the context of electrodynamics. This work led to a revolution in the understanding of the electronic structure of solids and the classification of materials into conductors, insulators and semiconductors. Brillouin [1953] used unit cell geometrical symmetry to define, in reciprocal space, a finite wavenumber range that would encompass a complete solution of the dispersion relation regardless of structural complexity. The accumulative body of work referred to above would later be widely applied and has led to the emergence of the field of phononics[*].

[*] Phononics2011: The First International Conference on Phononic Crystals, Metamaterials & Optomechanics was held in May of 2011 in Santa Fe, New Mexico. The diverse range of topics and discussions by over one-hundred participants has set the stage to continue this meeting in the future to enable further growth of the phononics community.

1.5.1.2 Periodic Materials from the 1950s Onwards

Now a brief synopsis is provided starting from the 1950s. A thorough overview is well beyond the scope of this dissertation. Instead a narrow snapshot summary of some of the most relevant topics that have impacted this work are provided.

Thomson [1950] gave a thorough analysis of elastic wave transmission in a stratified medium. Lee et al. [1973] investigated the properties of band gaps and their dynamical characteristics. Kushwaha et al. [1993] contributed to development of the Plane Wave Expansion Method for Phononic material band structure calculations. Mead [1996] compiled a thorough analysis of discrete and continuous periodic structures examining their behavior in numerous configurations. Recently Hussein et al. [2006, 2007] studied the correlation between Phononic materials in infinite and finite settings and proposed a multiscale dispersive design methodology that effectively combines the two.

Within this dissertation, many previous efforts have been crucial in setting the groundwork, for example, the work of Jensen [2003] who used LD of a 2D mass-spring lumped-parameter model to determine the effect of defects on the opening of band gaps. Another example is the Reduced Mode Bloch Expansion formulation developed by Hussein [2009] to enable accurate model reduction (and hence reduce the required computational resources when calculating band structures). Finally the effect of periodicity truncation (the topic of Section) has been explored by Haldky-Hennion et al. [2005].

1.5.2 Nanoscale Thermal Transport

1.5.2.1 Lattice Dynamics

Although the direct evolution of the lattice dynamics concept may be ambiguous, the idea of utilizing a lattice-based system with interatomic energy potentials to model dispersion of a prescribed medium has a lengthy history. It can be found that the advancements in lattice dynamics were driven by the goal to improve thermal conductivity predictions and as a result closely follow the developments in the following sections. However, there are distinct milestones and phases in the advancement of lattice

dynamics which are outlined in the next paragraph. Further overviews on this topic are available by Brillouin [1953], Maradudin [1963] and Horton [2003].

The first known problems utilizing the concept of lattice dynamics was performed by Newton [1686] which utilized masses and springs arranged in a linear chain to determine the speed of sound in air. Although much advancement involving periodicity and elastic media over the next two-hundred years was realized, one of the most notable developments in the concept of lattice dynamics came from Einstein [1907] and Debye [1912] who were among the first to use the mass/spring concept to approximate the thermal properties and dispersion in a material. During this same period the first dispersion relation and frequency spectra of atomic interactions embedded in a crystalline lattice were published by Born and von Karman [1912]. This concept utilized a simple mass/spring relationship with a basic energy potential and formed the baseline practice of lattice dynamics that remain to this day. Over time a series of improvements were implemented to the energy potential to span a larger selection of atomic elements and lattice types, accurately portray dispersion at extreme temperatures and to incorporate optical modes. One of the most notable potentials was introduced by Lennard-Jones [1924] which enabled simplistic approximation to the nonlinear attractive / repulsive interatomic forces of common bonds. More recently advanced multiple body potentials have been developed with the help of computational resources and empirical data yielding dispersion relations with a high level of accuracy; a few modern potentials for silicon were formulated by Stillinger and Weber [1985] and Tersoff [1988a 1988b].

Along a different track, in the 1950's a mathematical formulation was developed to automate the lattice dynamic formulation utilizing a generic lattice type and energy potentials utilizing multiple bodies. This formulation also included anharmonic perturbation theory which today has become a corner stone of lattice dynamics and used extensively when modeling nonlinear effects such as phonon scattering. An extensive overview of this mathematical formulation is available by Maradudin [1963].

1.5.2.2 Thermal Conductivity at the Nanoscale

In this section a brief discussion is provided on the evolution of thermal characterization of solids and how it has led to our current understanding of thermal transport at the nanoscale. There are several sources which elaborate in detail on several of the key concepts briefly summarized in this report: Kittel [2005], Ashcroft and Mermin [1976] and Chen [2005].

Einstein [1907] was among the first to model the heat capacity of solids with kinetic theory. He assumed that the heat capacity of a solid was due to the atomic lattice vibrations. For his analysis, he assumed that each atom in the lattice was independently connected with springs and masses (i.e., a quantized harmonic oscillator) all of which, for simplicity, had the same frequency. Debye [1912], expanded upon this model to account for the varying frequencies which has yielded improved results at low temperatures that better matched empirical measurements. This formed the foundation for Peierls [1929] to characterize the "*quantized normal modes of a perfect lattice, giving rise to the concept of phonons which is analogous to photons in radiation theory*[†]." Based on this concept, Klemens [1951] performed one of the first comprehensive theoretical studies of thermal conductivity by incorporating the Boltzmann Transport equation and true phonon lattice vibrations. In addition, this work was among the first theoretical models to incorporate phonon-phonon interactions. Klemens [1955] included the influence of material imperfections on phonon scattering.

Callaway [1959] implemented this model for silicon forming a simple formula that uses bulk phonon dispersion and experimental data. Here he assumed that the Brillouin Zone was directionally isotropic and only considered three degenerate non-dispersive acoustic modes for contribution to the thermal conductivity. Holland [1963] expanded upon this work by distinguishing between transverse and longitudinal modes and including optical modes. Today the Callaway-Holland model is widely used as a

[†] As stated by Klemens [1951]

simple formulation for the thermal conductivity prediction of face-centered cubic crystals. For silicon, improved experimental measurements of dispersion [Dolling 1963] and elaborate, semi-empirical, formulations of interatomic energy potentials [e.g., Stillinger and Weber, 1985, Tersoff, 1988(a), 1988(b)] have led to further improved models of phonon transport especially when influenced by crystalline boundaries [Li, 1988].

With robust, well characterized interatomic energy potentials, the LD formulation [see Dove, 1993 and Maradudin et al., 1963] is widely used to calculate the phonon dispersion of relatively simple bulk materials or complex nanostructured materials. The same principles that govern the Callaway-Holland model for primitive silicon can therefore be tailored to model the thermal transport of nanoscale phononic materials based on supercells and for complex nanostructured geometries such as thin-films, nanowires and nanodots.

1.5.2.3 Thermal Conductivity of Nanoscale Phononic Materials

The study of thermal transport in nanoscale phononic materials is a diverse field that requires both rigorous theoretical analysis and precise experimental measurements. In recent years, advances in computational modeling complemented with new fabrication techniques have led to intense research development in *phonon engineering* of nanoscale structures [see for example Chen, 2000(a), 2000(b) and Balandin, 2005]. In general, studies concerned with the thermal transport properties of nanoscale phononic materials need to adequately address the (1) treatment of dispersion and (2) the nonlinear scattering processes which involves the interactions of phonons with boundaries, impurities and other phonons. A brief overview of some of the early works in nanoscale phononic materials (or superlattices in the context of 1D material systems) and current avenues of interest are now presented.

One of the early works that identified the influence of artificial periodic media on thermal conductivity was by Balandin and Wang [1998]. He used simplified continuum models for the dispersion

of semiconductor quantum wells and used low order approximations of scattering rates. Follow-on work by Balandin et al. [2003] showed that in principle phonon transport can be inhibited with repeated inclusions. A similar conclusion was found by Cleland et al. [2001] considering a one-dimensional superlattice. It was suggested that a significant reduction in the thermal conduction is possible, at the very least due to the interface scattering. Other efforts have been underway to precisely quantify the reduction in thermal conductivity of superlattices in different configurations, e.g., bulk, nanowires, etc. Tamura et al. [1999] used LD to determine the dispersion of 2D layered superlattices. Gillet et al. [2009] and Gillet [2010] used LD in several studies of 3D bulk nanoscale phononic materials consisting of silicon with germanium inclusions. His models were based on supercells in which a large array of atoms is incorporated. These studies however did not establish conditions for the validity of the supercell LD calculations and did not present an analysis on the different underlying transport mechanisms and how they are affected by the periodicity of the nanoscale phononic material.

To improve upon the prediction of phonon lifetimes (due to phonon-phonon, phonon-boundary, and phonon-impurity interactions), molecular dynamics (MD) simulations have also been employed (for both bulk and nanostructured media). The Green-Kubo method [Green 1954, Kubo 1957] is widely used as a statistical approach for predicting the thermal conductivity using MD information. McGaughey and Kaviany [2006] provide a comprehensive overview of phonon transport analysis using MD. Mingo [2003] studied nanowires using both LD (for dispersion) and MD (for capturing anharmonic effects) to further improve and assess the emerging thermal conductivity predictions. This work confirmed earlier reports stating that phonon-boundary interactions cause a significant reduction in the thermal conductivity. Chantrenne et al. [2005] built upon this work for nanoribbons. He et al. [2011] performed a similar study for complex porous thin-films involving thousands of atoms. In most of these studies, however, whenever LD is employed, it is approximated with that of the bulk material. Some exceptions are the works of McGaughey et al. [2004, 2006] and Laundry et al. [2008] in which the full dispersion of

layered 1D diatomic materials were incorporated and MD was employed to obtain the scattering rates. By accounting for the full dispersion of the nanostructured crystal, not only is the model more accurate but it also provides insights into the role that coherent wave propagation mechanisms play in determining the thermal transport properties. This is the approach followed in this report.

On the experimental front, advances have been made in measuring the thermal conductivity of bulk materials, thin-films, nanowires etc. Asheghi et al. [1997, 1998] and Liu et al. [2004] were among the first to measure the lateral thermal conductivity of thin and ultra-thin-films. Their work correlated the decreasing film thickness to a drop in thermal conductivity due to the influence of boundary scattering. Li et al. [2003] performed one of the first studies of nanowires and noted the reduced thermal conductivity verses diameter due to phonon-boundary scattering.

1.6 Objectives and Overview of Dissertation

Nanoscale phononic materials can be utilized to alter the thermal transport properties of an otherwise regular crystalline material due to phonon manipulation. This dissertation aims to first improve upon the existing formulations for prediction of the thermal transport properties of nanoscale phononic materials. The prime goal is to elucidate the full effects of the added periodicity on the phonon transport properties and to introduce the concept of a NPM for the purpose of realization of high value of thermoelectric figure-of-merit. Meeting this goal will potentially impact others applications as well, for example, enhancement of heat dissipation in semiconductor materials.

There are five main **objectives** in this dissertation:

1. Develop a Lagrangian formulation for lattice dynamics calculations for 3D nanoscale phononic materials. Show how the inclusion of a defect or a heavy point mass creates significant changes in the dispersion and leads to the opening of a band gap.

2. Develop supercell lattice dynamics and thermal conductivity prediction models of silicon-based 3D NPCs. Characterize the thermal reduction due to coherent phonon transport mechanisms.
3. Develop full unit cell models for lattice dynamics calculations and thermal conductivity prediction of silicon thin-films. Compare with alternative models and experimental measurements.
4. Develop supercell models for lattice dynamics calculations and thermal conductivity prediction of silicon-based thin-film NPMs.
5. Determine the influence of periodicity truncations in PCs, and verify with experiments at the macroscale (note this completed work is available in a conference article and is omitted from this dissertation since it is outside the scope of nanoscale thermal transport).

1.6.1 Overview of Dissertation

An outline of the main chapters of the dissertation is presented in this section. It begins with a discussion of lattice dynamics in a Lagrangian framework. It next transitions into modeling silicon thermal conductivity of primitive, uniform supercells and NPC supercells in a 3D bulk setting. The final part of the dissertation transitions to 2D thin-film materials in which models of the thermal conductivity of uniform thin-films and NPM thin-films containing resonating pillars are presented. Chapters 2-5 are written in the form of journal articles of which Chapter 3 has already been published and the rest are in preparation for submission (some have been already been published as conference proceedings).

In chapter 2, the dispersion of NPCs is modeled using a Lagrangian formulation. The atomic structure and force constants are accounted for by means of a mass-spring model. This study focuses on a simple cubic lattice with one mass per primitive unit cell and the utilization of a rather simple interatomic potential. The model is used to conduct a series of studies on the influence of defects intentionally

introduced to the lattice at a supercell level. Under various defect conditions, a band gap emerges with varying location and size. In addition, a general reduction in phase and group velocities is demonstrated. A journal article is currently in preparation that highlights the difference between the energy-based Lagrangian formulation and the conventional Newtonian lattice dynamics formulation. A corresponding conference article has been published in the 2009 ASME Biennial Meeting on Vibration and Acoustics.

In chapter 3, supercell lattice dynamics is used to investigate the thermal transport behavior of three-dimensional NPCs formed from silicon and cubic voids of vacuum. The periodicity of the voids follows a simple cubic arrangement with a lattice constant that is around an order of magnitude larger than that of the bulk crystalline silicon primitive cell. The phonon band structure is computed and subsequently used to predict the thermal conductivity following the Callaway-Holland model. The findings shed light on the minimum supercell size and wave vector sampling resolution needed to accurately predict thermal conductivity of NPCs. Furthermore the results show that even for relatively small voids and unit-cell spacing, dispersion at the NPC unit cell level plays a noticeable role in determining the thermal conductivity. This work has been published in a special issue of the journal *AIP Advances* [Davis and Hussein, 2011]. A corresponding conference abstract was published in Phononics 2011: 1st International Conference on Phononic Crystals, Metamaterials and Optomechanics.

Chapter 4 is dedicated to modeling the thermal conductivity of silicon thin-film supercells using full-scale lattice dynamics. The phonon band structure of 2D thin-films is computed and found to exhibit significant differences when compared to that of the bulk material. A 2D form of the Callaway-Holland model is formulated to incorporate the out-of-plane finite properties of a thin-film. This model is compared with the conventional formulation which uses bulk dispersion and/or scattering parameters to approximate the phonon thermal conductivity. The results show that the thin-film full dispersion model better fits with the experimental data over a large temperature range. A journal article documenting this work is under preparation. A corresponding conference article has been published in the 2012 ASME

International Mechanical Engineering Congress and Exposition. This work was done in collaboration with Sandia National Laboratories.

In Chapter 5 the thin-film work is expanded upon to include pillars which are embedded on the free surface forming a NPM, which is a novel concept. Here the pillars act as local resonators to manipulate the propagation of phonon waves at subwavelength frequencies. One of the primary benefits to incorporating pillars is that they are not in the path of electron transport which is contrary to other NPC studies in which voids are inserted through the thickness of the thin-film. Lattice dynamics is used in conjunction with a finite element formulation to model dispersion of unit cells consisting of various sizes. For the finite element model, special considerations are taken to ensure that the adequate element sizes are considered in order to sufficiently capture nanoscale effects. The results show that the presence of a pillar significantly reduces the thermal conductivity in the thin-films. This effect is further pronounced by varying pillar height and unit cell spacing. A journal article documenting this work is under preparation. A corresponding conference abstract is due to appear in Phononics 2013: 2nd International Conference on Phononic Crystals/Metamaterials Phonon Transport and Optomechanics.

Finally, the dissertation closes with a few concluding remarks and discusses a future outlook and recommendations for follow-on studies.

1.7 Nomenclature

Acronyms

BTE	Boltzmann Transport Equation
LD	Lattice Dynamics
MD	Molecular Dynamics
NPC	Nanoscale phononic Crystal
NPM	Nanoscale phononic Metamaterial
	Note: Both NPCs and NPMs are a subset of Nanoscale phononic Materials
PC	Phononic Crystal
PM	Phononic Metamaterial

Variables

S	Seebeck Coefficient (V/K)
σ	Electrical Conductivity (1/Ωm)
k	Thermal Conductivity (W/mK)
T	Temperature (K)
Z	Dimensional Thermoelectric Figure-of-Merit (1/K)
ZT	Non-dimensional Thermoelectric Figure-of-Merit (unitless)
q	Heat Flux (W/m^2)
x	X-directional length (m)
$\boldsymbol{\kappa}$	Wave Vector (1/m)
κ	Wavenumber (unitless)
λ	Phonon Branch Polarization
c_{ph}	Volumetric Specific Heat (J/m^3K)
C_{ph}	Specific Heat (J/K)
v_g	Group Velocity (m/s)
τ	Phonon Scattering Time (s)
a	Lattice Constant (m)

Subscripts

x	denotes x-direction
i	denotes i component of direction

1.8 References

References for Chapter 1 are available in the Bibliography (Chapter 7)

2 LATTICE DYNAMICS IN A LAGRANGIAN FRAMEWORK

Journal Version:
Under Preparation;

Preliminary Version:
Davis, B.L. and Hussein, M.I., "A three-dimensional lumped parameter model of nanoscale phononic crystals," *Proceedings of 22nd ASME Biennial Conference on Mechanical Vibration and Noise*, [CD ROM: pp. 1-6], San Diego, California, 30 August - 2 September 2009.

2.0 Abstract

This work focuses on modeling nanoscale phononic crystals and analogous lumped-parameter systems by setting up the appropriate Lagrangian equations of motion. The lattice structure and interacting force constants are accounted for by means of a mass-spring model. In particular, we focus on a simple cubic lattice with one mass per primitive unit cell. We use the model to predict the wave dispersion frequency spectrum. We then use the model to conduct a series of studies on the influence of defects intentionally introduced to the lattice at a supercell level. One area of interest is the effect of such alterations on the size and location of band gaps. Alternative methods for determining wave propagation through lattice systems are discussed in detail and included Section 2.7.1.

2.1 Introduction

Within the field of phonon physics, lattice dynamics calculations are essential for characterizing the electronic and thermal properties of crystalline materials [1-4]. This well-established approach typically utilizes Newtonian mechanics to model the motion and interactions of atoms immersed within a lattice. The results yield important clues in studying a wide range of topics including the thermal conductivity of crystalline solids [7-9] and nanoscale phononic crystals (NPC) [10-12]. Lattice dynamics calculations may also be used to formulate the effective elastic properties of periodic materials [e.g. 15]. While lattice dynamics calculations are carried out primarily for atomic-scale models, in principle these calculations may also be lumped parameter spring-mass models representing macroscale periodic materials (such as

periodic composite materials) to study the effects of boundaries and viscous dampening [16,17]. With the growth of computational resources and material-level fabrication techniques, the role of lattice dynamics in the analysis of wave propagation in complex periodic material systems is growing rapidly.

From a historical perspective, the propagation of waves in a one-dimensional infinite mass chain was first modeled by Sir Isaac Newton as an attempt to calculate the speed of sound through air [18]. This analysis was based on what is now known as '*classical mechanics'* where rigid bodies are modeled as a system of particles with interacting forces. Approximately one hundred years after Newton's studies Joseph-Louis Lagrange first used an energy based method to model the dynamical motion of interacting bodies [19]. By utilizing general coordinates, he showed that the dynamical response of a set of particles can be calculated by conserving the net energy and momentum of a system [5]. With this, a new level of dynamic complexity could be captured as the physical coordinates are aligned with the mechanical motion of a system [6]. This eliminates the need to define the time-varying constraining force on each particle. The simplified equations of motion provide an intuitive perspective of the wave propagation in the medium. When applied to lattice dynamics, Lagrangian mechanics enables practical means for more advanced attributes such as damping or non-linearity. The formulations is also easily adapted from a unit cell framework to a truncated periodic structure since the derivations involve an explicit treatment of individual "springs" connecting the various masses with each other.

In this paper, a NPC is modeled as a periodic lumped-parameter mass-spring system. Here the point masses represent the atomic placement and the arrangement of springs imparts an inter-atomic potential for a determined number of nearest neighbor interactions. The formulated equations of motion are used to determine the dynamic response and solve for the phonon mode frequencies i.e., the dispersion relation. This paper presents the development of the lattice dynamics equations of such spring-mass model by following a Lagrangian mechanics framework, as opposed to the Newtonian framework as commonly done for atomic-scale frequency band structure calculations. The advantage is that we can

now associate a single force constant to each specific atomic pair for a prescribed geometric orientation. In contrast, for the Newtonian approach, nine force constants are calculated for each atom to account for the elastic forces experienced from all directions and from all nearest neighbor atoms – without specifically specifying and allotting springs.

Section 2.2 outlines the derivation and development of the lattice dynamics within a Lagrangian framework. Section 2.3 presents a fully worked example for a simple nanoscale cubic lattice structure. Here a primitive unit cell is repeated along specified Cartesian directions with Bloch wave propagation conditions imposed to compute the band structure dispersion relation. The differences between the two methods (Lagrangian versus Newtonian) are discussed in section 2.4 and the versatility of the model is demonstrated in Section 2.5. Finally we consider the possibility of opening up a band gap in our model by perturbing the mass of a single atom in a 5x5x5 supercell, and as such effectively form our NPC, or phononic bandgap material.

2.2 Lattice Dynamics in Newtonian and Lagrangian Frameworks

As discussed above, the dynamic motion of an atomic-scale system is commonly modeled following the formulations of Newtonian mechanics. In this approach, the equations of motion are determined by balancing forces on a prescribed mass within the lattice. Eq. (2.1) represents the application of Newton's second law of motion, i.e., the acceleration of mass i is constrained by the gradient of the instantaneous elastic energy potential φ imparted by neighboring masses which follow. Here $\bar{r}$, $\ddot{\bar{r}}$ and m are the position vector, acceleration vector and mass respectively with t denoting time. The gradient term requires the evaluation of the elastic energy potential φ in the prescribed lattice geometry. The full lattice dynamics formulation leading to an eigenvalue problem whose solutions provides the dispersion relation is summarized in the appendix.

$$\nabla \varphi_i(\bar{r}_i, t) - m_i \ddot{\bar{r}}_i(t) = 0 \tag{2.1}$$

As an alternative approach, Lagrangian mechanics may be used for the generation of the equations of motion and dispersion relation for a crystalline material. Lagrangian mechanics is based on the principle of virtual work, due to applied and inertial forces, and the notion of a virtual displacement defined in a manner consistent with the constraints. This is the basis for d'Alembert's principle which takes the form of

$$\delta W_i = \left(\overline{F}_i - m_i \ddot{\overline{r}}_i\right) \cdot \delta \overline{r}_i = 0 \tag{2.2}$$

where the virtual work δW performed on the system is set to zero to conserve energy. The variables $\overline{F}$, m, $\ddot{\overline{r}}$, and δr denote the force vector, mass, acceleration vector, and virtual displacement vector respectively for the mass i. A set of generalized coordinates q, which represent the motion of the system is established as

$$\overline{r}_i = \overline{r}_i\left(q_1, q_2, \ldots q_n, t\right) \tag{2.3}$$

where the motion of each mass i is fixed to n degrees of freedom. Upon combining Eqs. (2.2) and (2.3) and incorporating the generalized external (i.e., non-conservative) force Q_i the Lagrangian takes the form of

$$Q_i = \frac{d}{dt}\left(\frac{\partial T_i}{\partial \dot{q}_n}\right) - \frac{\partial T_i}{\partial q_n} + \frac{\partial V_i}{\partial q_n} = 0. \tag{2.4}$$

Since the interest is dispersion analysis, we set $Q_i = 0$. The kinetic energy T can be written as

$$T_i = \frac{1}{2} m_i \dot{\overline{r}}_i^2 \tag{2.5}$$

and potential energy V as

$$V_{ii'} = \frac{1}{2} k_{ii'} (\bar{r}_i - \bar{r}_{i'})^2 \tag{2.6}$$

where k represents the elastic stiffness between interacting masses i and i'. It should be noted that the potential energy is derived on the basis of Hookes law requiring the position of mass i and neighboring mass i'. The total potential energy is found from the summation of all neighboring mass interactions i' considered. In addition, the spring stiffness constant between the mass pairs is defined from the second spatial derivative of the energy potential

$$k_{ii'} = \frac{\partial^2 \phi}{\partial \bar{r}_{ii'}^2} \tag{2.7}$$

were ϕ is the linear stiffness within the generalized coordinate system with a separation distance of $\bar{r}_{ii'}$.

It is convenient to use three degrees of freedom for each mass following an orthogonal Cartesian coordinate system defined by the x, y, and z coordinates, i.e.,

$$\bar{r}_i(q_1, q_2, \ldots q_n, t) = \bar{R}_i(x, y, z, t) \tag{2.8}$$

In this coordinate system, the kinetic and potential energy for each direction are easily evaluated, with the exception of determining the elastic constant k. Here the stiffness magnitude is evaluated in a similar manner as in Eq. (2.7), except now this is done in the Cartesian coordinate system $\bar{R}_i$.

$$k_{ii'} = \left. \frac{\partial^2 \phi}{\partial \bar{r}_{ii'}^2} \right|_{\bar{r}_{ii'} = \left| \bar{R}_i - \bar{R}_{i'} \right|} \tag{2.9}$$

Since only one variable is used to represent the spring constant between each mass pair, $\bar{R}_{ii'}$ defines the spring extension with respect to the chosen coordinate system. This is done by taking the dot product of the coordinate unit vectors with the normalized unit vector between mass i and i'.

$$\overline{R}_{ii'} = (\hat{x}, \hat{y}, \hat{z}) \cdot \left(\frac{\overline{R}_i - \overline{R}_{i'}}{\left| \overline{R}_i - \overline{R}_{i'} \right|} \right) \tag{2.10}$$

By virtue of the harmonic analysis assumption, each spring is fixed to a designated axis and small deformations are assumed. In the next section, we solve for the dynamic response of a simple cubic structure using the Lagrangian lattice dynamics formulation presented above.

2.3 Implementation for a Simple Cubic Structure

The development of lattice dynamics within a Lagrangian mechanics framework provides a new process, and notation, for evaluating the equations of motion for a given crystalline material. This approach can be utilized for any lattice type; however, for simplicity, in this work we focus on a simple cubic structure where the primitive cell contains only a single mass. To allow for the eventual construction of a nanophononic crystal, we set up a *supercell* which consists of a collection of $N_x \times N_y \times N_z$ primitive cells extending along the x-y-z directions, respectively. Figure 2.1 (left) shows an example of a 3×3×3 supercell with the central mass (red) representing the basis of the unit cell. By incorporating the first three nearest neighboring masses, twenty-six neighboring pairs are found to contribute to the forces

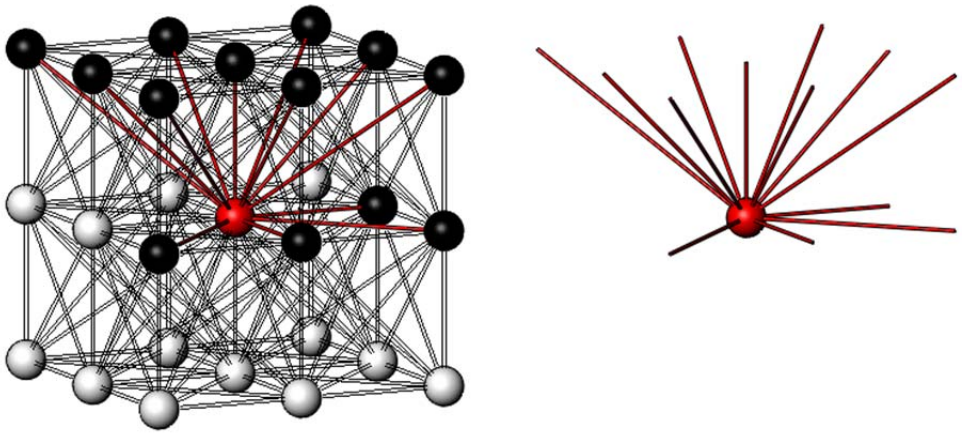

Figure 2.1: A basis atom [red] with three nearest neighbor interactions forming a 3×3×3 supercell (left). The supercell contains thirteen unique atom/spring pairs in the primitive unit cell (right).

applied by the central mass. Due to symmetry, only half of these interactions have unique geometrical directions within the lattice and are contained as part of the primitive unit cell [shown as red lines in Figure 2.1 (right)].

Following the Lagrangian formulation, the thirteen unique mass/spring pairs are individually identified and incorporated into the equations of motion. The neighboring interactions are contained within three groups: along the Cartesian axes containing three mass/springs (1,3,6), transverse and in-plane to the axes containing six mass/springs (2,4,5,7,8,9), and out-of-plane and diagonal to the axes containing four mass/springs (10,11,12,13) (see Figure 2.2 for an illustration).

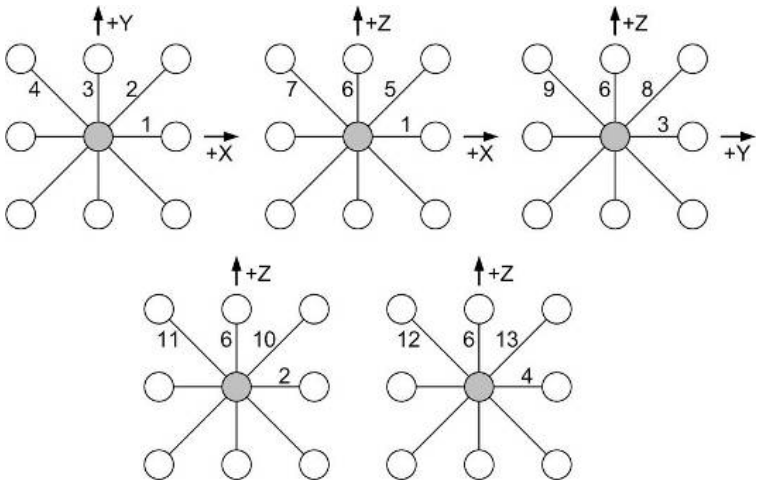

Figure 2.2: The atom/spring pair notation assignment graphically displayed as 2D slices of a 3×3×3 supercell.

These spring types can be referred to as the 1D, 2D and 3D interactions, respectively. To organize the resulting equations, a particular notation is adopted in line with similar practices in the literature [2,16]. The central mass of each unit cell is assigned an *i, j, k* index which represents the lattice position within the supercell in the *x*, *y*, *z* directions respectively. In addition, the thirteen springs are assigned a fourth index *l*, which identifies each unique spring type and varies from 1 to 13. Figure 2.2 shows planer slices of a 3×3×3 supercell and identifies the orientation of the thirteen unique spring types with respect to the

coordinate system *x*, *y* and *z*. Upon incorporating the Lagrangian approach described above with this 3D notation, the equations of motion can readily derived. The equations for the x-direction are shown in Eq. (2.11). The variables *u, v* and *w* denote the displacements in the *x, y*, and *z* directions respectively. Note that the one-half and one-third constants are formed by the lattice geometry from Eq. (2.10). In addition,

$$
\begin{aligned}
-m_{i,j,k}\ddot{u}_{i,j,k} &= k_{i,j,k,1}(u_{i,j,k}-u_{i+1,j,k})+k_{i-1,j,k,1}(u_{i,j,k}-u_{i-1,j,k}) \\
&+\frac{1}{2}k_{i,j,k,2}(u_{i,j,k}+v_{i,j,k}-u_{i+1,j+1,k}-v_{i+1,j+1,k}) \\
&+\frac{1}{2}k_{i-1,j-1,k,2}(u_{i,j,k}+v_{i,j,k}-u_{i-1,j-1,k}-v_{i-1,j-1,k}) \\
&+\frac{1}{2}k_{i,j,k,4}(u_{i,j,k}-v_{i,j,k}-u_{i-1,j+1,k}+v_{i-1,j+1,k}) \\
&+\frac{1}{2}k_{i+1,j-1,k,4}(u_{i,j,k}-v_{i,j,k}-u_{i+1,j-1,k}+v_{i+1,j-1,k}) \\
&+\frac{1}{2}k_{i,j,k,5}(u_{i,j,k}+w_{i,j,k}-u_{i+1,j,k+1}-w_{i+1,j,k+1}) \\
&+\frac{1}{2}k_{i-1,j,k-1,5}(u_{i,j,k}+w_{i,j,k}-u_{i-1,j,k-1}-w_{i-1,j,k-1}) \\
&+\frac{1}{2}k_{i,j,k,7}(u_{i,j,k}-w_{i,j,k}-u_{i-1,j,k+1}+w_{i-1,j,k+1}) \\
&+\frac{1}{2}k_{i+1,j,k-1,7}(u_{i,j,k}-w_{i,j,k}-u_{i+1,j,k-1}+w_{i+1,j,k-1}) \\
&+\frac{1}{3}k_{i,j,k,10}(u_{i,j,k}+v_{i,j,k}+w_{i,j,k}-u_{i+1,j+1,k+1}-v_{i+1,j+1,k+1}-w_{i+1,j+1,k+1}) \\
&+\frac{1}{3}k_{i-1,j-1,k-1,10}(u_{i,j,k}+v_{i,j,k}+w_{i,j,k}-u_{i-1,j-1,k-1}-v_{i-1,j-1,k-1}-w_{i-1,j-1,k-1}) \\
&+\frac{1}{3}k_{i,j,k,11}(u_{i,j,k}+v_{i,j,k}-w_{i,j,k}-u_{i-1,j-1,k+1}-v_{i-1,j-1,k+1}+w_{i-1,j-1,k+1}) \\
&+\frac{1}{3}k_{i+1,j+1,k-1,11}(u_{i,j,k}+v_{i,j,k}-w_{i,j,k}-u_{i+1,j+1,k-1}-v_{i+1,j+1,k-1}+w_{i+1,j+1,k-1}) \\
&+\frac{1}{3}k_{i,j,k,12}(u_{i,j,k}-v_{i,j,k}+w_{i,j,k}-u_{i+1,j-1,k+1}+v_{i+1,j-1,k+1}-w_{i+1,j-1,k+1}) \\
&+\frac{1}{3}k_{i-1,j+1,k-1,12}(u_{i,j,k}-v_{i,j,k}+w_{i,j,k}-u_{i-1,j+1,k-1}+v_{i-1,j+1,k-1}-w_{i-1,j+1,k-1}) \\
&+\frac{1}{3}k_{i,j,k,13}(u_{i,j,k}-v_{i,j,k}-w_{i,j,k}-u_{i-1,j+1,k+1}+v_{i-1,j+1,k+1}+w_{i-1,j+1,k+1}) \\
&+\frac{1}{3}k_{i+1,j-1,k-1,13}(u_{i,j,k}-v_{i,j,k}-w_{i,j,k}-u_{i+1,j-1,k-1}+v_{i+1,j-1,k-1}+w_{i+1,j-1,k-1})
\end{aligned}
\tag{2.11}
$$

note how the *x*-direction equations of motion do not accommodate the following spring numbers: 3, 6, 8, and 9 since these are contained within the *yz*-plane and are not influenced by motion along the *x*-direction. Symmetry within the model allows for replication in the remaining *y*- and *z*-directions.

A traveling wave solution is applied for each coordinate, as specified in Eqs. (2.12) through (2.14). In these equations, *A, B C* denote the amplitudes for each displacement component, γ the non-dimensional wavenumber, ω the lattice vibration frequency, *t* the time and *im* denoting an imaginary multiplier.

$$u_{i,j,k} = A_{i,j,k} e^{im\left[i\gamma_x + j\gamma_y + k\gamma_z - \omega t\right]} \tag{2.12}$$

$$v_{i,j,k} = B_{i,j,k} e^{im\left[i\gamma_x + j\gamma_y + k\gamma_z - \omega t\right]} \tag{2.13}$$

$$w_{i,j,k} = C_{i,j,k} e^{im\left[i\gamma_x + j\gamma_y + k\gamma_z - \omega t\right]} \tag{2.14}$$

The non-dimensional wavenumber is divided into components following the Cartesian coordinate system and is written in terms of the lattice wave number κ, lattice constant *a* (note for simple cubic system $a_x = a_y = a_z$), and the supercell size, i.e., N_x, N_y and N_z; see Eqs. (2.16) through (2.18). To enable periodic boundary conditions in the *x*-direction for a supercell of size N_x in the *x*-direction, the following relation holds: $A_{i-1}=A_{N_x}$ for $i=1$ and $A_{i+1}=A_1$ for $i=N_x$.

$$\gamma_x = \kappa a_x / N_x \tag{2.16}$$

$$\gamma_y = \kappa a_y / N_y \tag{2.17}$$

$$\gamma_z = \kappa a_z / N_z \tag{2.18}$$

Upon inserting Eqs. (2.12) through (2.14) into Eq. (2.11), a relationship for the motion of each mass can be determined for the *x*-direction in terms of wavevector and vibration frequency:

$$
\begin{aligned}
&-m_{i,j,k}\left(A_{i,j,k}(k_{AX,i,j,k}-\omega^2)+B_{i,j,k}k_{BX,i,j,k}+C_{i,j,k}k_{CX,i,j,k}\right)= \\
&+k_{i,j,k,1}(-A_{i+1,j,k}e^{im(\gamma_x)})+k_{i-1,j,k,1}(-A_{i-1,j,k}e^{im(-\gamma_x)}) \\
&+\frac{1}{2}k_{i,j,k,2}(-A_{i+1,j+1,k}e^{im(\gamma_x+\gamma_y)}-B_{i+1,j+1,k}e^{im(\gamma_x+\gamma_y)}) \\
&+\frac{1}{2}k_{i-1,j-1,k,2}(-A_{i-1,j-1,k}e^{im(-\gamma_x-\gamma_y)}-B_{i-1,j-1,k}e^{im(-\gamma_x-\gamma_y)}) \\
&+\frac{1}{2}k_{i,j,k,4}(-A_{i-1,j+1,k}e^{im(-\gamma_x+\gamma_y)}+B_{i-1,j+1,k}e^{im(-\gamma_x+\gamma_y)}) \\
&+\frac{1}{2}k_{i+1,j-1,k,4}(-A_{i+1,j-1,k}e^{im(\gamma_x-\gamma_y)}+B_{i+1,j-1,k}e^{im(\gamma_x-\gamma_y)}) \\
&+\frac{1}{2}k_{i,j,k,5}(-A_{i+1,j,k+1}e^{im(\gamma_x+\gamma_z)}-C_{i+1,j,k+1}e^{im(\gamma_x+\gamma_z)}) \\
&+\frac{1}{2}k_{i-1,j,k-1,5}(-A_{i-1,j,k-1}e^{im(-\gamma_x-\gamma_z)}-C_{i-1,j,k-1}e^{im(-\gamma_x-\gamma_z)}) \\
&+\frac{1}{2}k_{i,j,k,7}(-A_{i-1,j,k+1}e^{im(-\gamma_x+\gamma_z)}+C_{i-1,j,k+1}e^{im(-\gamma_x+\gamma_z)}) \\
&+\frac{1}{2}k_{i+1,j,k-1,7}(-A_{i+1,j,k-1}e^{im(\gamma_x+\gamma_z)}+C_{i+1,j,k-1}e^{im(\gamma_x-\gamma_z)}) \\
&+\frac{1}{3}k_{i,j,k,10}(-A_{i+1,j+1,k+1}e^{im(\gamma_x+\gamma_y+\gamma_z)}-B_{i+1,j+1,k+1}e^{im(\gamma_x+\gamma_y+\gamma_z)}-C_{i+1,j+1,k+1}e^{im(\gamma_x+\gamma_y+\gamma_z)}) \\
&+\frac{1}{3}k_{i-1,j-1,k-1,10}(-A_{i-1,j-1,k-1}e^{im(-\gamma_x-\gamma_y-\gamma_z)}-B_{i-1,j-1,k-1}e^{im(-\gamma_x-\gamma_y-\gamma_z)}-C_{i-1,j-1,k-1}e^{im(-\gamma_x-\gamma_y-\gamma_z)}) \\
&+\frac{1}{3}k_{i,j,k,12}(-A_{i+1,j-1,k+1}e^{im(\gamma_x-\gamma_y+\gamma_z)}+B_{i+1,j-1,k+1}e^{im(\gamma_x-\gamma_y+\gamma_z)}-C_{i+1,j-1,k+1}e^{im(\gamma_x-\gamma_y+\gamma_z)}) \\
&+\frac{1}{3}k_{i-1,j+1,k-1,12}(-A_{i-1,j+1,k-1}e^{im(-\gamma_x+\gamma_y-\gamma_z)}+B_{i-1,j+1,k-1}e^{im(-\gamma_x+\gamma_y-\gamma_z)}-C_{i-1,j+1,k-1}e^{im(-\gamma_x+\gamma_y-\gamma_z)}) \\
&+\frac{1}{3}k_{i,j,k,13}(-A_{i-1,j+1,k+1}e^{im(-\gamma_x+\gamma_y+\gamma_z)}+B_{i-1,j+1,k+1}e^{im(-\gamma_x+\gamma_y+\gamma_z)}+C_{i-1,j+1,k+1}e^{im(-\gamma_x+\gamma_y+\gamma_z)}) \\
&+\frac{1}{3}k_{i+1,j-1,k-1,13}(-A_{i+1,j-1,k-1}e^{im(\gamma_x-\gamma_y-\gamma_z)}+B_{i+1,j-1,k-1}e^{im(\gamma_x-\gamma_y-\gamma_z)}+C_{i+1,j-1,k-1}e^{im(\gamma_x-\gamma_y-\gamma_z)})
\end{aligned}
\tag{2.19}
$$

where

$$
\begin{aligned}
k_{AX,i,j,k} &= k_{i,j,k,1}+k_{i-1,j,k,1} \\
&+\frac{1}{2}(k_{i,j,k,2}+k_{i-1,j-1,k,2}+k_{i,j,k,4}+k_{i+1,j-1,k,4}+k_{i,j,k,5}+k_{i-1,j,k-1,5}+k_{i,j,k,7}+k_{i+1,j,k-1,7}) \\
&+\frac{1}{3}(k_{i,j,k,10}+k_{i-1,j-1,k-1,10}+k_{i,j,k,11}+k_{i+1,j+1,k-1,11}+k_{i,j,k,12}+k_{i-1,j+1,k-1,12}+k_{i,j,k,13}+k_{i+1,j-1,k-1,13})
\end{aligned}
\tag{2.20}
$$

$$
\begin{aligned}
k_{BX,i,j,k} &= \frac{1}{2}(k_{i,j,k,2}+k_{i-1,j-1,k,2}-k_{i,j,k,4}-k_{i+1,j-1,k,4}) \\
&+\frac{1}{3}(k_{i,j,k,10}+k_{i-1,j-1,k-1,10}+k_{i,j,k,11}+k_{i+1,j+1,k-1,11}-k_{i,j,k,12}-k_{i-1,j+1,k-1,12}-k_{i,j,k,13}-k_{i+1,j-1,k-1,13})
\end{aligned}
\tag{2.21}
$$

$$k_{CX,i,j,k} = \frac{1}{2}(k_{i,j,k,5} + k_{i-1,j,k-1,5} - k_{i,j,k,7} - k_{i+1,j,k-1,7}) + \frac{1}{3}(k_{i,j,k,10} + k_{i-1,j-1,k-1,10} - k_{i,j,k,11} - k_{i+1,j+1,k-1,11} + k_{i,j,k,12} + k_{i-1,j+1,k-1,12} - k_{i,j,k,13} - k_{i+1,j-1,k-1,13}) \quad (2.22)$$

These equations can be written as an eigenvalue problem shown in Eq. (2.23) where the $\tilde{S}$ matrix (i.e., the dynamical matrix) is defined with $\tilde{I}$ denoting an identity matrix. By solving for ω, the phonon frequency as a function of wavenumber can be determined.

$$\left[\tilde{S}(\gamma_x,\gamma_y,\gamma_z) - \omega^2\tilde{I}\right]\begin{bmatrix}\overline{A}\\ \overline{B}\\ \overline{C}\end{bmatrix} = 0 \quad (2.23)$$

2.4 Lattice Dynamics Comparison

The primary difference between the Newtonian and Lagrangian approaches is in the evaluation of the spring force constants and how the geometry of the lattice is incorporated. For the Newtonian lattice dynamics approach, the force potential is represented as 3×3 'force constant matrix' which inherently identifies each spring orientation. As a result, nine force constants are computed for every mass pair interaction. In the Lagrangian lattice dynamics formulation, each spring is geometrically aligned to a designated axis which enables in the need for only one force constant (i.e., elastic stiffness) for every mass pair interaction. This is defined within the equations of motion for each specific geometrical lattice configuration resulting in far fewer terms present in the governing equation.

The dispersion relation is generated using the two approaches for comparison. In these calculations, the distance inverse square scheme is utilized for the energy potential to determine the next-nearest neighboring force constants [20] with the 1st nearest neighbors set to unity. With the wave vector formulation set in terms of the Cartesian directions, a circuit around the Brillouin Zone for the simple

cubic lattice structure is established. Figure 2.3 shows the irreducible Brillouin Zone path used for our calculations. The magnitude of the wave vector can be written in terms of Eq. (2.24).

$$\gamma = \sqrt{\gamma_x^2 + \gamma_y^2 + \gamma_z^2} \tag{2.24}$$

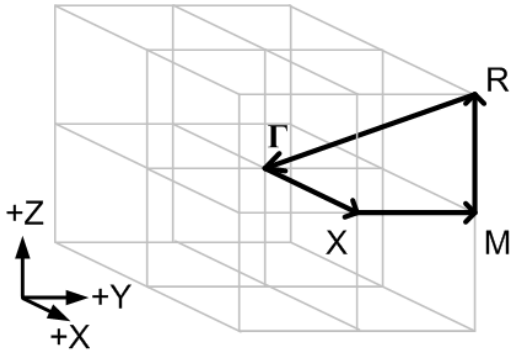

Figure 2.3: Irreducible Brillouin Zone wave vector path for a simple cubic structure. Point Γ has a value of [0,0,0] while point R has a value of $[\pi/N_x a_x, \pi/N_y a_y, \pi/N_z a_z]$. Here a_i is the lattice constant and N_i is the size of side i of the supercell for each Cartesian coordinate.

Figure 2.4 shows that the resulting dispersion curves based on both the Newtonian and Lagrangian formulations for a 3×3×3 supercell. Here the frequency Ω is non-dimensionalized. Clearly the two approaches yield an identical result, which verifies our Lagrangian lattice dynamics formulation.

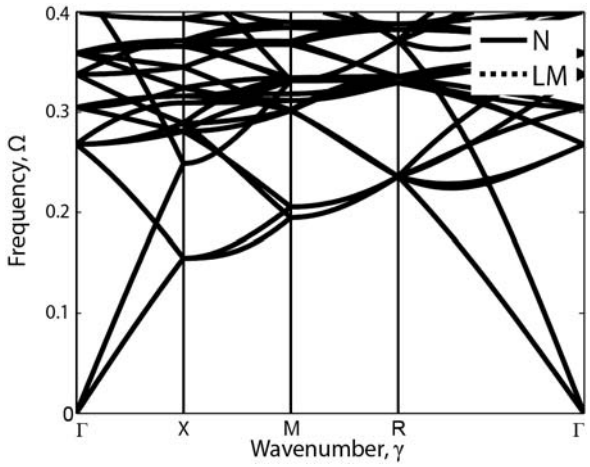

Figure 2.4: The dispersion relation comparison between the Newtonian (N) and Lagrangian Mechanics (LM) approaches for 3×3×3 supercell lattice.

2.5 Implementation of Superlattice Defects

The solution of Eq. (2.23) produces the dispersion relationship of the lattice structure for any wave vector γ. In the nominal "perfect" lattice case, (i.e., uniform mass arrangement), a band gap does not exist. However by including minor "defects" it is possible for band gaps to get generated. The size and quantity of defects can be used as a means to tune the band gap frequency location and range. To demonstrate this, the dispersion curves of two defected 5×5×5 lattice structures were calculated and compared to the "perfect" case. Similar to the dispersion plot shown in Figure 2.4, the distance inverse square scheme is utilized. The first modified scenario contains a single defect placed at the [3 3 3] location (center) shown

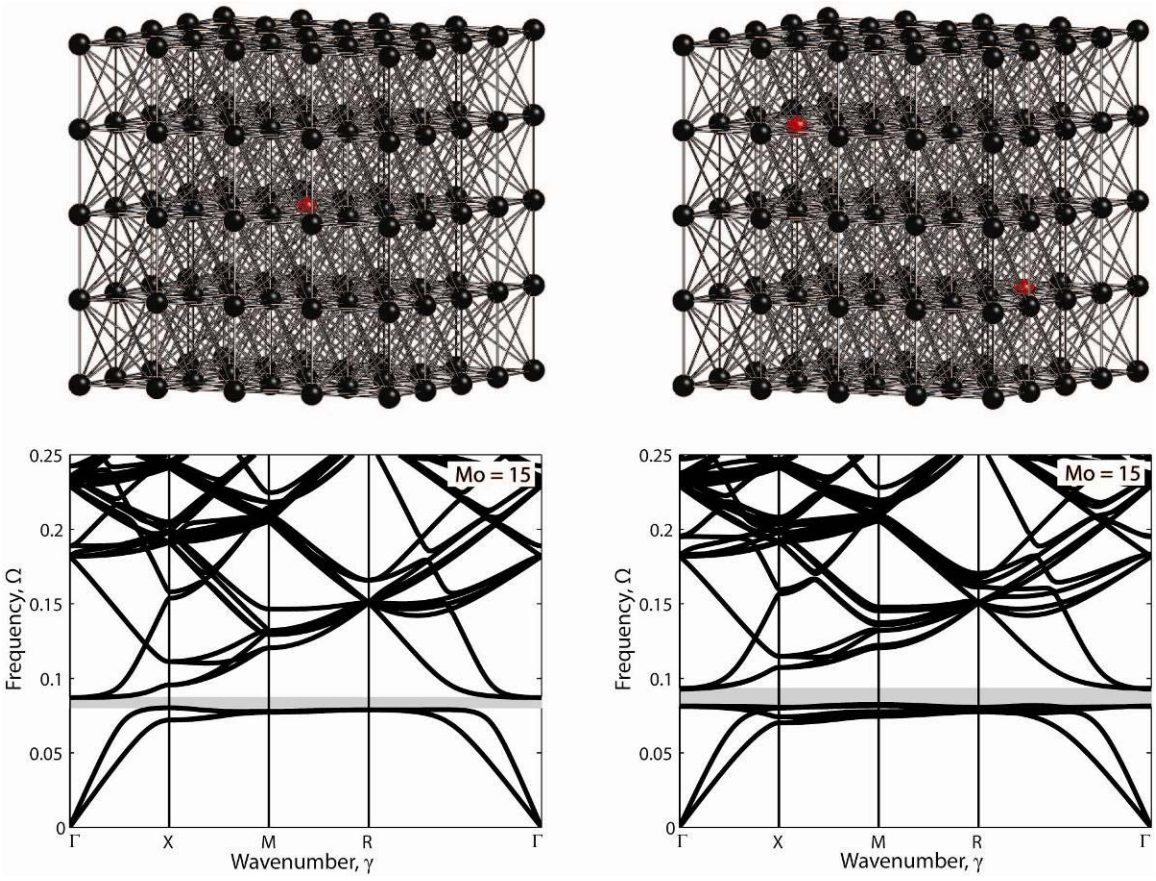

Figure 2.5: The dispersion relation for a 5×5×5 super cell with single defect [3 3 3] (left) and double defects [2 2 2], [4 4 4] (right). Here the ratio between the defect and the baseline mass $M_o = 15$.

in Figure 2.5 (left) and is given a mass value M_o that is fifteen times greater than the baseline mass. The second modified scenario contains two defects placed at the [2 2 2] and [4 4 4] locations shown in Figure 2.5 (right) and are each given the same mass ratio value.

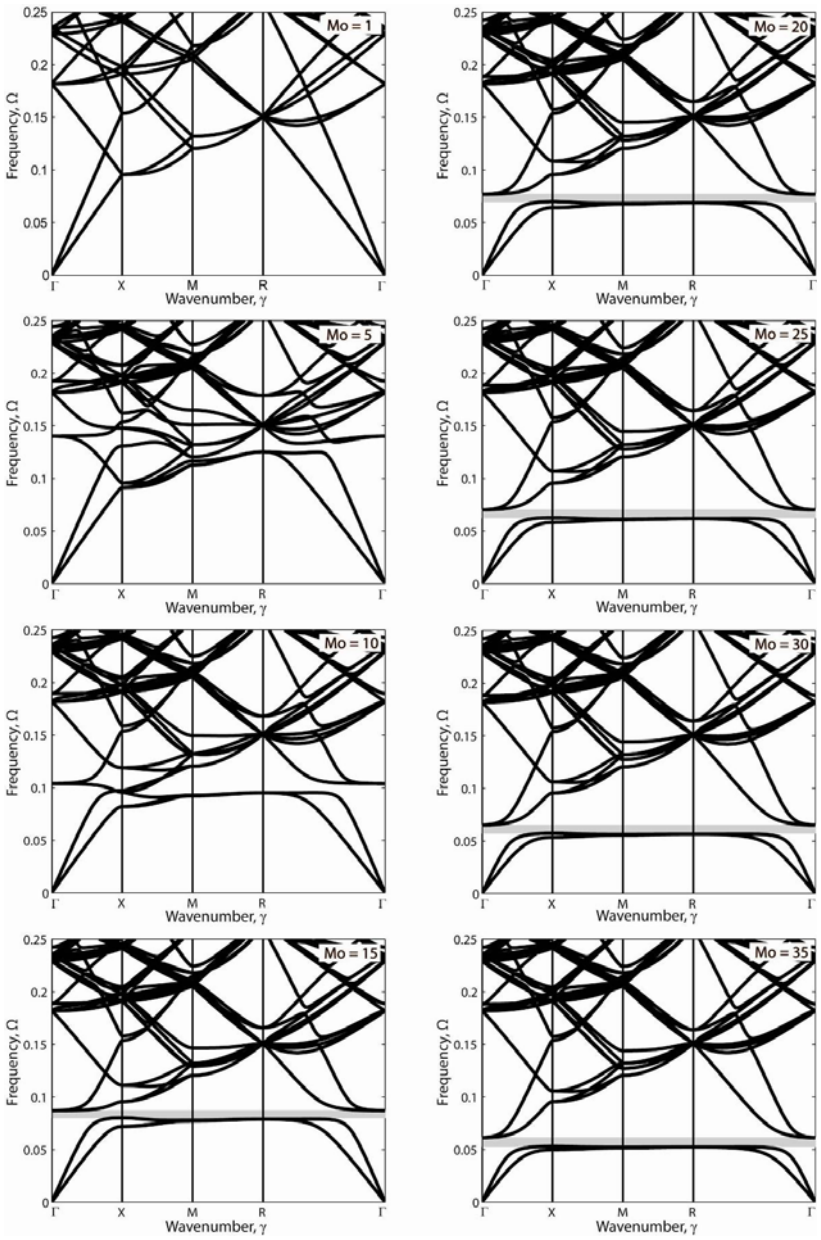

Figure 2.6: The dispersion relation for a 5×5×5 super cell with single defect. Here M_o is the ratio between the defect and the baseline mass and is varied to show its increasing impact on the range and location of the band gap.

In both scenarios, the dispersion curves are significantly altered due to the presence of the defect(s) and a formation of a band gap (a range where the wave propagation is prohibited) is observed. The presence of the band gap pushes down the acoustic branches and causes a splitting of the optical branches. The band structure for the two scenarios is given in Figure 2.5, where the shaded portion displays the band gap location.

The two defected scenarios contain band gaps which have varying size and range. To demonstrate the ability to control the bandgaps with a lumped parameter model, Figure 2.6 has been generated for the first defect scenario at multiple mass ratios. These two figures demonstrate the potential of controlling the frequency spectrum of the 3D nano-structured crystals. Techniques in phononic crystal optimization can lead to ultra-wide band gaps [21,23] which have numerous applications to control wave propagation.

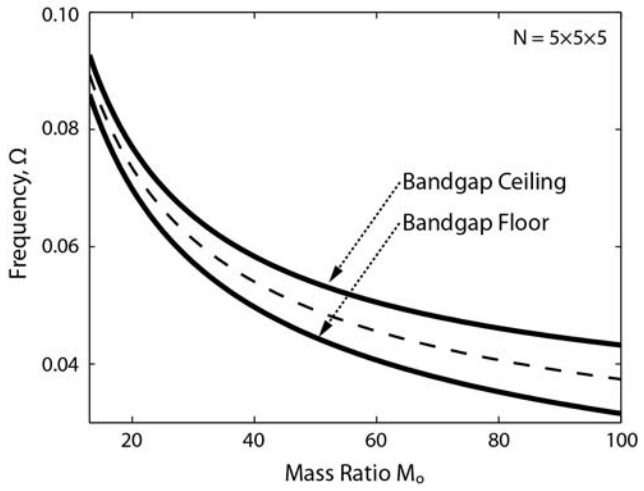

Figure 2.7: Band gap size and range as a function of mass ratio M_o for a 5×5×5 supercell. The upper (ceiling) and lower (floor) bounds of the band gap and center (dotted) are shown.

As the mass ratio increases the band gap range widens and becomes lower in frequency. This is illustrated in Figure 2.7 which shows the size of the band gap as a function of M_o. Figure 2.8 displays how this response is also affected by the supercell size in which we observe that the band gap shrinks when the M_o is held constant and the supercell size is increased. This is due to the change in the ratio of

the defected mass to the total mass in the supercell. Note that for the case of a 1×1×1 lattice spacing, there exists a band gap floor however no ceiling since the optical branches do not exist and at some critical $N \times N \times N$ value the band gap closes as the optical branches are pushed down and encroach the gap.

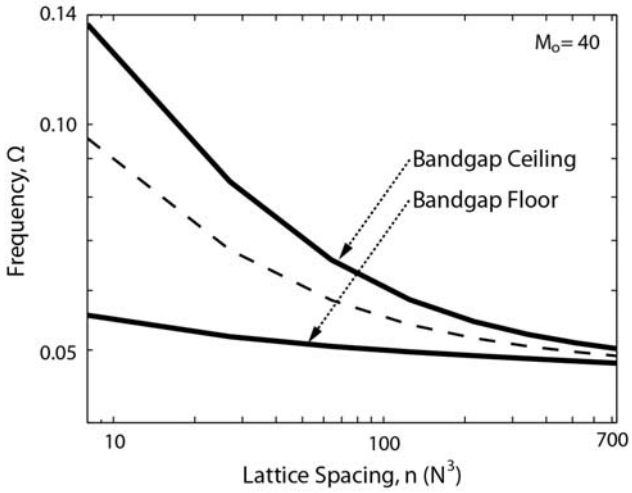

Figure 2.8: Band gap size and range as a function of lattice spacing n ($N*N*N$) for M_o=40. The upper (ceiling) and lower (floor) bound of the band gap and center (dotted) are shown.

2.6 Conclusion

Lattice dynamics analysis, or the dynamical analysis of atomic motion of a periodic medium, has broad applications in determining the wave propagation characteristics and the physical behavior of crystalline materials. This analysis is commonly used to model lattice vibrations at the nanoscale; however it also has analogous use in studying lumped-parameter phenomenon at the macroscale. In this paper we developed a lattice dynamics formulation within the Lagrangian mechanics framework to simplify how the inter-atomic force constants are defined within the equations of motion. Our proposed approach modifies the existing process by pinning each atomic interaction (in this case considered a spring force) to a designated axis. As a result, a single elastic constant is sufficient for this alternative formulation; simplifying the equations of motion from the existing Newtonian based approach which

utilizes nine force constants for each atomic pair interaction. Our formulation was demonstrated using a simple cubic lattice structure in which a single atom primitive cell was extended to form a supercell. This new formulation enables practical means for incorporating advanced phenomenon such as damping and non-linearity or the modeling of truncated periodic structures. Upon applying Bloch wave propagation conditions and computing the band structure dispersion relation, the two approaches were found to be consistent.

By understanding the relationship between unit cell structure and the dispersion curves, the ability to tune a lattice to allow or reject wave propagation at specific frequencies was presented. With a simple defect insertion process, it was shown that minor changes to a lattice structure can potentially have a large effect on the dispersion curves, specifically it can results in the opening of a band gap. With the enhancement of the inter-atomic potentials between the atoms and the utilization of optimization tools, the model presented in this study can be used for the design and study of nanostructured materials with dynamic properties tailored to specification. The defected supercells or phononic crystals studied within this paper provide a rich area of study with the ability to control wave propagation in numerous applications such as thermal transport at the nanoscale and phononic crystals at the macroscale

2.7 Appendix

2.7.1 Lattice Dynamics Formulation in a Newtonian Framework

The lattice dynamics formulation to calculate the phonon dispersion relation is documented below and follows a notation consistent with literature [22]. We begin by using Newtonian mechanics to balance the forces exerted on a central atom immersed within a lattice structure as discussed in Eq. (2.1). This can be written with a more specific notation for atom k in the lth primitive cell:

$$m_k \ddot{u}_\alpha(lk) = -\sum_{l'k'\beta} \Phi_{\alpha\beta}(lk;l'k') \cdot u_\beta(lk;l'k') \quad . \tag{A2.1}$$

Here m_k is the atomic mass, u is the displacement of atom lk with respect to an equilibrium position, t is time, Φ is a 3×3 inter-atomic force constant matrix, and $l'k'$ is an adjacent atom interacting with atom lk. The variables α, β represent the force interactions within an orthogonal coordinate system for the lattice structure and range from 1 to 3 for each direction: (1 for x, 2 for y, 3 for z). As a result, the force constant matrix contains a total of nine terms for each interaction. The summation term accounts for all neighboring atoms. The stiffness equations are formulated from a Taylor series expansion, however to abide by the harmonic assumption, only the second order term is evaluated. The number of nearest neighboring interactions desired determines the number of unit cells k' to be considered within the model. The force constant matrix for a two body harmonic stiffness potential can be assembled with the conditions of

$$\Phi_{\alpha\beta}(lk;l'k') = \begin{cases} -\varphi_{\alpha\beta}(lk;l'k') & lk \neq l'k' \\ \sum_{l''k''} \varphi_{\alpha\beta}(lk;l''k'') & lk = l'k' \end{cases} \tag{A2.2}$$

where the double prime term is present to account for the diagonal terms of the force constant matrix and are a summation over all interacting atoms. The inter-atomic stiffness potential φ is determined by taking the second derivative of the energy potential ϕ where, r is the inter-atomic separation distance (in

generalized coordinates), r_α, r_β are the Cartesian components and the with the prime notation denoting the spatial derivative.

$$\varphi_{\alpha\beta}(lk;l'k') = \left\{ \frac{r_\alpha r_\beta}{r^2}\left[\phi''_{kk'}(r) - \frac{1}{r}\phi'_{kk'}(r) \right] + \frac{\delta_{\alpha\beta}}{r}\phi'_{kk'}(r) \right\}\Bigg|_{r=x(lk;l'k')} \cong \frac{r_\alpha r_\beta}{r^2}\phi''_{kk'}(r) \tag{A2.3}$$

The resemblances between equations Eq. (A2.3) and Eqs. (2.8), (2.10) in the body of the text should be noted. For the purpose of this study, the first spatial derivative *ø'* is considered to be zero. To solve for a dynamic response, the traveling wave solution

$$u_\alpha(lk) = A_\alpha(k)e^{im[\kappa \bullet x(l) - \omega t]} \tag{A2.4}$$

is applied to the equations of motion where t is time, A is the mode shape, im denotes an imaginary multiplier, κ is the desired wave vector and ω is the phonon frequency. Note that the solution contains $3N$ (size of the unit cell * degrees of freedom per atom) mode frequencies and corresponding mode shapes for a given wave vector κ. The result can be written in terms of an eigenvalue problem

$$\left[\widetilde{D}(\kappa) - \omega^2(\kappa,\nu)\widetilde{I}\right]\overline{A}(\kappa,\nu) = 0 \tag{A2.5}$$

where $\widetilde{D}$is the dynamical matrix $\widetilde{I}$ an identity matrix and ν the mode (i.e. polarization) number. The formulation of the $3N \times 3N$ dynamical matrix is shown below.

$$D_{3(l-1)+\alpha,3(l'-1)+\beta}(ll',\kappa) = \frac{1}{\sqrt{m_l m_{l'}}}\sum_{k'}\Phi_{\alpha\beta}(l0,l'k')e^{im\{\kappa\cdot[r(l'k')-r(l0)]\}} \tag{A2.6}$$

The subscripts on the D matrix organize the placement of terms in a convenient form. Note that we are only modeling the primitive unit cell, thus the k index is set to zero over the summation and is the reason why this variable is not included in the subscript of the D matrix. The square root of the eigenvalues for $D(\kappa)$ matrix are the phonon mode frequencies with $3N$ solutions. Dispersion curves are

generated over a desired path by varying the wave number incrementally with wave numbers typically ranging from 0 to π/aN, where a is the lattice constant. Note, in symmetrical lattice systems, the solution often becomes degenerate reducing the total number of unique dispersion curve branches.

2.7.2 Nomenclature

Variables

r	atomic position, generalized coordinates [m],
r	atomic separation distance [m]
u	atomic position x-direction, **or** generic Cartesian atomic displacement [m]
v	atomic position y-direction [m]
w	atomic position z-direction [m]
R	atomic position (x,y,z) [m]
t	time [s]
m	mass [kg]
φ	atom-to-atom interatomic energy potential (immersed in a lattice) [J]
ϕ	linear atom-to-atom energy potential [J]
W	work [J]
Q	Total (generalized) force [N]
F	force [N]
q	generalized coordinate [unitless]
T	Kinetic Energy [J]
V	Potential Energy [J]
k	stiffness [N/m^2]
D	dynamical matrix [N/m^2]
I	identity matrix [unitless]
A	wave amplitude x-direction [m]
B	wave amplitude y-direction [m]
C	wave amplitude z-direction [m]
δ	delta (change) [uniteless]
γ	wavenumber [unitless]
κ	wavenumber [1/m]
υ	mode polarization [unitless]

ω	angular frequency [1/s]
im	imaginary multiplier (sqrt(-1))
Φ	Force constant matrix [F/m]
N	Number of primitive cells extended to forming a supercell [unitless]
M_o	Mass defect ratio [unitless]

Indicies (all integers)

i	supercell size, x-direction, **or** generic atomic index
j	supercell size, y-direction
k	supercell size, z-direction
k	adjacent supercell index (appendix only, follows Maradudin notation)
l	spring type
l	spring index (appendix only, follows Maradudin notation)
x	x-direction
y	y-direction
z	z-direction
n	number of generalized coordinates, total degrees of freedom per mass
α	orthogonal coordinate direction [1, 2 or 3], Force Constant Matrix 1
β	orthogonal coordinate direction [1, 2 or 3], Force Constant Matrix 2

Annotations

`	neighbour (i.e., neighbouring mass or supercell) **or** first spatial derivative
``	special case for summation, **or** second spatial derivative
~	denotes matrix
¯	denotes vector
^	coordinate direction
.	1st time derivative (d/dt)
..	2nd time derivative (d^2/dt^2)

2.8 Acknowledgements

The authors would like to thank Dr. Eduardo A. Misawa and the National Science Foundation for their support for this research under Grant No. CMMI 0927322.

2.9 References

[1] Horton, G. K. and Maradudin, A. A., Dynamical Properties of Solids, **1**, 1-82, (*Elsevier*, New York, New York 1974).

[2] Brillouin L., Wave Propagation in Periodic Structures, (*2nd Ed., Dover Publications Inc,* New York, New York 1953).

[3] Kittel C., Introduction to Solid State Physics, 8th Edition, (*Wiley*, New York, New York 2005).

[4] Dove M. T., Introduction to Lattice Dynamics, (*Cambridge University Press,* Cambridge, 1993).

[5] Dugas, R., History of Mechanics, (*Edition du Griffon*, Neuchatel, Switzerland, 1955).

[6] Brizard, A. J., An Introduction to Lagrangian Mechanics, (*World Scientific Publishing Company*, Singapore, 2008).

[7] McGaughey A. J. H., Hussein M. I., Landry E. S., Kaviany M. and Hulbert G. M., Phonon Band Structure and Thermal Transport Correlation in a Layered Diatomic Crystal, *Phys. Rev. B*, **74**, 104304 (2006).

[8] Turney, J. E., Laundry, E. S. and McGaughey, A. J. H., "Predicting Phonon Properties and Thermal Conductivity from Anharmonic Lattice Dynamics Calculations and Molecular Dynamics Simulations," *Phys. Rev. B*, **79**, 064301 (2009).

[9] Cao, J. X., Yan, X.H., Xiao, Y., Tang, Y. and Ding, J. W., "Exact Study of Lattice Dynamics of Single-Walled Carbon Nanotubes", *Phys. Rev. B*, **67**, 045413 (2003).

[10] Davis B. L. and Hussein M. I., Thermal Characterization of Nanoscale Phononic Crystals using Supercell Lattice Dynamics, *AIP Advances*, **1**, 041701 (2011).

[11] Tamura S., Tanaka Y. and Maris H., Phonon Group Velocity and Thermal Conduction in Superlattices, *Phys. Rev. B*, **60**, 2627 (1999).

[12] Gillet J. N., Chalopin Y. and Volz S., Atomic-Scale Three-Dimensional Phononic Crystals With a Very Low Thermal Conductivity to Design Crystalline Thermoelectric Devices, *J. of Heat Trans. ASME*, **131**, 043206 (2009).

[13] Cowley, R. A., "Lattice Dynamics and Phase Transitions of Strontium Titanate," *Phys. Rev.*, **134**, A981 (1964).

[14] Kern, G., Kresse, G. and Hafner, J., "Ab Initio Calculation of the Lattice Dynamics and Phase Diagram of Boron Nitride,' *Phys. Rev. B*, **59**, 8551 (1999).

[15] Wei-Wei, Z., Hong ,Y., Shuang-Ying, L. and Qing-An, H., Modeling of the Elastic Properties of Crystalline Silicon using Lattice Dynamics, *J. Phys. D: Appl. Phys.*, **44** 335401 (2011).

[16] Jensen J.S., Phononic Band Gaps and Vibrations in One- and Two-Dimensional Mass-Spring Structures, *Jour. Sound and Vib.*, **266**, 1053 (2003).

[17] Frazier, J. F. and Hussein, M. I., "Bloch-Theory-Based Analysis of Damped Phononic Materials," *Proceedings of the ASME 2011 International Mechanical Engineering Congress & Exposition* IMECE2011-**65662**, 1, Denver, Colorado (2011).

[18] Newton I., Naturalis Principia Mathematica, Book **II**, (1686).

[19] Lagrange, J.L., Mechanique Analytique, (*Chez la Veuve Desaint*, Paris 1788).

[20] Hepplestone, S. P. and Srivastava, G. P., "Hypersonic Modes in Nanophononic Semiconductors," Phys. *Rev. Letts.*, **101**, 105502 (2008).

[21] Hussein, M.I., Hamza, K., Hulbert, G. M. and Saitou, K., "Optimal Synthesis of 2D Phononic Crystals for Broadband Frequency Isolation," *Waves in Random and Complex Media*, **17**, 491 (2007).

[22] Maradudin, A. A., Montroll, E. W., Weiss, G. H. and Ipatova, I. P., Theory of Lattice Dynamics in the Harmonic Approximation, (*2nd Academic*, New York 1963).

[23] Bilal O. R. and Hussein M. I., Topologically Evolved Phononic Material: Breaking the World Record in Band Gap Size, *Proc. of SPIE*, **8269**, 826911-1 (2011).

3 THERMAL CHARACTERIZATION OF NANOSCALE PHONONIC CRYSTALS USING SUPERCELL LATTICE DYNAMICS

Journal Version:
*AIP Advances, **1** 041701, 2011*

3.0 Abstract

The concept of a phononic crystal can in principle be realized at the nanoscale whenever the conditions for coherent phonon transport exist. Under such conditions, the dispersion characteristics of both the constitutive material lattice (defined by a primitive cell) and the phononic crystal lattice (defined by a supercell) contribute to the value of the thermal conductivity. It is therefore necessary in this emerging class of phononic materials to treat the lattice dynamics at both periodicity levels. Here we demonstrate the utility of using supercell lattice dynamics to investigate the thermal transport behavior of three-dimensional NPCs formed from silicon and cubic voids of vacuum. The periodicity of the voids follows a simple cubic arrangement with a lattice constant that is around an order of magnitude larger than that of the bulk crystalline silicon primitive cell. We consider an atomic-scale supercell which incorporates all the details of the silicon atomic locations and the void geometry. For this supercell, we compute the phonon band structure and subsequently predict the thermal conductivity following the Callaway-Holland model. Our findings dictate that for an analysis based on supercell lattice dynamics to be representative of the properties of the underlying lattice model, a minimum supercell size is needed along with a minimum wave vector sampling resolution. Below these minimum values, a thermal conductivity prediction of a bulk material based on a supercell will not adequately recover the value obtained based on a primitive cell. Furthermore, our results show that for the relatively small voids and void spacing we consider (where boundary scattering is dominant), dispersion at the phononic crystal unit cell level plays a noticeable role in determining the thermal conductivity.

3.1 Introduction

3.1.1 Nanoscale Phononic Crystals

The concept of phonon engineering of nanoscale structures has been a topic of intense research in recent years, [e.g., 1-7]. Among the various phonon engineering strategies considered is the utilization of phononic crystals at the nanoscale (i.e., *nanoscale phononic crystals* or NPC) to provide a means for controlling the phonon transport properties. PnCs are periodic composite materials that consist of more than one phase (usually at least one phase is a solid and the other(s) are solid, fluid or gas). Numerous applications have been developed for PnCs in the macroscopic regime, e.g., elastic or acoustic waveguiding [8] and focusing [9], vibration minimization [10], sound collimation [11], frequency sensing [12,13], acoustic cloaking [14], acoustic rectification [15] and optomechanical waves coupling in photonic devices [16]. The realization that phononic crystals can now be sized at the nanoscale to influence atomic-scale phonons is opening up a new direction in nanoscale heat transfer and material design [17-28]. For example, among the configurations considered is the insertion of periodic holes in silicon slabs [24-26,28]. Should the conditions of coherent transport exist in such configurations, phonon waves can in principal linearly interfere while simultaneously experience nonlinear scattering events [see [21] for an analysis on the interplay between the effects of dispersion and anharmonic scattering in a one-dimensional NPC]. The technological implications of tuning this phenomenological interplay are indeed significant. For example, it is conceivable that a phononic crystal with a relatively large lattice spacing (as considered in Refs. [24,26]) may exhibit a reduction in thermal conductivity without a significant impact on the scattering of electrons – a favorable outcome for increasing the figure-of-merit of thermoelectric materials [29,30].

3.1.2 Supercell Lattice Dynamics and Thermal Conductivity Prediction

There is an assortment of classical approaches available for the prediction of the phonon thermal conductivity of crystalline materials. Some of these approaches are based on analytical models such as the Callaway-Holland formulation [31,32] or the Boltzmann transport equation [33]. Scattering data is often obtained from experiments or using molecular (MD) simulations [34]. Another approach employs MD simulations followed by the application of the Green Kubo method (in the case of equilibrium simulations) or the Fourier law of heat conduction (in the case of non-equilibrium simulations), (see Ref. [22] for a comparison). While simulations provide direct predictions and hence alleviate the need for making assumptions concerning material and boundary scattering, analytical models provide physical insight into the various factors that contribute to the thermal conductivity.

In NPCs, it is essential to identify the role that the dispersion plays in the overall phonon thermal transport. Naturally this has to be done at both the primitive lattice and PnC lattice levels. A unit cell at the PnC level would constitute a supercell from the perspective of the primitive lattice. *Supercell lattice dynamics* information can be incorporated into a phenomenological model, e.g., the Callaway-Holland [31,32] model, to obtain an estimate of the thermal conductivity. One of the obstacles to this approach, however, is the fact that the band structure of a supercell exhibits multiple foldings of the dispersion branches – the larger the supercell the smaller is the size of the Brillouin Zone and subsequently the more intense, and often overwhelming, the foldings are. Furthermore, additional dispersion branches appear due to the increase in cell size (and therefore the number of atomic motion degrees of freedom).

3.1.3 Overview

In this paper we examine the utility of using the concept of an atomic-scale supercell and how it can be reliably used for the prediction of the thermal conductivity of a NPC. As a case study, we consider a configuration formed from silicon and cubic voids of vacuum laid out in a simple cubic arrangement. We choose to focus on small sizes, that is, the lattice constant of the PnC is around only an order of

magnitude larger than that of the bulk crystalline silicon primitive cell. The supercell for this configuration incorporates, by definition, all the details of the silicon atomic locations and the void geometry. We carry out lattice dynamics calculations for this supercell (employing the Tersoff interatomic potential) and subsequently use the Callaway-Holland model to predict the thermal conductivity. We consider the distance between the voids as a representative length scale for boundary scattering and use experimental data for bulk silicon to fit the material-related time relaxation parameters. Our aims are (1) to determine the requirements on the supercell size and the wavenumber sampling rate for the thermal conductivity predictions to be adequate, and (2) to investigate the role that dispersion plays at the supercell level in determining the thermal conductivity (for the case where the phononic crystal unit cell is relatively small and boundary scattering is dominant over material scattering). The main part of the paper is divided into two sections. Section 3.2 provides a thorough explanation of the primitive and conventional unit cell structures of bulk silicon and presents the Callaway-Holland approach for the prediction of the thermal conductivity from phonon dispersion. Here the influence of the acoustic and transverse dispersive branches on thermal conductivity is identified as well as the relative contributions of the boundary, Umklapp and impurity scattering terms. Section 3.3 considers unit cells of NPCs. It first presents supercell lattice dynamics calculations and analysis, and then covers the corresponding thermal conductivity predictions and an examination of the role of dispersion under a state of dominant boundary scattering. In section 3.4, conclusions are provided followed by a brief outlook on the promise of repeating the present study on larger unit cells as well as of using these cells as *building blocks* for the development of nanoscale thermal waveguides, a key component in a future device based on phononics.

3.2 Bulk Silicon

3.2.1 Primitive Cell: Structure and Lattice Dynamics

This study focuses on silicon-based NPCs, however to understand the underlying physics of wave dispersion and scattering we must first consider the most basic lattice forming the material's atomic structure, that is, the lattice described by a primitive cell. A bulk silicon primitive cell contains two base atoms embedded in a face-centered cubic (FCC) structure. A choice of primitive cell lattice vectors forms a basis with a common angle of 60 degrees; here the length scale of interest is that of the atomic separation distance, a_p = 0.38 nm (Figure 3.1a). It is convenient (for treating the bulk material and later when we consider the PnC lattice) to extend this primitive cell along these axes to form an eight-atom conventional cell which is cubic in shape. Here the lattice vectors are redefined as an orthogonal basis with a conventional cell lattice constant of a = 0.54 nm (Figure 3.1b). Figure 3.1c displays a cut along the

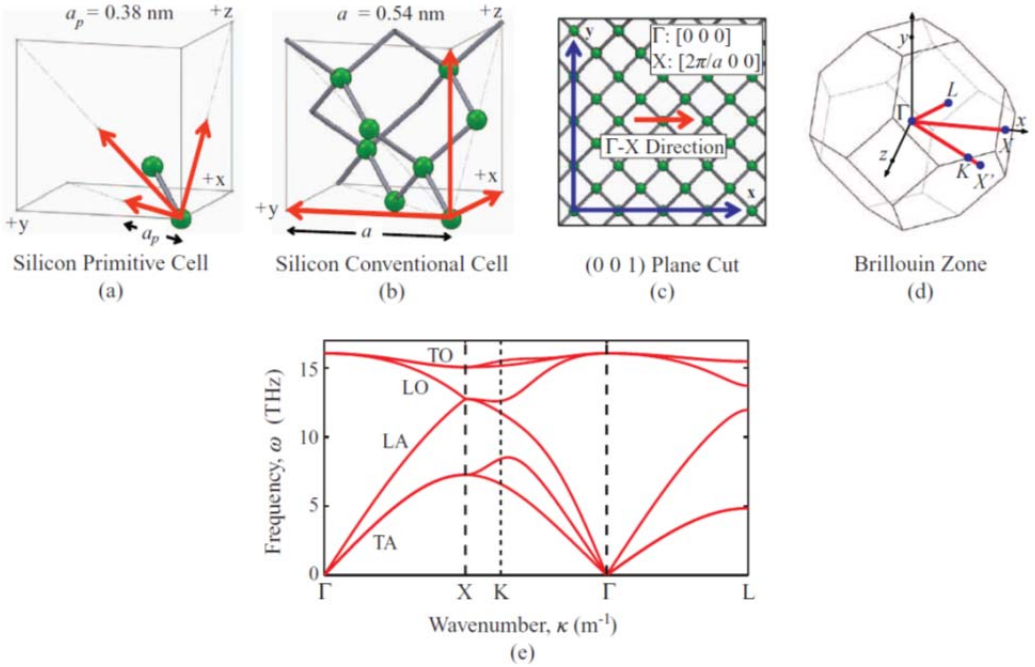

Figure 3.1: Phonon dispersion of silicon: (a) 2-atom primitive cell and corresponding lattice vectors, (b) 8-atom conventional unit cell and corresponding orthogonal lattice vectors, (c) a slice through the silicon crystal (001) plane with the orthogonal coordinate system shown and the Γ-X direction labeled, (d) FCC Brillouin Zone and symmetry points, (e) bulk dispersion (based on primitive cell).

direction of the planes of a conventional cell. The Brillouin Zone of the FCC structure is a truncated octahedron (Figure 3.1d). For our lattice dynamics and subsequent thermal conductivity calculations in this section we focus on the Γ-X wavevector path bordering the edge of the irreducible FCC Brillouin Zone (Figure 3.1d).

The phonon dispersion of isotropic silicon is formulated utilizing the General Utility Lattice Program [35) (details of the lattice dynamics formulation are available at Refs. [36,37]). For all cases reported in this paper, the three-body Tersoff potential is used for the Si-Si bonds with only the first nearest neighboring interactions considered [38,39]. Prior to calculating the dispersion, the energy is minimized at constant pressure to relax the structure and ensure stability. This is especially relevant when boundary edges (caused by voids when forming the NPC) are introduced. The Broyden-Fletcher-Goldfarb-Shanno (BFGS) optimization method [40] is used for this purpose.

Figure 1e displays the dispersion curves based on the primitive unit cell, i.e., the phonon band structure for bulk silicon, showing good agreement with measurements [41]. There are six dispersion branches, two pairs of which are degenerate along the Γ-X path, namely those corresponding to the transverse acoustic (TA) and transverse optical (TO) modes. There is only one polarization for each of the longitudinal acoustic (LA) and longitudinal optical (LO) modes along the same path.

3.2.2 Primitive Cell: Thermal Conductivity

In this study, the thermal conductivity of silicon is predicted by the Callaway-Holland model [31,32], as given by Eq. (3.1). This model determines the thermal conductivity k by summing over each dispersion branch λ an integral function evaluated over the non-dimensional wave vector $\boldsymbol{q}$. The integrand involves the phonon volumetric specific heat $C_p(\boldsymbol{q},\lambda)$, the square of the phonon group velocity $\boldsymbol{v}(\boldsymbol{q},\lambda)$ and the phonon scattering relaxation time $\tau(\boldsymbol{q},\lambda)$. The velocity is dotted with unit vector $\boldsymbol{l}$, to define the direction of interest for the phonon transport.

$$k = \sum_{\lambda} \int C_p(\boldsymbol{q},\lambda)(\boldsymbol{v}(\boldsymbol{q},\lambda)\cdot\boldsymbol{l})^2 \tau(\boldsymbol{q},\lambda)\, d\boldsymbol{q}. \tag{3.1}$$

Since we are interested in the Γ-X direction, we re-write Eq. (3.1) to incorporate the dimensional lattice constant, a, within the variable of integration $\boldsymbol{q}$, i.e., $d\boldsymbol{q} = d\boldsymbol{\kappa}\, a / 2\pi$. The factor of 2π stems from location of point X within the Brillouin Zone geometry of face-centered cubic structures. This conversion enables us to write the heat capacity, C_{ph}, in Joules per Kelvin, thus we get

$$k = \frac{1}{(2\pi)^3} \sum_{\lambda} \int C_{ph}(\boldsymbol{\kappa},\lambda)(\boldsymbol{v}(\boldsymbol{\kappa},\lambda)\cdot\boldsymbol{l})^2 \tau(\boldsymbol{\kappa},\lambda)\, d\boldsymbol{\kappa}. \tag{3.2}$$

The material is assumed to be isotropic allowing for the variable of integration to be evaluated over the volume of a sphere and expressed as a scalar, that is,

$$\int d\boldsymbol{\kappa} = 4\pi \int_0^{2\pi/a} \kappa^2 d\kappa. \tag{3.3}$$

This is essentially an approximation to the near-spherical shape of the first Brillouin Zone. As for the dot product in Eq. (3.2), this becomes $(\boldsymbol{v}(\boldsymbol{\kappa},\lambda)\cdot\boldsymbol{l}) = v/\sqrt{3}$. The final form of the Callaway-Holland expression for an isotropic FFC crystal along the Γ-X path (0 to $2\pi/a$) is

$$k = \frac{4\pi/3}{(2\pi)^3} \sum_{\lambda} \int_0^{2\pi/a} C_{ph}(\kappa,\lambda) v^2(\kappa,\lambda) \tau(\kappa,\lambda) \kappa^2 d\kappa. \tag{3.4}$$

In Eq. (3.4), the heat capacity C_{ph} measures the energy of each phonon mode and incorporates the Boltzmann-Einstein distribution to account for quantum effects at low wavenumbers:

$$C_{ph}(\kappa,\lambda) = k_B \left(\frac{\hbar\omega(\kappa,\lambda)}{k_B T} \right)^2 \frac{\exp(\hbar\omega(\kappa,\lambda)/k_B T)}{\left[\exp(\hbar\omega(\kappa,\lambda)/k_B T) - 1\right]^2}. \tag{3.5}$$

Here k_B is the Boltzmann constant, $\hbar$ is the reduced Plank's constant, and T is the temperature. The phonon group velocity is evaluated by taking the derivative of the phonon frequency with respect to the wavenumber:

$$v(\kappa,\lambda)=\frac{\partial\omega(\kappa,\lambda)}{\partial\kappa}. \tag{3.6}$$

Finally the phonon scattering relaxation time can be broken into three components identifying the type of scattering mechanism: Umklapp τ_U, impurity τ_I and boundary τ_B. The inverse of these variables are summed via Matthiessen's rule to give the overall scattering time:

$$\begin{aligned}\tau(\kappa,\lambda) &= (\tau_U^{-1}(\kappa,\lambda)+\tau_I^{-1}(\kappa,\lambda)+\tau_B^{-1}(\kappa,\lambda))^{-1}\\ &= (AT\omega^2(\kappa,\lambda)e^{-B/T}+D\omega^4(\kappa,\lambda)+c/L)^{-1}.\end{aligned} \tag{3.7}$$

The boundary scattering is dependent on the longitudinal speed of sound in the crystal, c [more accurately evaluated as $v(\kappa,\lambda)$], and the minimum feature length L which can be viewed as a characteristic length scale based on the size and distribution of boundaries, grains, voids, etc. In our calculation of the thermal conductivity of single crystal bulk silicon, we simply omit the τ_B term in Eq. (3.7) because L is effectively equal to infinite in this case. The impurity scattering is frequency dependent and is described by the parameter D which we obtain from the literature. Specifically, we use D = 1.32x10^{-45} s^3 [42]. The Umklapp scattering, which is associated with phonon-phonon interactions, is temperature and frequency dependent. This term is described by two parameters, A and B, which we obtain by fitting to measurements of bulk silicon thermal conductivity. For this we use experimental data reported in the literature [43,44] and attain the following values: A = 2.1e^{-19} sK^{-1} and B = 180 K (see Figure 3.2). With this information, and using the phonon dispersion shown in Figure 3.1d, we predict the thermal conductivity of single crystal bulk silicon to be 142 W/mK, close to the widely reported value of

148 W/mK [44]. In this paper (unless otherwise specified) we consider the material to be at room temperature or 300º K.

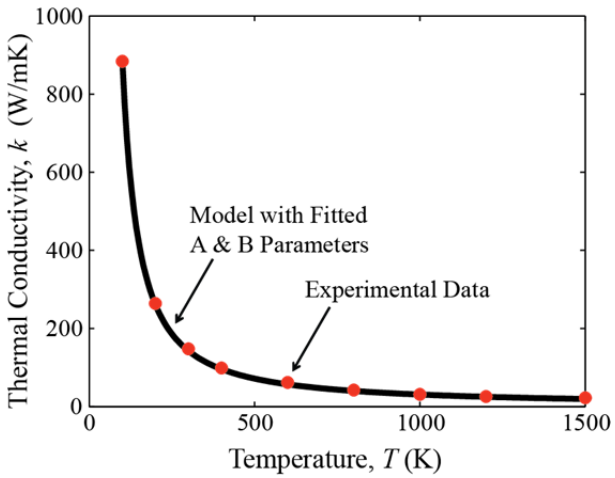

Figure 3.2: Thermal conductivity of bulk silicon calculated from the Callaway-Holland model with fitted *A* & *B* parameters (solid line) matching empirical data [43,44] from macro-scale silicon (dots). *Reprinted with permission from J. Phys. Ref. Data 1, 279 (1972). Copyright 1972 American Institute of Physics and from John Wiley & Sons, Inc. F. P. Incropera and D. P. DeWitt, Fundamentals of Heat and Mass Transfer (Wiley, Hoboken, NJ, 2002).*

When we keep the boundary scattering term, the thermal conductivity drops in the manner shown in Figure 3.3a. Here *L* may be viewed, for example, as the average grain size in a bulk polycrystalline silicon. The graph demonstrates that when *L* is small (i.e., in the order of nanometers) a dramatic reduction in the thermal conductivity occurs. This is an obvious outcome because internal boundaries (such as grain boundaries) inhibit the propagation of phonons and subsequently a small value of *L* leaves very few propagating phonons to carry energy though the crystal. We refer to this as the *dominant boundary scattering* regime. On the contrary, at large scales (i.e., $L > 0.1$mm) the boundary scattering mechanism begins to fade compared to the other mechanisms. This is deduced from Matthiessen's rule (Eq. 3.7) and demonstrated in Figure 3.3a. Furthermore, we can explicitly decompose the contributions of the acoustical and optical branches (as governed by Eq. (3.4), and demonstrated in Figure 3.3a), or even the contribution of each individual branch on its own (Figure 3.3b). We observe that for bulk silicon

the acoustic branches dominate the contribution to the thermal transport and the longitudinal modes are more influential than the transverse modes.

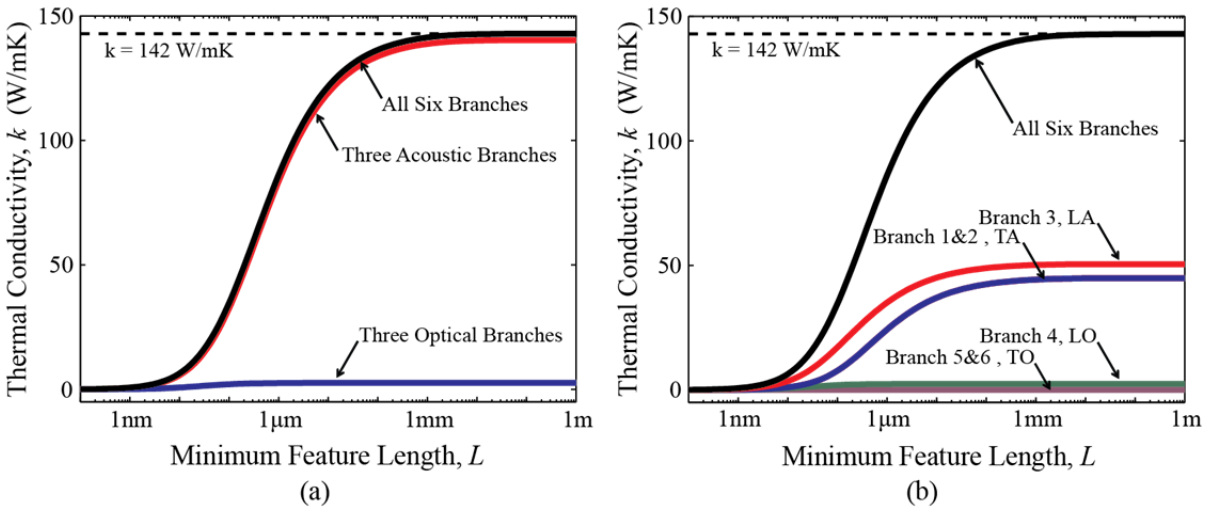

Figure 3.3: Thermal conductivity of bulk silicon (based on primitive cell) with varying minimum feature length (black) over the Γ-X direction, (a) Contributions of the three acoustical (red) and optical branches (blue) are identified, (b) Contributions of the longitudinal acoustic (red), transverse acoustic (blue), longitudinal optical (green) and transverse Optical (purple) branches are identified.

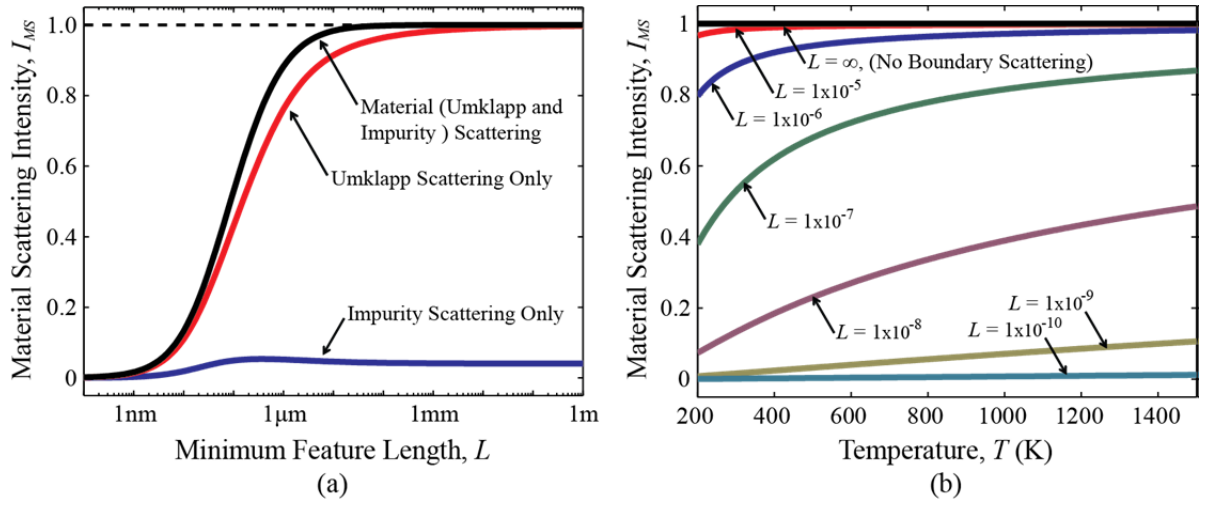

Figure 3.4: Material scattering intensity representing the influence of Umklapp and impurity scattering on the thermal conductivity of bulk silicon, (a) contribution of both Umklapp and impurity scattering (black), contribution of Umklapp scattering only (red), contribution of impurity scattering only (red), (b) effect of temperature for various minimum feature lengths L.

We can further investigate the scattering mechanisms within the Callaway-Holland model by looking directly at the role of material (Umklapp & impurity) scattering. For this purpose, we introduce the *material scattering intensity ratio*,

$$I_{MS} = (k_{NMS} - k)/k_{NMS}, \tag{3.8}$$

which compares the thermal conductivity, k (calculated normally), to the thermal conductivity, k_{NMS}, which is a prediction in which either one or both material scattering relaxation times are "turned off". This quantity is shown for bulk silicon in Figure 3.4a, for the cases of combined and individual elimination of Umklapp & impurity scattering. A high value of I_{ms} indicates $k_{NMS} \gg k$ and hence a large original role of the eliminated mechanism(s) in lowering the thermal conductivity. On the contrary, a low value of I_{ms} indicates a low contribution of material scattering. Consistent with Figure 3.3, at small minimum feature lengths L the material intensity is low due to boundary scattering dominance. However as L increases, there is a rapid shift in intensity until L becomes so large that the potency of boundary scattering diminishes. We note that the influence of Umklapp scattering is far superior to impurity scattering (according to our choices of the A, B and D parameters) although it saturates at a higher value of minimum feature length. Additional insight on material scattering can be gained by varying temperature as shown in Figure 3.4b. Since impurity scattering is not dependent on temperature, the trends seen here are of Umklapp scattering alone. When $L = \infty$, Umklapp scattering is dominant over boundary scattering at all temperatures. As L is reduced, we observe that I_{ms} drops. This drop is most profound at low temperatures because Umklapp scattering weakens at low temperatures. The curves in Figure 3.4b provide a quantitative view of these effects.

Figures 3.3 and 3.4 demonstrate, in different ways, the relative contributions of boundary and material scattering as the minimum feature size changes. Figure 3.3 shows us specifically the role of boundary scattering, as a function of minimum feature length L, without explicitly addressing the role of

material scattering. Figure 3.3, 3.4 on the other hand provides us with an explicit indication of the role of material scattering as a function of the minimum feature length. According to Figure 3.3, the thermal conductivity starts to flatten when the minimum feature length falls below $L \approx 11$ nm. From the point of view of material intensity, on the other hand, we observe in Figure 3.4 that the flattening starts to take place when the minimum feature length falls below $L \approx 5$ nm. In the following section we will examine the behavior of NPCs with void spacing distances ranging from 2.2 nm to 3.2 nm which according to Figures 3 and 4 is clearly a regime where boundary scattering is dominant over material scattering. We will examine the effect of the PnC crystal dispersion on the thermal conductivity in this regime.

3.3 Silicon Based Nanoscale Phononic Crystals

3.3.1 Supercells: Structure and Lattice Dynamics

We now turn to the main focus of this work which is silicon-based three-dimensional (3D) NPCs. The avenue of nanostructuring bulk silicon in order to alter the thermal transport properties was considered by Bux [45], although the focus there was on grain control and the introduction of particulates. While such an approach leads to increased scattering and hence significant reduction in thermal conductivity, it does not provide a means of property control via dispersion. NPCs on the other hand offer the possibility of reducing thermal conductivity via a combination of boundary scattering *and* dispersion-dependent coherent and incoherent mechanisms (through the introduction of additional periodicity). Consequently, and as mentioned earlier, NPCs can potentially serve as an outstanding candidate for thermoelectric materials by tuning the PnC lattice spacing to be large enough not to impede the electron transport yet small enough to desirably couple with the phonon transport at the atomic scale. In this paper we model a PnC unit cell as a supercell that incorporates all the atomic-level information of the underlying primitive lattice.

The concept of an atomic supercell has been studied by Hepplestone et al. [46] where they considered different reduced-dimension configurations of silicon. In their supercell lattice dynamics calculations they modeled bulk unit cells with a special treatment for the outer atoms to extract the configuration of the reduced dimension structure of interest. Gillet et al. [23] also considered dispersion calculations of supercells, specifically in the context of silicon-germanium quantum-dot materials. However no conditions, or convergence analysis, were provided for proper utilization of the supercell model.

In this section we start with a conventional cell, as depicted in Figure 3.1b, and extend it along orthogonal lattice vectors to create a supercell. The prior transition we made from the two-atom primitive system depicted in Figure 3.1a into the eight-atom conventional cell is necessary because it allows us to analyze simple cubic shapes and hence be able to conveniently insert symmetrical voids. The side length N is the number of conventional cells that are extended along each direction. For example, a $N = 2$ supercell contains 8 conventional cells or 64 atoms as illustrated in Figure 3.5 in which the extended conventional cells are shaded. To solve for the dispersion, the lattice dynamics model undergoes

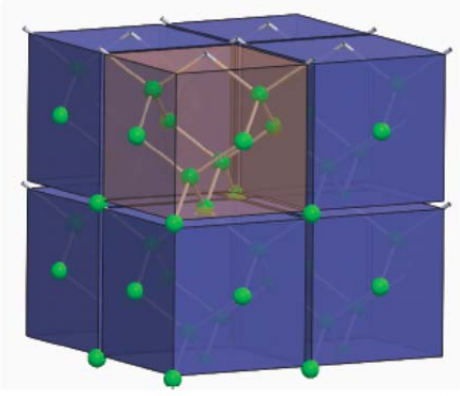

Figure 3.5: Formation of a supercell formed from a 2×2×2 array of conventional cells. Here the conventional cell contains eight atoms and is extended along an orthogonal coordinate system to create a sixty-four atom supercell.

modifications (compared to application on a primitive cell) to incorporate the new geometry and the resizing of the Brillouin Zone. The Brillouin Zone decreases in size by a factor proportional to the difference in size between the conventional and primitive cells and also the number of conventional cells making up the supercell. Compared to the primitive cell, the dispersion branches of a supercell of size $N \times N \times N$ become folded, increasing the difficulty of identifying specific branches (especially for large supercells). Furthermore, additional dispersion branches appear due to the increase in the cell size (and therefore the number degrees of freedom associated with the added atoms). However, in principle, these two factors do not diminish the value of the supercell band structure and complex processes for unfolding and explicitly handling the additional branches are unnecessary as we will demonstrate later.

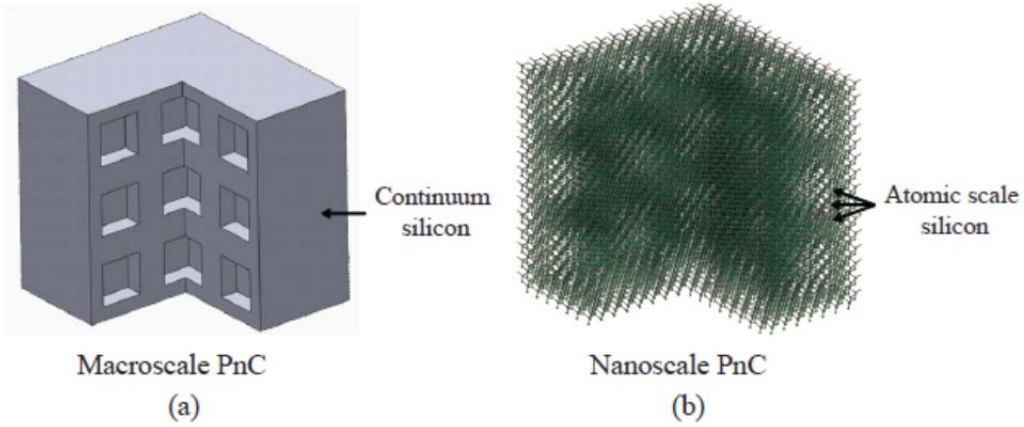

Figure 3.6: Macroscale versus NPC based on silicon, (a) macroscale continuum model (scalable), (b) atomistic model (discrete, scale fixed by atomic spacing).

Upon the formation of a large supercell, we create a NPC by inserting a cubic void at the center of the supercell. Other void shapes and supercell symmetries may be considered, but this is beyond the scope of the current study. Here it is appropriate to draw an analogy with conventional macroscale PnCs [47-49]. Figure 3.6a illustrates an example of a 3D macroscale PnC, suitably modeled as a continuum. Such a model is scale-independent and hence can be used for PnCs spanning a wide range of length scales from

meters down to the point where the continuum hypothesis breaks down. As mentioned earlier, this class of PnCs is finding numerous applications across disciplines [8-16]. At the nanoscale, however, atomic-scale phenomena cannot be neglected, and hence the necessity to model the PnC unit cell as a non-scalable supercell that incorporates all the atomic information as mentioned above (Figure 3.6b).

To examine the effect of inserting a void in a supercell (to create a NPC) on the phonon band structure, we first consider a $N = 5$ supercell. With no void, this supercell describes a cube of bulk silicon containing one thousand atoms with a side length (i.e., NPC unit cell length) of $A = 2.7$ nm. It should be noted that N and A are related by the function: $A = Na$. We now insert cubic voids (to ensure 3D symmetry) and consider a series of void sizes, enumerated in increments of conventional cells, (i.e., 1×1×1, 2×2×2, 3×3×3 and 4×4×4). This generates four unique NPC unit cells to study, each containing 992, 936, 784 and 488 atoms, respectively. We measure the size of the void by volume fraction v_f which we obtain by dividing the number of removed atoms by the total number of atoms of the bulk supercell.

Figure 3.7 shows the lowest few dispersion branches for all these cases (for the Γ-M wavevector path as illustrated at the top of the figure). We can notice clearly the effect of the branch folding (as well as the additional branches due to the added degrees of freedom) in the $v_f = 0$ case. As the volume fraction increases, the initially degenerate dispersion branches diverge, flatten and shift in frequency at varying rates. Some branches shift upwards and others drop. An important observation from the point of view of thermal conductivity is that as the voids increase in size the slopes of the branches – the acoustic modes in particular – decrease, which means reductions in the group velocities and hence a lowering of the energy carrying capacity in the NPC as a whole.

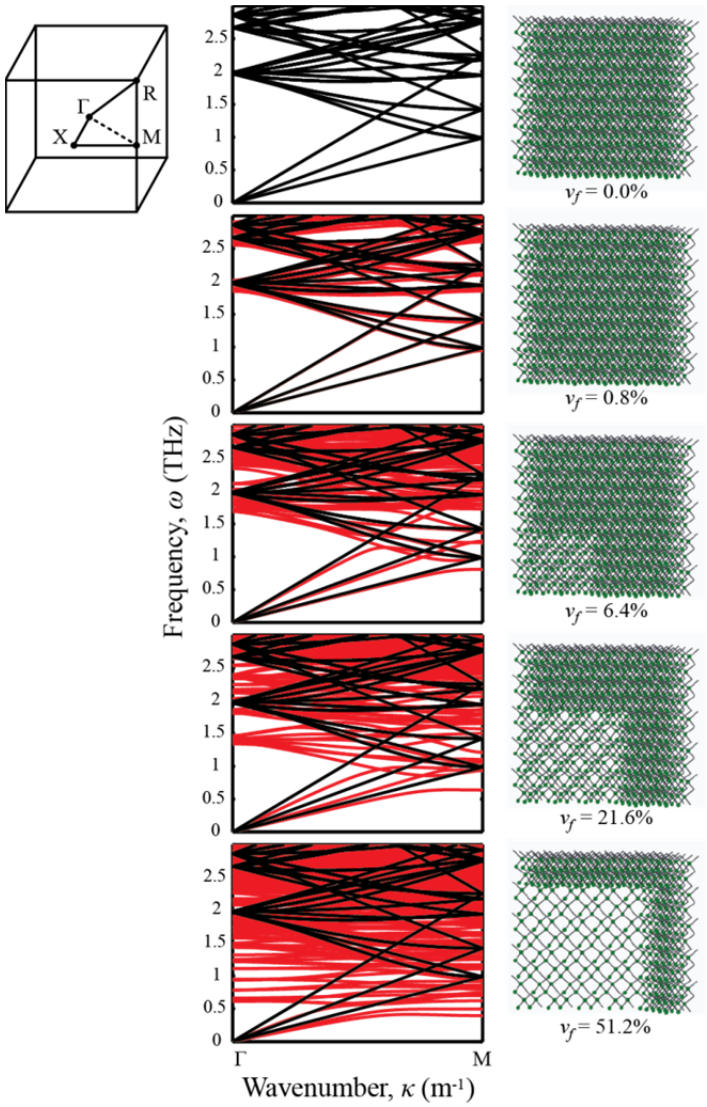

Figure 3.7: Dispersion of an $N = 5$ ($A = 2.7$ nm) supercell for various volume fractions v_f. The curves for the nominal case (Bulk, $v_f = 0\%$) are in black and the curves for the NPC (for different values of v_f) are in red. The Brillouin Zone for the cubic supercell is shown.

3.3.2 Supercells: Thermal Conductivity

In this section we use the Callaway-Holland model to predict the thermal conductivity of NPCs of the type depicted in Figure 3.7. We now use a different version of Eq. (3.4) to suit our cubic PnC unit cell, and furthermore we arbitrarily choose to compute the thermal conductivity in the Γ-M direction (as shown in the top of Figure 3.7). The Callaway-Holland model for our supercell calculations is therefore as follows

$$k = \frac{4\pi/3}{(\pi/\sqrt{2})^3}\frac{1}{R_{dof} f_{gs}}\sum_{\lambda}\int_0^{\pi/(a\sqrt{2})} C_{ph}(\kappa,\lambda)v^2(\kappa,\lambda)\tau(\kappa,\lambda)\kappa^2 d\kappa, \tag{3.9}$$

where R_{dof} denotes the ratio of the number of degrees of freedom in the conventional cell to that in the primitive cell (for silicon, R_{dof} = 4), and f_{gs} is a geometric shape factor to account for the difference in geometry between a sphere (which is the shape of our domain of integration) and a cube (which is the shape of the actual Brillouin Zone for the supercells we are considering). From our subsequent analysis, we find that the optimal value for f_{gs} is 2. We note that the evaluation of the thermal conductivity in Eq. (3.9) involves a summation of the integrals over all dispersion branches that we obtain from the supercell lattice dynamics calculations. In practice all the function evaluations are executed numerically. In the primitive cell case, we have clearly identifiable branches to integrate over. This however is not the case for a supercell since there is typically a large number of branches (due to the foldings and the added degrees of freedom) as observed in the band diagrams displayed in Figure 3.7. Moreover, there are numerous crossings among these branches which from a mathematical point of view render the individual branch functions discontinuous. Even if we were to abandon tracking a particular branch based on its type and only follow each branch on the basis of its order at each κ-point, we will face numerous non-smooth junctures. If not accounted for, this issue will introduce significant errors during the process of numerical differentiation (to obtain the group velocities as given in Eq. (3.6) and consequently the supercell-based thermal conductivity calculations will not be accurate.

In order to examine the utility of the supercell lattice dynamics approach we carry out a series of reference calculations on cubic supercells of bulk silicon (i.e., no voids). For ease of calculation, we still approximate the κ-space domain of integration to a spherical volume as indicated above. As shown in Figure 3.8, we observe that as we increase the supercell size (represented by the value of N) and the κ-space sampling resolution (represented by the number of sampling points, n_κ, per Γ-M wave vector

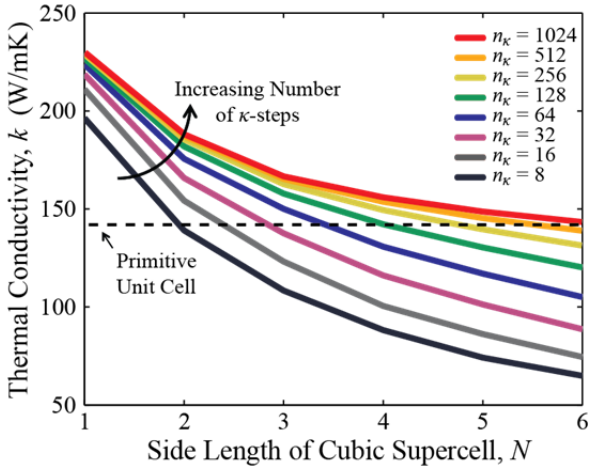

Figure 3.8: Thermal conductivity of bulk silicon based on bulk N×N×N supercells as a function of supercell size N and κ-space sampling resolution n_κ. The thermal conductivity of bulk silicon based on a primitive cell (benchmark calculation) is shown at k = 142 W/mK (dashed line).

sweep), the supercell-based thermal conductivity prediction convergences to the nominal value of 142 W/mK that corresponds to our primitive cell-based prediction. As mentioned earlier, in evaluating the supercell-based thermal conductivity using the Callaway-Holland model, there will be errors stemming from the difficulties in handling the non-smooth junctures in the dispersion branches. There will also be an error in the overall prediction stemming from the difference in the shape of the integration domain (between a sphere and a cube). In Figure 3.8, the converging behavior for a given value of n_κ suggests that these errors get increasingly minimized as N increases. As for the role of n_κ for a given value of N, it is evident (also from Figure 3.8) that its increase is necessary for convergence. This is because increasing the κ-space resolution is equivalent to refining the step size in the numerical evaluation of the integrands in Eq. (3.9) which in turn leads to reducing the error in evaluating the group velocities near the branch crossings. It should be noted that for a given value of n_κ, the κ-space resolution increases as N increases (because the size of the Brillouin Zone decreases). However, it is clear from Figure 3.8, that increasing N alone is not sufficient to achieve convergence hence *both* an increase in N and an increase in n_κ are

needed. While the analysis of Figure 3.8 focuses on bulk silicon, the conditions discussed for convergence naturally extend to the analysis of voided supercells.

To summarize, the concept of supercell lattice dynamics can be employed for the thermal conductivity prediction of NPCs only when the following conditions are met: (1) *the supercell size has to be equal to or larger than a minimum threshold size*, and (2) *the wave vector sampling resolution has to be equal to or higher than a minimum threshold resolution*. The value of these minimum thresholds depends on the level of convergence (and hence degree of accuracy) desired in the predictions.

For our bulk silicon model, we observe that a minimum supercell size of $N_{min} = 6$ and a minimum κ-space sampling resolution of $n_{\kappa,min} = 1024$ steps yield a prediction that is within 1% of the nominal value of 142 W/mK. However, for the calculations presented in the rest of the paper, we select $N_{min} = 4$ and $n_{\kappa,min} = 128$ to speed up our computations, assuming that the error induced with these selections is tolerable especially when the PnC crystal predications are normalized with respect to the supercell-based bulk material predictions.

With regards to the scattering parameters for the NPCs analysis, we incorporate the distance between the voids as a representative length scale for boundary scattering. For the supercell sizes we consider in this work, this length scale is small compared to the mean free path associated with Umklapp scattering and this renders boundary scattering as the dominant nonlinear interaction mechanism (as the results of Figures 3.3 and 3.4 assert). As such, the accuracy level of the Umklapp scattering parameters will not significantly affect the values of the predicted thermal conductivity. This in turn allows us to use, as an approximation, experimental data for bulk silicon to fit the material-related time relaxation parameters A and B (as done in Section 3.2.2). For the calculations to follow, we establish a notation for the different thermal conductivity quantities we obtain as listed in As expected, the small size of the NPC lattice spacing (and consequently L) results in a significant reduction of thermal conductivity (the colored dots in Figure 3.9). The inset provides greater detail for the trends for each supercell size. Clearly, the PnC

thermal conductivities are lower than the corresponding bulk silicon with boundary scattering; furthermore, the slopes decrease as the value of A increases which is attributed to the change in dispersion as the void size increases. An exponential function,

. As a reference, we first calculate $k_{BS}^{B/Prim}$, which is the primitive cell-based thermal conductivity of bulk silicon with boundary scattering

Table 3.1: Thermal conductivity calculations terminology for different cases studied.

	Primitive	**Supercell**	
	Bulk	Bulk (No Voids)	PnC (Voids)
No Boundary Scattering	$k_{NBS}^{B/Prim}$	$k_{NBS}^{B/SC}$	$k_{NBS}^{PnC/SC}$
Boundary Scattering	$k_{BS}^{B/Prim}$	$k_{BS}^{B/SC}$	$k_{BS}^{PnC/SC}$

incorporated, and normalize this quantity using $k_{NBS}^{B/Prim}$, which is the prediction for a bulk single crystal (i.e., no boundary scattering included). The purpose of the normalization here is to remove errors stemming from the supercell analysis (see Figure 3.8). The result, which is similar to Figure 3.3, is plotted as a function of L in Figure 3.9. We then consider several NPCs with different unit cell sizes, A = 2.2, 2.7 and 3.2 nm (corresponding to N = 4, 5 and 6 respectively), and different void volume fractions. Here, the minimum feature length L is determined to be the distance between adjacent voids. The supercell-based thermal conductivity predictions for these configurations, $k_{BS}^{PnC/SC}$, are normalized with respect to $k_{NBS}^{PnC/SC}$ (the same quantity with no boundary scattering incorporated) and also plotted versus L in Figure 3.9.

As expected, the small size of the NPC lattice spacing (and consequently L) results in a significant reduction of thermal conductivity (the colored dots in Figure 3.9). The inset provides greater detail for the

trends for each supercell size. Clearly, the PnC thermal conductivities are lower than the corresponding bulk silicon with boundary scattering; furthermore, the slopes decrease as the value of A increases which is attributed to the change in dispersion as the void size increases. An exponential function,

$$\frac{k_{BS}^{PnC/SC}}{k_{NBS}^{PnC/SC}} = 8x10^{-6}\, e^{(Ln)}, \tag{3.10}$$

is fitted to provide a quantitative assessment of this role that the dispersion plays (under conditions of boundary scattering dominance). We did not investigate larger NPC unit cells due computational limitations. However, we expect the trends shown in the inset to remain bounded from above by the thermal conductivity of the bulk material with boundary scattering.

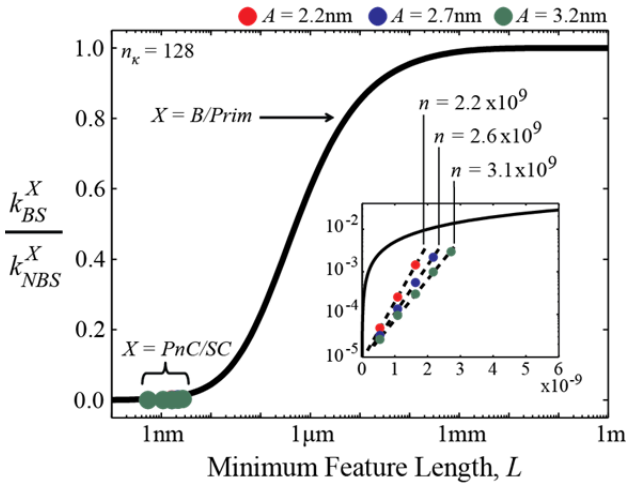

Figure 3.9: Primitive cell-based thermal conductivity calculations for bulk silicon with boundary scattering $\boldsymbol{k_{BS}^{B/PrC}}$ normalized with respect to the same with no boundary scattering $\boldsymbol{k_{NBS}^{B/PrC}}$ (black curve), and supercell-based thermal conductivity calculations for the NPCs with boundary scattering $\boldsymbol{k_{BS}^{PnC/SC}}$ for A = 2.2, 2.7 and 3.2 nm normalized with respect to the same with no boundary scattering $\boldsymbol{k_{NBS}^{PnC/SC}}$ (colored dots). The red and blue dots are obscured by the green dots. Inset provides a closer view of the data points for the NPC. The exponent n from the exponential fit of Eq. (3.10) is provided for the various A values. All supercell calculations were obtained using a κ-space sampling resolution of n_κ = 128.

The thermal conductivity predictions of the NPCs, with ($k_{BS}^{PnC/SC}$) and without ($k_{NBS}^{PnC/SC}$) boundary scattering, are shown as a function of volume fraction in Figure 3.10. Here, the plots are normalized with respect to the prediction for bulk silicon based on a supercell without (Figure 3.10a) and with (Figure 3.10b) boundary scattering incorporated, i.e., with respect to $k_{NBS}^{B/SC}$ and $k_{BS}^{B/SC}$, respectively. The purpose of the normalizations is to again remove the errors stemming from the supercell analysis, but also to allow us to isolate the effect of dispersion in the thermal conductivity trends. For the case including boundary scattering and normalized with respect to the no-boundary scattering bulk silicon predictions (the bottom curve in Figure 3.10a), an increase in volume fraction induces a rather profound reduction in thermal conductivity. The dominating cause of this behavior is the decreasing minimum feature length which is the distance between the voids (this distance decreases as the void size increases for a fixed value of A). On the contrary, for the case where boundary scattering is not considered, and again the normalization is

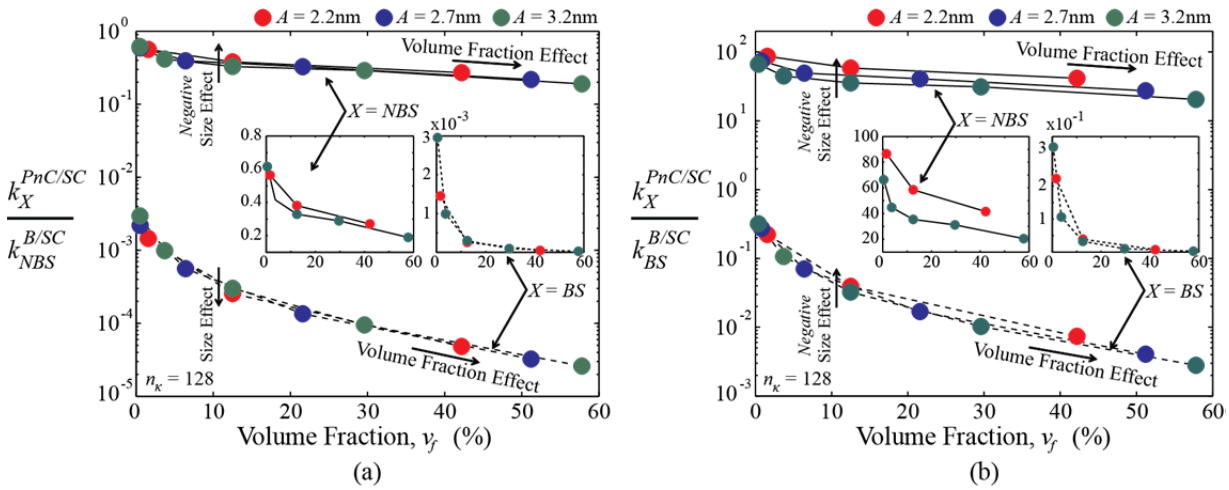

Figure 3.10: Supercell-based thermal conductivity calculations for the NPCs without boundary scattering $\boldsymbol{k_{NBS}^{PnC/SC}}$ (solid black) and with boundary scattering $\boldsymbol{k_{BS}^{PnC/SC}}$ (dashed black), both normalized with respect to a supercell-based thermal conductivity calculation for bulk silicon with (a) no boundary scattering $\boldsymbol{k_{NBS}^{B/SC}}$ incorporated or with (b) boundary scattering incorporated $\boldsymbol{k_{BS}^{B/SC}}$. Three supercell sizes, A = 2.2, 2.7 and 3.2 nm, are analyzed with varying volume fractions. Insets provide a closer view of the two sets of curves in each subfigure. Arrows are included to refer to observed size effects (positive and negative). All supercell calculations were obtained using a κ-space sampling resolution of n_κ = 128.

with respect to no-boundary scattering bulk silicon predictions (top curve in Figure 3.10a), the reduction in thermal conductivity is dictated by the phonon dispersion alone. We note that the reduction in this case is moderate compared to the lower curve in the same figure. In Figure 3.10b, the bottom curves also shed light on the effect of dispersion because it displays results incorporating boundary scattering that are normalized with respect to bulk silicon predictions in which boundary scattering is also incorporated. Hence these curves describe the isolated effect of dispersion in the presence of boundary scattering. They show an appreciable effect although, as expected, much less than what is observed in the lower curves in Figure 3.10a (noting the logarithmic axes). The top curves in Figure 3.10b are included for completeness.

We note that for the case of incorporation of boundary scattering in Figure 3.10a, a decrease in unit cell size (from A = 3.2 nm to A = 2.2 nm) leads to a reduction in the thermal conductivity at v_f = 12.5%. This is indicative of a classical size effect (where the thermal conductivity decreases with decreasing size). On the other hand, when only dispersion is considered, i.e., the top curves in Figure 3.10a, we observe an increase in the thermal conductivity for the same decrease in unit cell size at the same volume fraction. This suggests that when dispersion is considered in isolation of boundary scattering, a *negative size effect* emanates. This conclusion is also supported by the bottom curves in Figure 3.10b where the effect of dispersion has been isolated in the presence of boundary scattering and, furthermore, is consistent with the slopes trend shown in the inset of Figure 3.9.

Finally, the relationship between material scattering intensity and temperature of the NPCs and bulk silicon (both with boundary scattering incorporated) is shown in Figure 3.11. Here we consider NPC supercells with a size of N = 6 where the red, blue and green solid lines correspond to a void size of 2×2×2, 3×3×3, 4×4×4 (in units of number of conventional cells) or a volume fraction of 3.7, 12.5 and 29.6% respectively. The dashed lines correspond to bulk silicon modeled also using a supercell with a size of N = 6. For both the solid and dashed lines three different values of minimum feature size are incorporated: $L = 4a_f$, $3a_f$ and $2a_f$. For the NPCs these values of L represent the distance between the

voids, whereas for the bulk material these values of L are imposed (and can be thought of, for example, as average grain sizes in a polycrystal). We recall from Figure 3.4b how the temperature-dependent role of material scattering fades away as the minimum feature size is decreased. Figure 3.11 shows that the deterioration of this role intensifies in a NPC, an outcome that can only be attributed to the effect of dispersion.

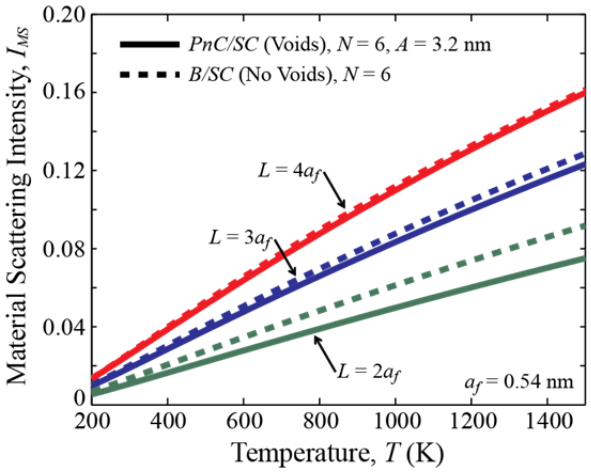

Figure 3.11: Material scattering intensity versus temperature for NPCs (solid lines) and bulk silicon (dashed lines) for three different values of L. For the NPCs, a supercell of size $N = 6$ is used and L is incorporated as the distance between the voids. For comparison, the same supercell size and the same values of L are incorporated in the bulk silicon predictions. All calculations were obtained using a κ-space sampling resolution of $n_\kappa = 128$.

3.4 Conclusions

In this paper we analyzed the concept of *supercell lattice dynamics* as a tool for the characterization of the thermal conductivity of NPCs on the basis of the Callaway-Holland model. Using a supercell of bulk silicon as a reference problem, we have shown that the thermal conductivity prediction converges to the value obtained using the primitive cell when (1) the supercell size N increases, and (2) the κ-space sampling resolution (represented by n_κ) increases. The minimum chosen value of each of these parameters collectively determines the extent to which the prediction is representative of the properties of the underlying lattice model.

Upon investigating the effects of boundary and material scattering in bulk silicon using primitive cell lattice dynamics, we employed our supercell-based approach towards the analysis of NPCs in sizes in which the dominant incoherent mechanism is boundary scattering. First we demonstrated that the phonon band structure of a NPC supercell is significantly different from that of a corresponding bulk material supercell. We then showed that under conditions of dominant boundary scattering, the dispersion of the NPC clearly plays a role in reducing the thermal conductivity – although most of the reduction is attributed to the boundary scattering itself as expected. Moreover, this role, when viewed in isolation, causes a *negative* size effect in which the thermal conductivity increases, rather than decreases, with reduction in PnC unit cell size.

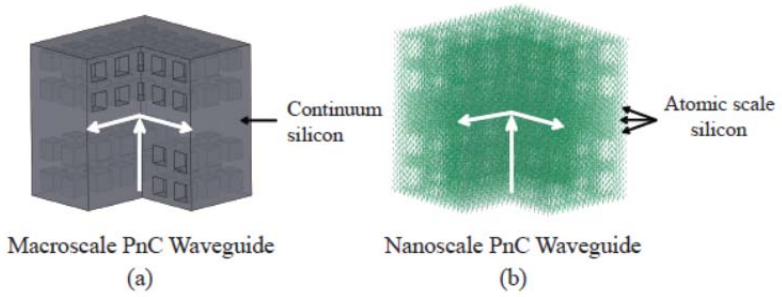

Figure 3.12: PnC waveguides, (a) conventional macroscale PnC waveguide, (b) NPC waveguide. The white arrows indicate targeted direction of confined phonon energy transport.

Future work will extend the current methodology to larger NPCs, as this would be advantageous for the thermoelectrics application and also more amenable to mass fabrication. As the value of A increases, the Umklapp scattering mechanism will become increasingly important (up to a length scale in the order of the mean free path). In such a regime a combination of boundary and Umklapp scattering will vigorously contribute to reducing the thermal conductivity, and the latter will compete in its effect with the reduction caused by the coherent transport mechanism. The nature of "coherent-incoherent" competition will be affected by the dispersive properties of the NPC and the ambient temperature. Once this mixed-scattering regime for NPCs is elucidated, it will be possible to fruitfully apply current concepts

in macroscale PnCs towards thermal transport. For example, one can create a NPC waveguide as illustrated in Figure 3.12 in order to confine and steer the path of heat flow in a favorable manner in devices. This concept would represent an analogy to the macroscale PnC waveguide which is used to channel acoustic or elastic waves [8,50-52]. Other similar adoptions may also be done in the broader context of the emerging field of phononics.

3.5 Acknowledgements

The authors would like to thank Dr. Eduardo A. Misawa and the National Science Foundation for their support for this research under Grant No. CMMI 0927322. In addition the authors acknowledge the Teragrid organization - also sponsored by the National Science Foundation - for allocating computation time at the Texas Advanced Computing Center (TACC) under project #MSS110021. Finally the authors would like to thank their colleagues Alan J. H. McGaughey of Carnegie Mellon University and Ihab El-Kady, Patrick E. Hopkins and Charles M. Reinke of the Sandia National Laboratories in Albuquerque, New Mexico for numerous fruitful discussions on this work.

3.6 References

[1] Balandin A. A. and Wang K. L., Significant Decrease of the Lattice Thermal Conductivity Due to Phonon Confinement in a Free-Standing Semiconductor Quantum Well, *Phys. Rev. B*, **58**, 1544 (1998).

[2] Balandin A., Thermal Properties of Semiconductor Low-Dimensional Structures, *Phys. Low-Dimens. Str.*, **1–2,** 1 (2000).

[3] Chen G., Heat Conduction in nanostructures, *Int. Jour. Therm. Sci.*, **39**, 471 (2000).

[4] Chen G., Particularities of Heat Conduction in Nanostructures, *J. Nanoparticle Research*, **2**, 199 (2000).

[5] Li D., Wu Y., Kim P., Shi L., Yang P. and Majumdar A., Thermal Conductivity of Individual Silicon Nanowires, *Appl. Phys. Lett.*, **83**, 14 (2003).

[6] Chen G., Narayanaswamy A. and Dames C., Engineering Nanoscale Phonon and Photon Transport for Direct Energy Conversion, *Superlattice. Microst.*, **35**, 161 (2004).

[7] Balandin A. A., Nanophononics: Phonon Engineering in Nanostructures and Nanodevices, *J. Nanosci. Nanotechnol.*, **5**, 1015 (2005).

[8] Sigalas M. M., Defect States of Acoustic Waves in a Two-Dimensional Lattice of Solid Cylinders, *J. Appl. Phys.*, **84**, 3026 (1998).

[9] Yang S., Page J. H., Liu Z., Cowan M. L., Chan C. T. and Sheng P., Focusing of Sound in a 3D Phononic Crystal, *Phys. Rev. Lett.*, **93**, 24301 (2004).

[10] Hussein M. I., Hulbert G. M. and Scott R. A., Dispersive Elastodynamics of 1D Banded Materials and Structures: Design, *J. Sound Vib.*, **307**, 865 (2007).

[11] Christensen J., Fernandez-Dominguez A. I., de Leon-Perez F., Martin-Moreno L. and Garcia-Vidal F. J., Collimation of Sound Assisted by Acoustic Surface Waves, *Nat. Phys.*, **3**, 851 (2007).

[12] El-Kady I., Olsson III R. H. and Fleming J. G., Phononic Band-Gap Crystals for Radio Frequency Communications, *Appl. Phys. Lett.*, **92**, 233504 (2008).

[13] Mohammadi S., Eftekhar A. A., Hunt W. D. and Adibi A., High-Q Micromechanical Resonators in a Two-Dimensional Phononic Crystal Slab, *Appl. Phys. Lett.*, **94**, 051906 (2009).

[14] Torrent D. and Sánchez-Dehesa J., Acoustic Cloaking in two Dimensions: A Feasible Approach, *New J. Phys.*, **10**, 063015 (2008).

[15] Li X. F., Ni X., Feng L. A., Lu M. H., He C. and Chen Y. F., Tunable Unidirectional Sound Propagation through a Sonic-Crystal-Based Acoustic Diode, *Phys. Rev. Lett.*, **106**, 084301 (2011).

[16] Eichenfield M., Chan J., Camacho R. M., Vahala K. J. and Painter O., Optomechanical Crystals, *Nature*, **462**, 78 (2009).

[17] Cleland N., Schmidt D. R. and Yung C. S., Thermal Conductance of Nanostructured Phononic Crystals, *Phys. Rev. B*, **64**, 172301 (2001).

[18] Khitun A., Balandin A., Liu J. L. and Wang K. L., The effect of the long-range order in a quantum dot array on the in-plane lattice thermal conductivity, *Superlattice Microst.*, **30**, 1 (2001).

[19] Balandin A. A., Lazarenkova O. L. and Boechat R. T., Thermoelectric Phonon Stop Band Materials, *Proceedings of XXII International Conference on Thermoelectrics (ICT'22), IEEE* **03TH8726**, 399, La Grand-Motte, France, (2003).

[20] Gorishnyy T., Ullal C. K., Maldovan M., Fytas G. and Thomas E. L., Hypersonic Phononic Crystals, *Phys. Rev. Lett.*, **94**, 115501 (2005).

[21] McGaughey A. J. H., Hussein M. I., Landry E. S., Kaviany M. and Hulbert G. M., Phonon Band Structure and Thermal Transport Correlation in a Layered Diatomic Crystal, *Phys. Rev. B*, **74**, 104304 (2006).

[22] Laundry E. S., Hussein M. I. and McGaughey A. J., Complex Superlattice Unit Cell Designs for Reduced Thermal Conductivity, *Phys. Rev. B*, **77**, 184302 (2008).

[23] Gillet J. N., Chalopin Y. and Volz S., Atomic-Scale Three-Dimensional Phononic Crystals With a Very Low Thermal Conductivity to Design Crystalline Thermoelectric Devices, *J. of Heat Trans. ASME*, **131**, 043206 (2009).

[24] Tang J., Wang H-T., Lee D. H., Fardy M., Huo Z., Russell T. P. and Yang P., Holey Silicon as an Efficient Thermoelectric Material, *Nano Lett.*, **10**, 4279 (2010).

[25] Yu J., Mitrovic S., Tham D., Varghese J. and Heath J., Reduction of Thermal Conductivity in Phononic Nanomesh Structures, *Nat. Nanotechnol.*, **5**, 718 (2010).

[26] Hopkins P. E., Reinke C. M., Su M. F., Olsson III R. H., Shaner E. A., Leseman Z. C., Serrano J. R., Phinney L. M. and El-Kady I., Reduction in the Thermal Conductivity of Single Crystalline Silicon by Phononic Crystal Patterning, *Nano Lett.*, **11**, 107 (2011).

[27] Robillard J. F., Muralidharan K., Bucay J., Deymier P. A., Beck W. and Barker D., Phononic Metamaterials for Thermal Management: An Atomistic Computational Study, *Chinese J. Phys.*, **49**, 448 (2011).

[28] He Y. P., Donadio D., Lee J. H., Grossman , J. C. and Galli G., Thermal Transport in Nanoporous Silicon: Interplay Between Disorder at Mesocopic and Atomic Scales, *ACS Nano*, **5**, 1839 (2011).

[29] Chen G., Dresselhaus M. S., Dresselhaus G., Fleurial J. P. and Caillat T., Recent Developments in Thermoelectric Materials, *Int. Mater. Rev.*, **48**, 45 (2003).

[30] Minnich A. J., Dresselhaus M. S, Ren Z. F. and Chen G., Bulk Nanostructured Thermoelectric Materials: Current Research and Future Prospects, *Energ. Environ. Sci.*, **2**, 466 (2009).

[31] Callaway J., Model for lattice Thermal Conductivity at Low Temperatures, *Phys Rev.*, **113**, 1046 (1959).

[32] Holland M. G., Analysis of Lattice Thermal Conductivity, *Phys. Rev.*, **132**, 2461 (1963).

[33] Srivastava G. P., The Physics of Phonons, (*Adam Hilger*, Bristol, 1990).

[34] McGaughey A. J. H. and Kaviany M., Quantitative Validation of the Boltzmann Transport Equation Phonon Thermal Conductivity Model under the Single-Mode Relaxation Time Approximation, *Phys. Rev. B*, **69**, 094303 (2004).

[35] General Utility Lattice Program, https://www.ivec.org/gulp.

[36] Maradudin, A. A., Montroll, E.W. and Weiss, G. H., Theory of Lattice Dynamics in the Harmonic Approximation, (Academic Press, New York, New York, 1963).

[37] Dove M. T., Introduction to Lattice Dynamics, (*Cambridge University Press,* Cambridge 1993).

[38] Tersoff J., New Empirical Approach for the Structure and Energy of Covalent Systems, *Phys. Rev. B*, **37**, 6991 (1988).

[39] Tersoff J., Empirical Interatomic Potential for Silicon with Improved Elastic Properties, *Phys. Rev. B*, **38**, 9902 (1988).

[40] Shanno D. F., Conditioning of Quasi-Newton Methods for Function Minimization, *Math. Comput.*, **24**, 647 (1970).

[41] Dolling G., Inelastic Scattering of Neutrons in Solids and Liquids, edited by S. Ekland, Vol. **II**, 37 (IAEA, Vienna, 1963).

[42] Mingo N., Calculation of Si Nanowire Thermal Conductivity using Complete Phonon Dispersion Relations, *Phys. Rev. B*, **68**, 113308 (2003).

[43] Ho C. Y., Powell R.W. and Liley P.E., Thermal Conductivity of the Elements *J. Phys. Chem. Ref. Data*, **1**, 279 (1972).

[44] Incropera F. P. and DeWitt D. P., Fundamentals of Heat and Mass Transfer, (*Wiley*, Hoboken, New Jersey, 2002).

[45] Bux S. K., Nanostructured Bulk Silicon as an Effective Thermoelectric Material, *Adv. Funct. Mater.*, **19**, 2445 (2009).

[46] Hepplestone S. P. and Srivastava G. P., Lattice Dynamics of Silicon Nanostructures, *Nanotechnology*, **17**, 3288 (2006).

[47] Sigalas M. and Economou E. N., Band Structure of Elastic Waves in Two Dimensional Systems, *Solid State Commun.*, **86**, 141 (1993).

[48] Kushwaha M. S., Halevi P., Dobrzynski L. and Djafari-Rouhani B., Acoustic Band Structure of Periodic Elastic Composites, *Phys. Rev. Lett.*, **71**, 2022, (1993).

[49] Sigalas M. M. and García N., Theoretical Study of Three Dimensional Elastic Band Gaps with the Finite-Difference Time-Domain Method, *J. Appl. Phys.*, **87**, 3122 (2000).

[50] Torres M., Montero de Espinosa F. R., García-Pablos D. and García N., Sonic Band Gaps in Finite Element Media: Surface States and Localization Phenomena in Linear Point Defects, *Phys. Rev. Lett.*, **82**, 3054 (1999).

[51] Khelif A., Djafari-Rouhani B., Vasseur J. O., Deymier P. A., Lambin Ph. and Dobrzynski L., Transmissivity Through Straight and Stublike Waveguides in a Two-Dimensional Phononic Crystal, *Phys. Rev. B*, **65**, 174308 (2002).

[52] Khelif A., Choujaa A., Benchabane S., Djafari-Rouhani B. and Laude V., Guiding and Bending of Acoustic Waves in Highly Confied Phononic Crystal Waveguides, *Appl. Phys. Lett.*, **84**, 4400 (2004).

4 THERMAL CONDUCTIVITY OF SILICON THIN-FILMS BASED ON FULL DISPERSION CALCULATIONS

Journal Version:
Under Preparation;

Preliminary Version:
Davis, B.L., Su, M.F, El-Kady, I. and Hussein, M.I., "Silicon thin-film lattice dynamics and thermal transport properties," *Proceedings of the ASME 2012 International Mechanical Engineering Congress & Exposition*, IMECE2012-89902, [CD ROM: pp. 1-6], Houston, Texas, 9-15 November 2012.

4.0 Abstract

Thin-films composed of dielectric materials are attracting growing interest in the solid state physics and nanoscale heat transfer communities. This is primarily due to their unique thermal and electronic properties and their extensive use as components in optoelectronic, and potentially in thermoelectric devices. In this paper, an elaborate study is presented on silicon thin-films ranging from a few nanometers in thickness to very thick bulk-like thicknesses. Full lattice dynamics calculations are performed incorporating the entire film cross section and the relaxation of the free surfaces. The phonon properties emerging from these calculations are then incorporated into Callaway-Holland models to predict the thermal conductivity and other phonon transport properties. A rigorous curve fitting process to a limited set of available experimental data is carried out to obtain the scattering lifetimes. Our results demonstrate the importance of proper consideration of the full thin-film dispersion description and provide insights into the relationship between thermal conductivity, film thickness and temperature.

4.1 Introduction

The study of heat transfer in nanoscale materials is a rapidly growing area of interest [1-6]. The concept of phonon engineering, or the manipulation of phonon wave propagation, provides promising opportunities to design materials with unique thermal transport properties. Phononic crystals (PCs) or periodic composite materials use their geometric patterning as a mechanism to scatter waves among the

intervallic physical boundaries. Numerous applications for PCs have been studied at the macroscale such as waveguiding and focusing of elastic and acoustic waves, vibration minimization, sound collimation, frequency sensing, acoustic cloaking, acoustic rectification and opto-mechanical waves coupled with photonic devices. The application of phononic crystals at the nanoscale, i.e., nanoscale phononic crystals (NPCs), is emerging as a promising approach towards the development of materials with superior thermal transport properties [7-15]. With recent progress in nanoscale fabrication techniques as well as improved modeling and computational capacity, the capability to engineer these nano-structured materials is being realized. It is feasible that the reduction in thermal conductivity due to scattering from NPCs may not have a significant impact on the scattering of electrons (due to wavelengths of different magnitudes) leading to a favorable outcome for thermoelectric materials [16-18].

In general, studies concerned with thermal transport properties of PCs need to adequately address the treatment of (1) the phonon dispersion and (2) the nonlinear scattering which involves phonon interactions with other phonons, geometrical boundaries and material impurities. Often the bulk properties of a material are utilized as an approximation for the dispersive and/or scattering properties when modeling nanoscale devices [13-15,19]. In these studies it is assumed that the minimum feature size is inherently larger than the dominant wavelengths. However as fabrication techniques allow for smaller devices, the minimum feature size encroaches on the length of the propagating waves making the bulk dispersive and scattering approximations ambiguous.

While NPCs can be realized in 3D, i.e., by introducing a 3D array of inclusions or holes into a bulk medium (as done in Chapter 3), it is more practical to have it realized in 2D, i.e., by patterning a thin-film or a slab [13-15]. Resorting to a 2D framework is also necessary for the realization of the pillared structure concept presented in Chapter 5. However, before we investigate a 2D PNC or a 2D NPM, it is essential to fully develop the modeling and analysis tools for a uniform, unpatterned thin-film. This paper focuses on predicting the full dispersion behavior and thermal conductivity of standard silicon thin-films.

The examine of a thin-film is rather tractable due to its geometrical simplicity and known minimum feature size which, for uniform and homogeneous materials, is defined only by the film's finite thickness. In addition, the computational capability to obtain the full dispersion of relatively thick films and the availability of empirical thermal conductivity measurements enable a complete end-to-end study. To determine the thermal conductivity of dielectric materials, analytical models such as the Callaway-Holland formulation [20,21] can be employed. In this calculation, the dispersion characteristics determine the phonon modal contribution to thermal transport. This formulation requires the use of nonlinear wave scattering approximations which in in this work we obtain by rigorous multi-level curve fitting of empirical data.

To determine the dispersion curves of a thin-film, lattice dynamics (LD) [22,23] is employed on a narrow finite strip of the thin-film, which when extended periodically along the in-plane *x*- and *y*-directions forms a 2D thin-film. This is an improvement over the two-atom primitive cell bulk dispersion (a 3D representation of bulk media–without any consideration of the finite surfaces–commonly used in the Callaway-Holland and other similar formulations) since it incorporates the out-of-plane finiteness of the material and the corresponding restrictions of the boundaries. Furthermore, fitting nonlinear scattering parameters onto temperature-dependent experimental measurements of thin-films enables thickness dependent phonon-phonon nonlinear scattering parameters to be incorporated. This is an improvement over a commonly used approach (which we will refer to as the conventional approach) that uses constant parameters that are fitted only to bulk dispersion data. In these past studies, some fitting models are utilized that incorporate surface roughness and specular/diffuse reflections to accommodate interactions at the boundaries [19,32]; however these studies were not based on full dispersion calculations. Other thin-film studies have taken the approach to incorporate a full dispersion model (although with some simplifications in the interatomic potential) [34,35] in the prediction of thermal conductivity, however these depended on bulk scattering properties of the material.

With our modeling methodology, we can investigate the limits for when the use of bulk dispersion in the prediction of the thermal conductivity of thin-films is appropriate. In addition, this work identifies an implied size effect in which the influence of finite boundaries, and thus the thermal conductivity, plays a significant role on the dispersion and nonlinear phonon-phonon scattering; shedding light into the length scales in which the minimum feature size becomes relevant within NPCs or reduced dimension nanostructures in general. A comprehensive understanding of the dispersion and nonlinear scattering properties of thin-films will enable further studies of NPCs when in-plane periodicity is introduced, as well as the NPMs studied in Chapter 5.

In this paper, Section 4.2 provides a thorough overview of the crystalline structure of silicon thin-films and its dispersion properties. The difference in dispersion between bulk and thin-film silicon are identified and compared as a function of thickness. Section 4.3 provides an overview of the Callaway-Holland formulation to predict the thermal conductivity of bulk silicon (i.e., a 3D material with indefinite extensions in all directions). A brief derivation is then presented which modifies the existing formulation to accommodate the finite nature of thin-films (i.e., a 2D material with a finite out-of-plane extension). In Section 4.4, the thermal conductivity of various thin-films is computed for both the bulk-based and true thin-film dispersion models. The nonlinear scattering parameters for both methods are fitted to empirical data for various thicknesses and temperatures. Upon comparison, it is shown that improvements in the prediction of the thermal conductivity can be realized when incorporating the full dispersion and thickness-dependent scattering fitting parameters to empirical data. In Section 4.5, conclusions are provided followed by a brief outlook and implications of this work on thin-film-based nanoscale phononic materials (NPMs) in Chapter **Error! Reference source not found.**.

4.2 Phonon Dispersion in Thin-films

This study focuses on the wave propagation in silicon based thin-films with a thickness less than one micron. As a result, when modeling wave propagation at this scale the discrete atomic structure needs to be considered. Crystalline silicon contains a two-atom primitive basis that is extended along a face-centered-cubic (FCC) lattice structure. In Figure 4.1 (left), the two-atom primitive basis and corresponding Brillouin Zone can be seen (with a lattice constant a = 0.54nm). The lattice vectors (red arrows) are non-orthogonal in nature which results in a Brillouin Zone that is a truncated octahedron. The reciprocal lattice vectors (blue lines) indicate the base coordinate system within the near-spherical Brillouin Zone. The ΓX direction, which is the direction of propagation considered in this study, is identified (dotted orange line). When forming a supercell (in this case a narrow unit strip to represent the dynamics of a thin-film, it is convenient to extend the crystalline structure along an orthogonal basis. As a result a cube is drawn around the primitive cell shown in light blue in Figure 4.1 (left) and filled forming an eight-atom conventional cell with a simple cubic (SC) lattice type in Figure 4.1 (center). Here the lattice (red arrows) and reciprocal lattice (blue lines) vectors are now orthogonal forming a cubic Brillouin Zone. Although this is not the most basic representation of the crystalline structure, the dispersion and subsequent phonon transport predictions are still representative of the material behavior [33]. When investigating thin-films, the periodicity of the out-of-plane direction (z) is truncated forming a two-dimensional material. The crystalline structure for thin-films of various thicknesses is established by stacking M conventional unit cells in the out-of-plane direction forming a finite strip of thickness A_z. The in-plane (x, y directions) lattice vectors are maintained to form a thin-film material that is infinite along these directions (Figure 4.1 right). The absence of periodicity along the out-of-plane direction creates a two-dimensional square (rather than cubic) Brillouin Zone.

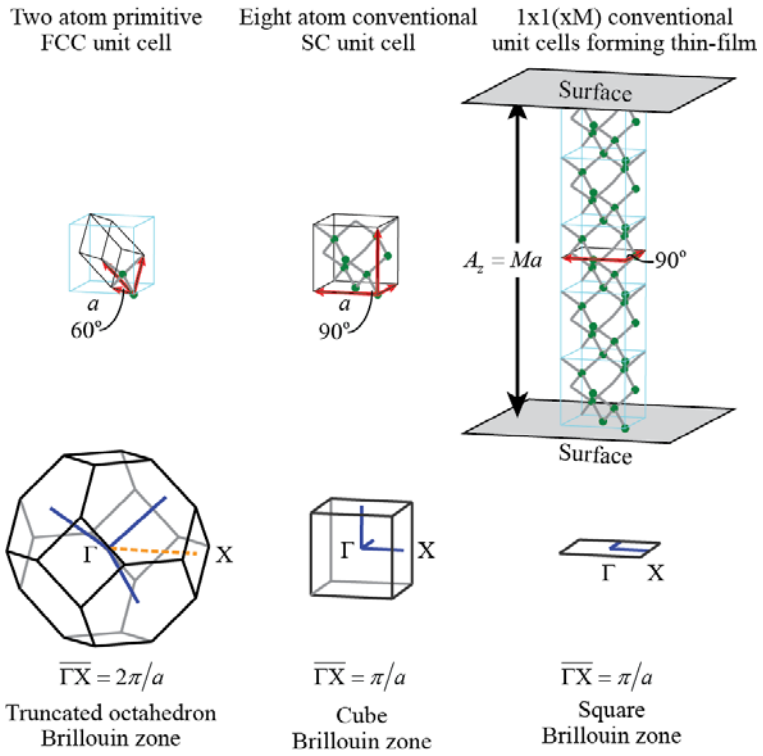

Figure 4.1: The silicon crystalline structure for: primitive bulk (left), conventional bulk (center) and conventional thin-film (right). The crystal lattice vectors are shown with red arrows for lattice constant *a*. The encompassing Brillouin Zone shape for each type is outlined with the Γ and X high symmetry points labeled and the reciprocal lattice vectors are shown in blue. For the case of the thin-film, the Brillouin Zone is two-dimensional in shape and the finite thickness is defined by A_z, which is determined by the number of *M* stacked conventional cells; here *M*=5.

The phonon dispersion of silicon is formulated utilizing the General Utility Lattice Program [24]. For all cases reported in this paper, the three-body Tersoff potential is used for the Si-Si bonds with only the first nearest neighboring interactions considered [25,26]. Prior to calculating the dispersion, the energy is minimized at constant pressure to relax the structure and ensure stability. This is especially relevant near the boundary edges at the film top and bottom surfaces. The Broyden-Fletcher-Goldfarb-Shanno (BFGS) optimization method [27] is used to accommodate these free boundaries.

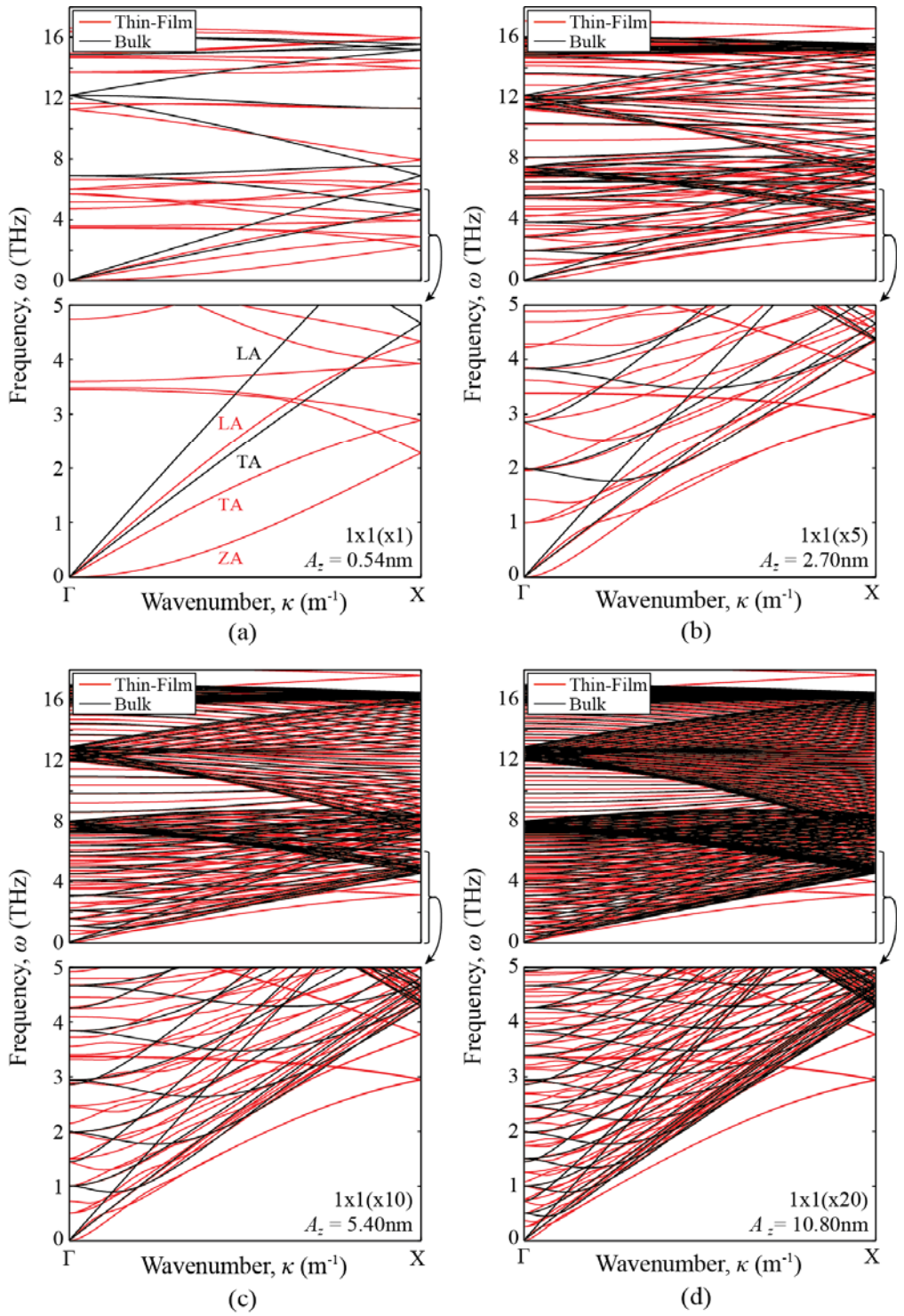

Figure 4.2: Silicon phonon dispersion for both thin-film (red) and bulk (bulk) for 1×1(×*M*) supercells. Note the differences in degeneracy and the curvature of the acoustic branches as the out-of-plane dimension (*M*) is increased.

As the thin-film thickness increases, more atoms must be considered to form a unit cell of the lattice resulting in an increased number of dispersion branches. Figure 4.2 illustrates the complexity of the dispersion as the thickness increases ranging from the thinnest allowable of A_z = 0.54nm in Figure 4.2 (one conventional cell or M = 1; Figure 4.2a) up to A_z =10.80nm (M = 20; Figure 4.2d). When comparing dispersion of 3D extended bulk (i.e., bulk supercells with the same geometrical arrangement) with 2D thin-films, differences occur due to the elimination of out-of-plane periodicity and the wave interaction with finite boundaries. In this illustration, we directly compare the dispersion between extended bulk (black) and thin-films (red) for a 1×1(×M) crystalline supercell. We note that for all thicknesses, the general dispersion trend is maintained and most of the branches are clumped in a similar manner between both the bulk and thin-film cases. We also note that the folding that appears is due to the conventional unit cell being larger than a primitive cell (which is acceptable for the upcoming thermal conductivity calculations since these are just alternative representations of the same material). For very thick films, the dispersion resembles that of the extended bulk with the noted key exceptions: (1) broken degeneracy and a general reduction in frequency among most branches, (2) the slope of two acoustic modes of the thin-film lies outside from the primary cluster of the dispersion branches, (3) the magnitude of the two highest optical branches extends above of the cluster of dispersion branches creating a new maximum frequency, which is a result of the surface relaxation, and finally (4) the out-of-plane acoustic branch nonlinearity near the Γ point.

As previously mentioned, there are significant differences in the acoustic branches of bulk and thin-film dispersion. This is especially relevant near the Γ point, i.e., the long wave lengths which play an important role in thermal transport. This can be first illustrated in Figure 4.2a where we identify the longitudinal acoustic (LA) and transverse acoustic (TA) modes for bulk silicon. Here the LA mode is along the x-direction (ΓX) with the degenerate TA modes propagating with motion in the y- and z-directions. This degeneracy occurs because of the 3D nature of the geometry. Upon comparison with the

thin-film dispersion, we notice that the degeneracy of the TA modes no longer exits and we redefine the *z*-direction mode as ZA or out-of-plane acoustic mode. This mode exhibits a nearly flat slope near the Γ point indicating a zero group velocity, which is a characteristic of long-wave plate-like motion. As the film thickness is increased (from Figure 4.2b to 2c to 2d), unique traits occur for each acoustic branch. For the ZA mode, the flat slope near the Γ point becomes less pronounced and eventually converges with the LA branch. The LA branch on the other hand becomes highly nonlinear over a specific thickness range before converging with the properties of the ZA branch. Finally, the TA branch remains linear with its slope converging to the TA value of the bulk dispersion.

To further illustrate this phenomenon, Figure 4.3a displays the trends of the three acoustic branches across various thicknesses when $q \leq 0.003$ (where the normalized Brillouin Zone boundary is defined by $q_{max} = 0.5$). We find that as the thickness increases, the second branch converges or 'locks' onto the bulk acoustic branch (dotted lines), inferring that this in-plane transverse mode is less influenced by the film boundaries at larger thicknesses and at a prescribed thickness threshold has achieved some traits of bulk-like dispersion. Figure 4.3b more clearly illustrates the convergence trends across various thicknesses at a

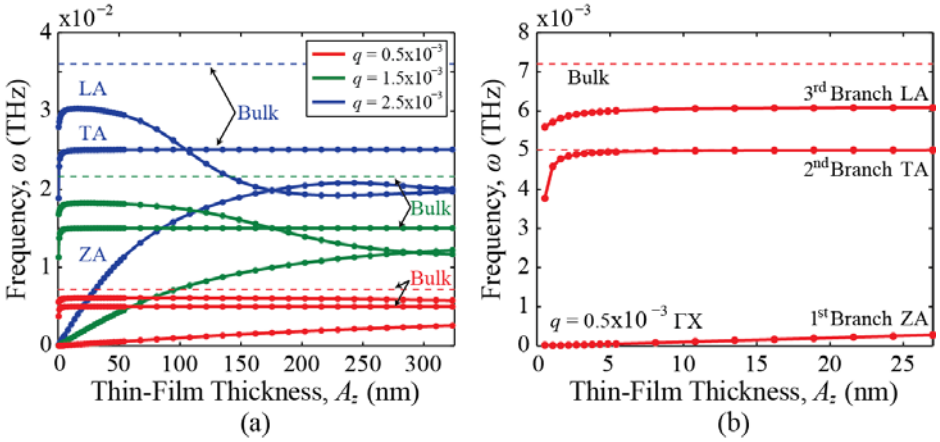

Figure 4.3: Acoustic mode convergence for silicon thin-films with increasing thickness at very low wavenumbers (left). Note the 'locking' with bulk values for the second acoustic branch for increasing film thicknesses; an expanded view for small thicknesses is shown (right). Here LA, TA and ZA are the acoustic longitudinal, transverse and out-of-plane waves, respectively.

small wavenumber value of $q = 0.5\text{x}10^{-3}$. We see that the ZA branch grows steadily at low thicknesses, and the LA branch at small thicknesses converges to a constant value however does not lock with that of the bulk medium. For larger thicknesses, the first and third acoustic branches converge, at short wavelengths, to form a degenerate branch.

4.3 Thermal Conductivity, 2D and 3D Materials

Predicting the thermal conductivity of bulk silicon dispersion (based on a primitive cell) utilizing the Callaway-Holland model is well documented in literature [20,21]. The formulation consists of three components: the specific heat C_{ph}, the group velocity v_g and time scattering parameters τ; each of which are related to the dispersion where κ and λ are the phonon wave vector and polarization branch, respectively (eq. 4.1). The thermal conductivity is computed by integrating these phonon properties across the volume of the Brillouin Zone along all possible wave motion directions. For the case of bulk silicon, the two atom face-centered cubic structure has a near-spherical Brillouin Zone with the Γ-X path ranging from 0 to $2\pi/a$. To incorporate the bulk geometry into the calculation, a prefactor is included which contains three components: the volume of the spherical Brillouin Zone ($4\pi\int \kappa^2 d\kappa$), the average value of the specified direction over a spherical volume (1/3), and the normalized volume of the Brillouin Zone in 3D space for a primitive cell $(2\pi/a)^3$. This formulation is consistent with recent studies utilizing bulk silicon [12,15].

$$k = \frac{4\pi/3}{(2\pi)^3}\sum_{\lambda}\int_0^{2\pi/a} C_{ph}(\kappa,\lambda)v_g^2(\kappa,\lambda)\tau(\kappa,\lambda)\kappa^2 d\kappa \tag{4.1}$$

Upon applying the Callaway-Holland model for silicon slabs, a few modifications are implemented to reflect the 2D nature of the crystalline structure (eq. 4.2). The length of the ΓX path is reduced by a factor of 2 to accommodate the simple cubic lattice structure of the conventional cell. In addition, the three components that define the multiplying prefactor of the integral now derive from a 2D system: the surface

of the Brillouin Zone (which is now the area of a circle, $2\pi\int\kappa d\kappa$), the average value of a specified direction over a circular area (1/2), and the normalized surface of the Brillouin Zone in 2D space for a conventional cell $(\pi/a)^2$. In addition, A_z appears in the prefactor to incorporate the thickness of the thin-film. This formulation is consistent with previous studies incorporating 2D thin-film dispersion [34,35].

$$k = \frac{2\pi/2}{A_z \pi^2} \sum_{\lambda} \int_0^{\pi/a} C_{ph}(\kappa,\lambda) v_g^2(\kappa,\lambda) \tau(\kappa,\lambda) \kappa \, d\kappa \tag{4.2}$$

The heat capacity C_{ph} (eq. 4.3) measures the energy of each phonon mode and incorporates the Boltzmann-Einstein distribution to account for quantum effects at low wavenumbers. Here ω is the phonon frequency, k_B is the Boltzmann constant, $\hbar$ is the reduced Plank's constant, and T is the temperature.

$$C_{ph}(\kappa,\lambda) = k_B \left(\frac{\hbar\omega(\kappa,\lambda)}{k_B T} \right)^2 \frac{\exp(\hbar\omega(\kappa,\lambda)/k_B T)}{\left[\exp(\hbar\omega(\kappa,\lambda)/k_B T) - 1\right]^2} \tag{4.3}$$

The phonon group velocity is measured by taking the derivative of the phonon frequency with respect to the wave number (eq. 4.4). This can intuitively be determined by taking the slope of the dispersion curves.

$$v_g(\kappa,\lambda) = \frac{\partial\omega(\kappa,\lambda)}{\partial\kappa} \tag{4.4}$$

Finally the phonon scattering time can be broken into three major components: Umklapp τ_U, impurity τ_I and minimum feature size τ_B. The inverse of these variables are summed via Matthiessen's rule which enables the stand-out variables to be dominant over the others (eq. 4.5).

$$\tau(\kappa,\lambda) = \left(\frac{1}{\tau_U(\kappa,\lambda)} + \frac{1}{\tau_I(\kappa,\lambda)} + \frac{1}{\tau_B(\kappa,\lambda)} \right)^{-1}$$
$$= \left(A_u T \omega^2(\kappa,\lambda) \exp(-B_u / T) + D\omega^4(\kappa,\lambda) + \left| v_g \right| / L \right)^{-1} \quad (4.5)$$

The Umklapp scattering term represents the phonon-phonon interactions and is therefore temperature and frequency dependent. This term has two fitted parameters A_u and B_u which in this work we obtain using empirical data. The impurity scattering is frequency dependent and contains the parameter D, which is well established in the literature [28]. The boundary scattering is dependent on the absolute value of the group velocity of each phonon and the minimum feature length L. We note that this form of boundary scattering is an improvement over the conventional approach [12,15,20,21] which approximates all phonon velocities to be equivalent to the average velocity or the speed of sound in the material. For thin-films, the minimum feature length is set to be A_z. Boundary scattering is a surface process while impurity and Umklapp are volumetric phenomena.

4.4 Thermal Conductivity of Silicon Thin-Films

We now turn to the main focus of this work where the thermal conductivity of silicon thin-films is determined by three formulations: 1) the *conventional model* which incorporates bulk dispersion and bulk (i.e., constant) scattering parameters, 2) an *enhanced model* which utilizes bulk dispersion and thin-film (i.e., thickness adjusted) scattering parameters, and 3) the *proposed model* which incorporates both thin-film dispersion and thin-film scattering parameters.

In the *conventional model*, the fitting parameters of A_u and B are obtained using empirical thermal conductivity data for bulk silicon across a wide temperature range. The thin-film thickness in this model appears only in the boundary scattering term in Eq. (4.5); otherwise the calculations are performed using Eq. (4.1) and use of bulk dispersion. This approach is consistent with previous work [12]. The *enhanced model* contains a better approximation for the nonlinear Umklapp scattering parameters by utilizing

empirical thermal conductivity measurements of actual thin-films at various temperatures. This model also utilizes bulk dispersion and the Callaway-Holland approach outlined in Eq. (4.1). The available data limits the fitting to a series of thicknesses of A_z = 20, 30, 50, 100, 420 and 3000nm [29-31]. The Umklapp parameters A_u and B_u are fitted for each thin-film thickness and their thermal conductivity is plotted vs. temperature in Figure 4.4. Here the available empirical measurements are plotted with square markers.

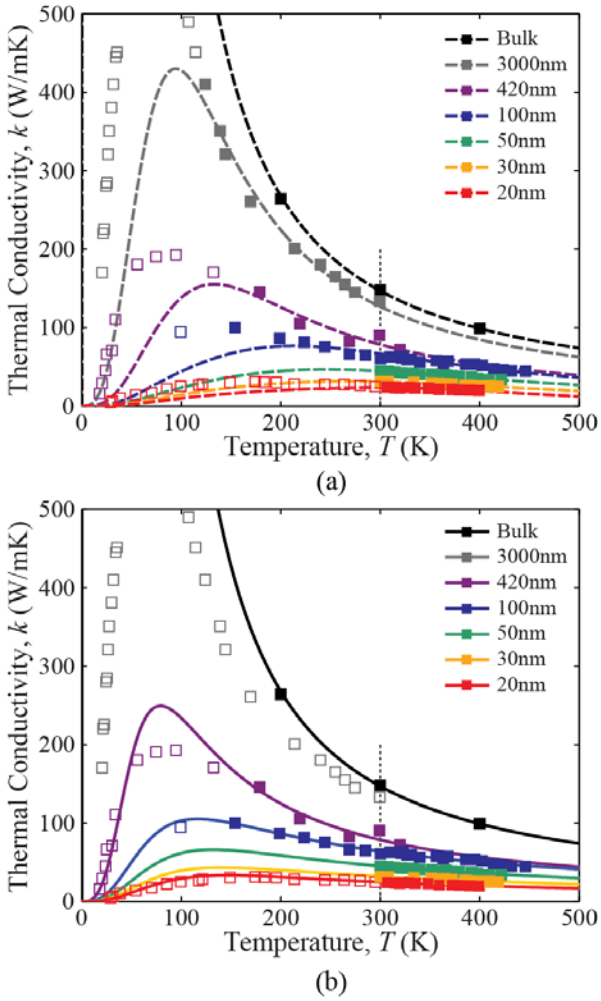

Figure 4.4: Thermal conductivity of thin-films across various thicknesses and temperatures with square markers indicating empirical data. Dashed lines (top) are the Callaway-Holland predictions using the bulk dispersion approximation while the solid lines (bottom) utilize the full dispersion and incorporates the Callaway-Holland model with a finite thickness. The Umklapp parameters, A and B, were fitted for each thickness across a temperature range centered at T = 300K utilizing the empirical data which are drawn as filled markers.

Given that the aim of this study is to fit around a constant temperature of T = 300K, only the filled markers in Figure 4.4a were incorporated for each film thickness when fitting the scattering parameters. This required discretion by the authors to best incorporate the available data around 300K. For example, the film thickness of A_z = 100 nm utilized empirical data between 150K and 450K to enable a consistent transition between A_z = 420 and 50 nm which had limited data below and above T = 300K respectively. The final scattering parameters as well as the temperature ranges considered for each curve fitting is given in Table 4.1.

Table 4.1: A & B parameter values selected for each thin-film thickness.

Thermal Conductivity Fitting over Temperature					
Thickness, A_z (nm)	**Temp Range, T (K)**	**Bulk A_u (s/K)**	**Bulk B_u (K)**	**Thin-film A_u (s/K)**	**Thin-film B_u (K)**
Bulk, ($A_z = \infty$)	200 – 400	2.026e-19	177	2.026e-19	177
3000	120 – 300	2.469e-19	277	n/a	n/a
420	150 – 320	3.939e-19	385	6.984e-19	170
100	150 – 450	5.776e-19	801	5.235e-19	189
50	300 – 425	8.571e-19	1001	6.602e-19	223
30	300 – 425	1.931e-18	1333	8.086e-19	194
20	300 – 400	3.248e-17	2463	1.165e-18	245

Next we turn to the *proposed model* for predicting thermal conductivity which incorporates both the full thin-film dispersion and the scattering parameters utilizing thin-film empirical measurements. This model incorporates the 2D Callaway-Holland approach outlined in Eq. (4.2). Like before, the available data limits the fitting to a series of thicknesses. Figure 4.4b shows the improvement in matching the thermal conductivity with full dispersion. The bulk and thin-film full-dispersion based scattering parameters are identified in Table 4.1. Upon comparison, we find that the *proposed model* contains a better fit with the empirical data across a wide temperature range. This outcome can be further illustrated by fitting across the full temperature range as shown in Figure 4.5. Here we select the film thickness of

A_z = 420, 100 and 20nm which have a consistent range of data across all temperatures. We note that the *proposed model* maintains a strong improvement over the *enhanced model*, especially at low temperatures. In addition, we note that including low temperature empirical data within the *enhanced model* prevents a smooth and consistent trend between the thicknesses at higher temperatures.

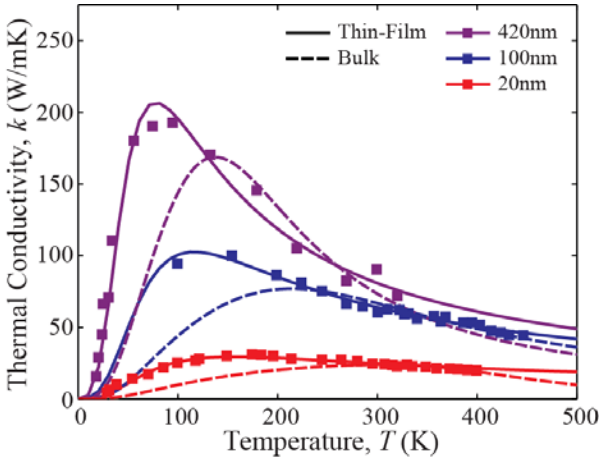

Figure 4.5: Thermal conductivity of thin-films (with a thickness of A_z = 20, 100 and 420 nm) versus temperature. Here a comparison between the bulk and thin-film based dispersion results is shown for all available empirical data (shown as solid markers).

Upon resolving the fitted parameters for each film thickness, a trend can be obtained to determine the adjusted parameters as a function of thickness. In this case we focus on film thicknesses between 20nm ≤ A_z ≤ 100nm which is selected due to an abundance of corresponding data over a consistent temperature range. The thicknesses of A_z = 420nm and 3000nm are not utilized due to a shortage in empirical data and limited computational resources respectively. The trending equations were selected on the basis of the following criteria: 1) follow the general trend across the desired film thicknesses and 2) have a slope of zero at A_z = ∞ (i.e., at large thicknesses, the thin-film becomes bulk-like and as a result the A_u and B_u parameters do not vary). Figure 4.6 shows the A_u and B_u parameters as a function of film thickness. Here

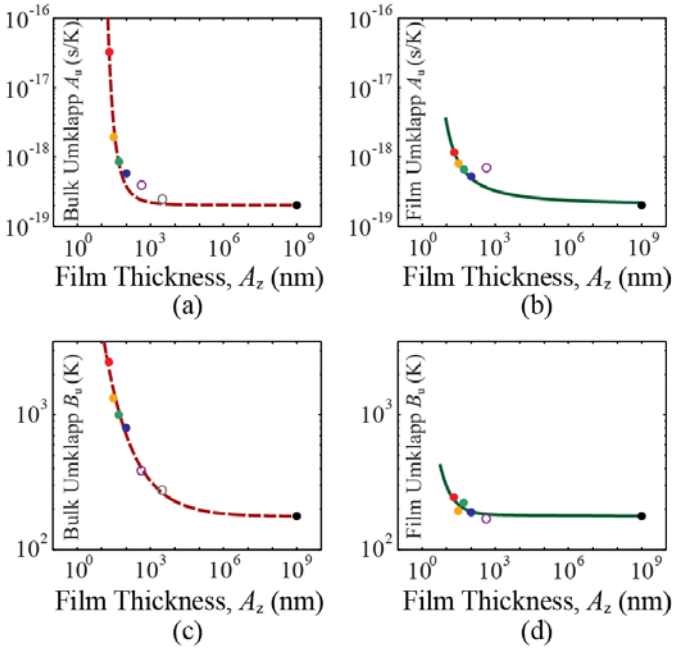

Figure 4.6: The fitted A_u and B_u values as a function of thin-film thickness. Trending equations are superimposed.

the solid markers for the 'bulk' (i.e., *enhanced model*) and 'film' (i.e., *proposed model*) identify the parameters used when fitting the trending equations and use the same color scheme as in Figure 4.4. The hollow markers are placed on the figure to illustrate the general trend and inaccuracies present due to the lack available empirical data. Although data is present for the bulk case of A_z = 3000nm, it is disregarded in order to remain consistent with thin-film formulation. The following equations

$$A_u(A_z) = mA_z^{-n} + A_{u,\infty} \tag{4.6}$$

$$B_u(A_z) = ae^{-bA_z} + ce^{-dA_z} \tag{4.7}$$

are used to fit the data in Figure 4.6 with the constants displayed in Table 4.2. Note that these equations were formulated in log-log space.

Table 4.2: Curve fit parameters forming the A_u & B_u values for all thicknesses

A_u & B_u Parameter Fitting over Thin-film Thickness at T = 300 K							
	Parameter A_u			**Parameter B_u**			
	m ***s/(nm K)***	***n*** ***(no units)***	$A_{u,\infty}$ ***(s/K)***	***a*** ***(K)***	***b*** ***(1/nm)***	***c*** ***(K)***	***d*** ***(1/nm)***
Bulk	965.3	4.811	-43.043	7.495	0.364	5.168	-7.165×10^{-5}
Thin-film	9.935	1.581	-43.043	3.974	0.911	5.205	2.076×10^{-4}

Upon establishing the proper trending equation for the thickness-adjusted scattering parameters of silicon thin-films, we can now compute the thermal conductivity of any film thickness within the specified ranges. In this case, the computations are valid between the thicknesses of 20 nm $\leq A_z \leq$ 100 nm and temperatures of 150K $\leq T \leq$ 450K. Pertaining to thickness, any result beyond this range is due to extrapolation. Figure 4.7 shows the thermal conductivity following the three approaches as a function of film thickness. The solid black line utilizes bulk dispersion and scattering parameters (*conventional model*). The figure includes measured thin-film data points which are shown as black dots. The colored lines in Figure 4.7 show the effects of incorporating thin-film dispersion and the thickness dependent A_u and B_u scattering parameters. The dotted dark red line incorporates the adjusted scattering parameters (*enhanced model*) while the solid dark green line incorporates both the adjusted parameters and the inclusion of thin-film dispersion (*proposed model*). The general trend across all thicknesses can be seen where the thermal conductivity is greatly reduced at low thicknesses due to scattering from the film boundaries (i.e., the minimum feature size). At very large thicknesses, this boundary scattering term becomes negligible and the thermal conductivity approaches the bulk characteristics. This effect is further demonstrated in Figure 4.8 where we look at the relative contributions of the different modes of the dispersion spectrum (identified by branch and wavenumber) to the thermal conductivity for the bulk (top) and thin-film (bottom) cases at various thicknesses. Here we plot dispersion with a spectral color

scheme to highlight which regions of the dispersion are most significant (three left plots) as well as a thermal conductivity cumulative plot for increasing frequency (right). Upon utilizing bulk dispersion with a boundary thickness of L = 1m, we have essentially nullified the effect of the film thickness and

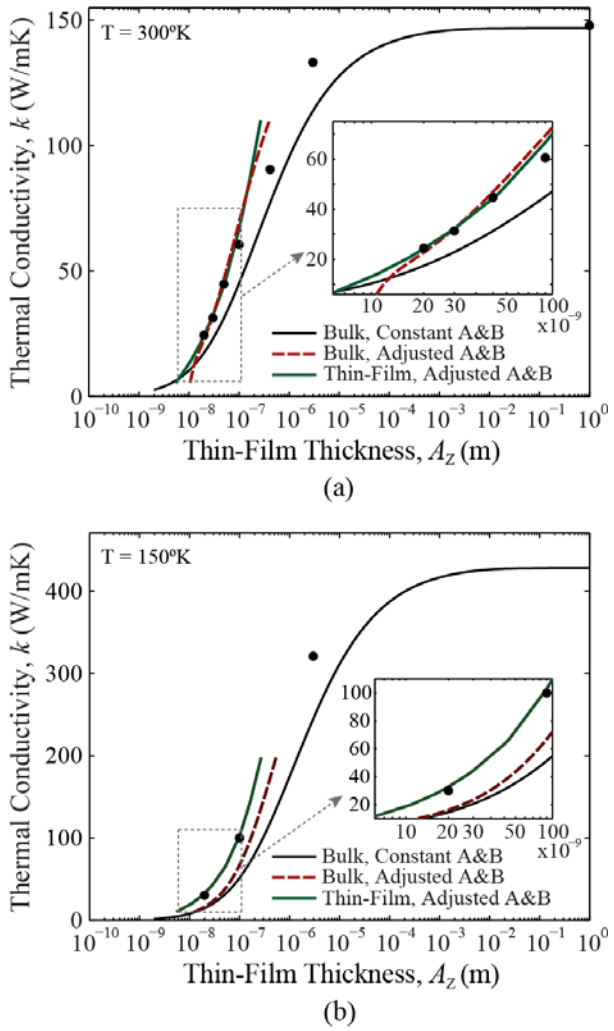

Figure 4.7: Computed thermal conductivity of silicon vs. thickness using the Callaway-Holland model at two temperatures: T=300K (top) and T=150K (bottom). Thermal conductivity predictions using bulk dispersion with constant A_u and B_u parameters (solid black), bulk dispersion and the thickness-adjusted parameters (dashed red), and full thin-film dispersion and thickness-adjusted parameters (solid green) are shown. Thin-film dispersion is shown to provide a noticeably improved correlation with empirical data (black dots) especially at small thicknesses.

thus obtain the response of 3D bulk-like material. As a result, we see that the vast majority of the phonon transport contributing to the thermal conductivity is within the acoustic branches at low wavenumbers; this is consistent with another study [36] which performed a similar investigation for carbon nanotubes. For this system, as the film thickness decreases—and the impact of boundary scattering grows—the phonons with the longer wavelengths (i.e., lower wavenumbers) are more heavily impacted than the shorter wavelengths (i.e., higher wavenumbers). This trend exists whether utilizing bulk dispersion (top) or the thin-film dispersion with proper thickness adjusted scattering parameters for three selected thicknesses (bottom).

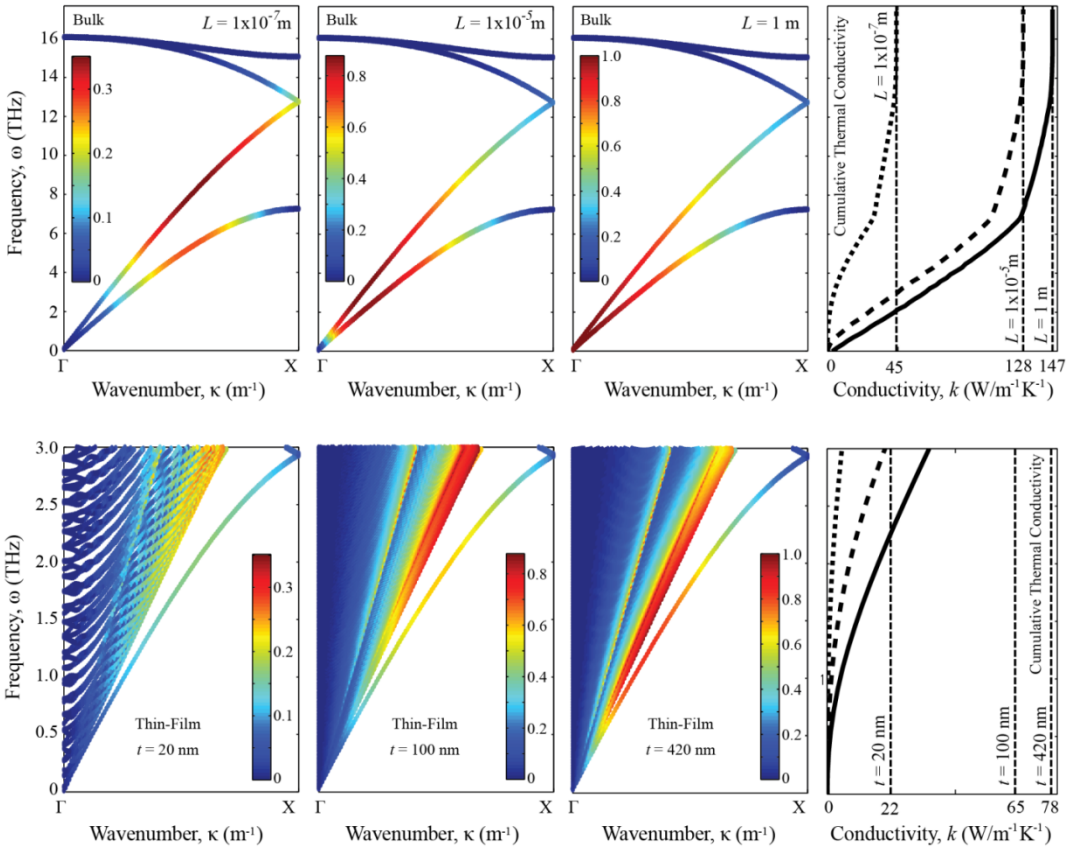

Figure 4.8: Color spectral plot representing the relative phonon contribution to the thermal conductivity for each branch and wavenumber (left three plots). The cumulative thermal conductivity is shown for these three plots as a function of frequency (right). The impact of increasing boundary scattering (due to limiting L for the bulk case in the top row, and t for the thin-film case in the bottom row) is illustrated by the shifting in color density to higher wavenumbers.

Returning to Figure 4.7, we observe that for a temperature of T = 300 K (Figure 4.7a), the proposed approach predictions are seen to be highly aligned with the empirical data and hence exhibits a significant improvement over the results of the *conventional approach*. In addition, there is a slight improvement of the *proposed model* over the *enhanced model* within the fitted thickness range (20nm ≤ A_z ≤ 100nm). Outside of this range (where extrapolation occurs, i.e., 20nm > A_z and A_z < 100nm), this improvement becomes more significant at very low thicknesses since the effect of boundaries on the dispersion plays an increased role. The inset within Figure 4.7a more closely illustrates this improvement. At lower temperatures, the role of including thin-film dispersion curves is further pronounced as shown in Figure 4.7b where T = 150K. This is explained by the fact that dispersion plays a more prominent role (compered to Umpklapp scattering) with decrease in temperatures.

The improved performance of predicting the thermal conductivity at very low thicknesses outlines the importance of incorporating both the thin-film dispersion and thickness-adjusted scattering parameters within the formulation. This suggests that below a threshold thickness, bulk dispersion is no longer valid in predicting thermal conductivity. Figure 4.7 suggests that this minimum thickness is on the order of 15-20nm. As for lower temperatures, incorporation of full dispersion appears to be important at a much broader range thickness.

4.5 Conclusions

In summary, the thermal conductivity of silicon thin-films was predicted via formulations that require the full phonon dispersion and thickness-dependent parameters for approximating the nonlinear phonon-phonon scattering effects. It was found that the conventional approach of using bulk properties to model the thermal conductivity of thin-films can be dramatically improved by incorporating the full thin-film dispersion and utilizing thin-film empirical data for the scattering parameters. This effort required the need to modify the Callaway-Holland thermal conductivity formulation to incorporate the finite

boundaries present within the thin-film as well as fitting techniques to acquire the thickness-dependent scattering parameters. It was found that the improvements of the proposed method are more significant at lower temperatures and in thin-films with a thickness lower than ~15-20nm. In these regimes, phonon dispersion plays a more significant role in determining the thermal conductivity. A comprehensive understanding of the dispersion and nonlinear scattering properties of thin-films will enable further studies of NPCs when in-plane periodicity is introduced.

4.6 Acknowledgements

BLD and MIH would like to thank Dr. Eduardo A. Misawa and the National Science Foundation for their support for this research under Grant No. CMMI 0927322. In addition, all authors are grateful to Charles Reinke and Patrick Hopkins for their insightful discussions relating to this topic as well as to Leslie Phinney for her support enabling collaboration between the CU-Boulder group and Sandia National Laboratory (SNL) under grant No. 1113289. SNL is a multi-program laboratory managed and operated by Sandia Corporation, a wholly owned subsidiary of Lockheed Martin Corporation, for the U.S. Department of Energy's National Nuclear Security Administration under contract DE-AC04-94AL85000.

4.7 References

[1] Balandin A. A. and Wang K. L., Significant Decrease of the Lattice Thermal Conductivity Due to Phonon Confinement in a Free-Standing Semiconductor Quantum Well, *Phys. Rev. B*, **58**, 1544 (1998).

[2] Balandin A., Thermal Properties of Semiconductor Low-Dimensional Structures, *Phys. Low-Dimens. Str.*, **1–2**, 1 (2000).

[3] Chen G., Heat Conduction in nanostructures, *Int. Jour. Therm. Sci.*, **39**, 471 (2000).

[4] Chen G., Particularities of Heat Conduction in Nanostructures, *J. Nanoparticle Research*, **2**, 199 (2000).

[5] Chen G., Narayanaswamy A. and Dames C., Engineering Nanoscale Phonon and Photon Transport for Direct Energy Conversion, *Superlattice. Microst.*, **35**, 161 (2004).

[6] Balandin A. A., Nanophononics: Phonon Engineering in Nanostructures and Nanodevices, *J. Nanosci. Nanotechnol.*, **5**, 1015 (2005).

[7] McGaughey A. J. H., Hussein M. I., Landry E. S., Kaviany M. and Hulbert G. M., Phonon Band Structure and Thermal Transport Correlation in a Layered Diatomic Crystal, *Phys. Rev. B*, **74**, 104304 (2006).

[8] Laundry E. S. and Hussein M. I. and McGaughey A. J., Complex Superlattice Unit Cell Designs for Reduced Thermal Conductivity, *Phys. Rev. B*, **77**, 184302 (2008).

[9] Gillet J. N., Chalopin Y. and Volz S., Atomic-Scale Three-Dimensional Phononic Crystals With a Very Low Thermal Conductivity to Design Crystalline Thermoelectric Devices, *J. of Heat Trans. ASME*, **131**, 043206 (2009).

[10] Robillard J. F., Muralidharan K., Bucay J., Deymier P. A., Beck W. and Barker D., Phononic Metamaterials for Thermal Management: an Atomistic Computational Study, *Chinese J. Phys*., **49**, 448 (2011).

[11] He Y. P., Donadio D., Lee J. H., Grossman , J. C. and Galli G., Thermal Transport in Nanoporous Silicon: Interplay Between Disorder at Mesocopic and Atomic Scales, *ACS Nano*, **5**, 1839 (2011).

[12] Davis B. L., Hussein M. I., Thermal Characterization of Nanoscale Phononic Crystals using Supercell Lattice Dynamics, *AIP Advances*, **1**, 041701 (2011).

[13] Tang J., Wang H-T., Lee D. H., Fardy M., Huo Z., Russell T. P. and Yang P., Holey Silicon as an Efficient Thermoelectric Material, *Nano Lett.*, **10**, 4279 (2010).

[14] Yu J., Mitrovic S., Tham D. and Varghese J., Heath J., Reduction of Thermal Conductivity in Phononic Nanomesh Structures, *Nat. Nanotechnol.*, **5**, 718 (2010).

[15] Hopkins P. E., Reinke C. M., Su M. F., Olsson III R. H., Shaner E. A., Leseman Z. C., Serrano J. R., Phinney L. M. and El-Kady I., Reduction in the Thermal Conductivity of Single Crystalline Silicon by Phononic Crystal Patterning, *Nano Lett.*, **11**, 107 (2011).

[16] Chen G., Dresselhaus M. S., Dresselhaus G., Fleurial J. P. and Caillat T., Recent Developments in Thermoelectric Materials, *Int. Mater. Rev.*, **48**, 45 (2003).

[17] Minnich A. J., Dresselhaus M. S, Ren Z. F. and Chen G., Bulk Nanostructured Thermoelectric Materials: Current Research and Future Prospects, *Energ. Environ. Sci.*, **2**, 466 (2009).

[18] Venkatasubramanian R., Siivola E., Colpitts T. and O'Quinn B., Thin-Film Thermoelectric Devices with High Room-Temperature Figures of Merit, *Nature*, **413**, 597 (2001).

[19] Maldovan M., Micro to Nano Scale Thermal Energy Conduction in Semiconductor Thin Films, *J. Appl. Phys.*, **110**, 034308 (2011).

[20] Callaway J., Model for lattice Thermal Conductivity at Low Temperatures, *Phys Rev.*, **113**, 1046 (1959).

[21] Holland M. G., Analysis of Lattice Thermal Conductivity, *Phys. Rev.*, **132**, 2461 (1963).

[22] Maradudin, A. A., Montroll, E.W. and Weiss, G. H., Theory of Lattice Dynamics in the Harmonic Approximation, (Academic Press, New York, New York, 1963).

[23] Dove M. T., Introduction to Lattice Dynamics, (*Cambridge University Press,* Cambridge, 1993).

[24] General Utility Lattice Program, https://www.ivec.org/gulp.

[25] Tersoff J., New Empirical Approach for the Structure and Energy of Covalent Systems, *Phys. Rev. B*, **37**, 6991 (1988).

[26] Tersoff J., Empirical Interatomic Potential for Silicon with Improved Elastic Properties, *Phys. Rev. B*, **38**, 9902 (1988).

[27] Shanno D. F., Conditioning of Quasi-Newton Methods for Function Minimization, *Math. Comput.*, **24**, 647 (1970).

[28] Mingo N., Calculation of Si Nanowire Thermal Conductivity using Complete Phonon Dispersion Relations, *Phys. Rev. B*, **68**, 113308 (2003).

[29] Liu W. and Asheghi M., Thermal Conduction in Ultrathin Pure and Doped Single-Crystal Silicon Layers at High Temperatures, *J. Appl. Phys.*, **98**, 123523 (2005).

[30] Liu W. and Asheghi M., Phonon-Boundary Scattering in Ultrathin Single-Crystal Silicon Layers, *Appl. Phys. Lett.*, **84**, 3819 (2004).

[31] Goodson K. E. and Ju, Y. S., Heat Conduction in Novel Electronic Films, *Annu. Rev. Mater. Sci.*, **29**, 261 (1999).

[32] Turney J. E., Mcgaughey A. J. H. and Amon C. H., In-Plane Phonon Transport in Thin Films, *Journal of Applied Physics*, **107**, 024317 (2010).

[33] Kittel C., Introduction to Solid State Physics, 8th Edition, (*Wiley*, New York 2005).

[34] Nika D. L., Zincenco, N. D. and Pokatilov E. P., Engineering of Thermal Fluxes in Phonon Mismatched Heterostructures, *J. Nanoelectronics and Optoelectronics*, **4**, 180 (2009).

[35] Cocemasov A. I. and Nika D. L., Phonons and Phonon Conductivity in Silicon Nanolayers, *J. Nanoelectronics and Optoelectronics*, **7**, 370 (2012).

[36] Thomas J. A., Turney J. E., Iutzi R. M., Amon C. H. and McGaughey A. J. H., Predicting Phonon Dispersion Relations and Lifetimes from the Spectral Energy Density *Phys. Rev. B*, **81**, 081411R (2010).

5 NANOPHONONIC METAMATERIALS: COHERENT THERMAL TRANSPORT SUPRESSION VIA LOCAL RESONANCE

Journal Version:
Under Preparation;

Preliminary Version:
Davis, B.L. and Hussein, M.I., "Reduction of thermal conductivity using nanophononic metamaterials," *Phononics 2013: 2nd International Conference on Phononic Crystals/Metamaterials Phonon Transport and Optomechanics.*, Sharm El-Sheikh, Egypt, 2 June - 7 June 2013.

5.0 Abstract

We present the concept of a locally resonant nanophononic metamaterial for the purpose of utilization as a thermoelectric material system exhibiting a high value of the *ZT* energy conversion figure-of-merit. The proposed concept enables an inherent reduction in the thermal conductivity, which is desired for increasing the *ZT* value. Furthermore, to achieve this reduction with practically no effect on the electrical conductivity (which is also needed for attaining a high *ZT* value), we choose a nanophononic metamaterial configuration consisting of a thin-film with a periodic array of pillars erected on one or two of the free surfaces. This configuration qualitatively alters the base thin-film phonon spectrum due to a hybridization mechanism between the pillar local resonances and the underlying lattice dispersion. Using a full lattice dynamics-based theoretical model (or a high resolution finite-element-based model for large sizes) that utilizes experimentally determined scattering constants; we explore the performance of the proposed material system in reducing the thermal conductivity compared to a corresponding uniform thin-film. The results show that with a 50-nm thick silicon thin-film (with smooth free surfaces), a lattice spacing of 60 nm and 80-nm tall pillars introduced on a single surface, the room-temperature thermal conductivity drops to approximately 60% of the corresponding uniform thin-film value (and to approximately 50% when pillars are introduced to both free surfaces). Upon parametric optimization, selection of other base materials, as well roughening of the free surfaces, additional

reductions in thermal conductivity are expected without a significant impact on the electrical conductivity. Compared to thin-film nanophononic crystals or thin-film superlattices, here there are no holes or layers that may impede the electron transport. However, the proposed pillared structure may still be utilized as an augmentation to existing thin-film-based nanophononic crystals or superlattices with proven improvements in the *ZT* figure-of-merit to provide a doubling, or more, of their performance. The proposed concept therefore provides a promising new paradigm for high-performance, scalable thermoelectric materials with a configuration that is easily integrated into devices.

5.1 Introduction

The utilization of nanostructured materials for control of heat transport is a rapidly growing field of interest [1-7]. Specifically, the manipulation of heat carrying phonons, or elastic waves that propagate and scatter at the nanoscale, can yield beneficial thermal properties [8]. One particular application relates to thermoelectric materials, or the concept of converting energy in the form of heat into electricity and vice-versa. In past studies, it has been proposed that nanoscale periodic patterning of dielectric materials can in principle be used to disrupt phonon transport in a way that has a minimal impact on electron transport. This is mainly due to the mismatch in the mean free path associated with the heat carrying phonons and that of the electrons (the latter is responsible for the electrical conductivity and is generally an order of magnitude smaller in size [8-11]). This ability to use nanostructuring to reduce the thermal conductivity without significantly affecting the electrical conductivity provides a promising avenue for achieving high values of thermoelectric energy conversion *ZT* figure-of-merit.

The manipulation of elastic waves in a periodic medium can be realized primarily in two distinct ways: 1) the utilization of phononic crystals and 2) the introduction of local resonance. The latter, which is proposed here for the first time for the reduction of thermal conductivity, renders the medium a "metamaterial". The concept of a phononic crystal [12, 13] involves a material with periodic patterning

for which the lattice spacing has a length scale on the order of the propagating waves, and hence wave scattering and interferences occur across the patterned unit cells thus providing a unique frequency band structure with the possibility of band gaps. Focusing on nanoscale phonon transport, the periodic patterning can be realized in a variety of ways such as by the layering of multiple materials with different phases, as in a superlattice [14-16]) or the introduction of holes and/or inclusions [17-23]. The concept of a metamaterial, on the other hand, generally involves the inclusion of local resonators which enable unique subwavelength properties to emerge. At the macroscale (where the focus is on acoustics and mechanical vibrations), locally resonant periodic metamaterials have been considered in various forms, such as by having heavy inclusions coated with a complaint material (e.g., rubber-coated lead spheres) hosted in a relatively lighter and less stiff matrix (e.g., epoxy) [24], or by the presence of pillars on a plate [25, 26].

In this work, we introduce the concept of an elastic metamaterial at the nanoscale, which we refer to as a *nanophononic metamaterial* (NPM). The goal is to significantly reduce the thermal conductivity in a nanostructured dielectric material system and to do so without affecting other important factors, especially the electrical conductivity. For both functional and practical purposes, we choose silicon thin-films as the platform material system that we use as a foundation to create a nanophononic metamaterial. Using a reduced-dimension material such as a thin-film already causes a reduction of thermal conductivity with little significant impact on the power factor, $S^2\sigma$ (where S is the Seebeck coefficient and σ is the electrical conductivity) [27-30], and is also favorable from the point of view of device integration. The choice of silicon is beneficial due to its wide use in the electronics industry and ease of fabrication; however other materials may be considered in the future. The resonators take the form of a periodic array of nanostructured pillars that extrude off the surface of the thin-film (on either one side or both sides, as practically permitted). A key advantage of this configuration is that the local resonances of the pillars may be tuned to interfere (or more specifically hybridize) with the underlying phonon

dispersion of the thin-film crystalline material in a way that lowers the thermal conductivity–a very favorable outcome for thermoelectric energy conversion. Another important benefit to utilizing pillars is that the feature manipulating the thermal transport (i.e., the pillar itself) is physically outside of the primary flow path of the electrons (which happens in the main body of the thin film). This is another key advantage compared to thin-film-based nanophononic crystals (which consist of holes drilled through the thickness of the thin-film and hence are more likely to have a negative effect on the electrical transport) or thin-film-based superlattices (in which the layers may similarly cause an obstruction to the electron transport). Thus, with the proposed pillared nanophononic material configuration, the concern about the competition between coherent and incoherent thermal transport and how to elucidate the interplay of these two mechanisms (in order to enable a most effective thermoelectric material design), are no longer of critical importance. Yet, for thin-film nanophononic crystals and thin-film superlattices with proven improvements in *ZT* values, the addition of a pillared array may be utilized as an "over and above" augmentation to the existing structure to provide a transformative improvement in performance.

In the following sections we describe our experimentally-fit theoretical models for the prediction of the thermal conductivity. In Section 5.2, we focus on uniform silicon thin-films, and in Section 5.3 we cover our treatment of the pillared nanophononic metamaterial and perform a parametric study in Section 5.4. In each section, we start by presenting our phonon dispersion models and proceed with the thermal conductivity prediction calculations on the basis of the dispersion curves we have as well as temperature-dependent empirical data for silicon thin-films. In Section 5.5, we present our conclusions.

5.2 Thermal Transport in Silicon Films

For this study we use silicon as our constituent material, considering that silicon has been extensively studied in the past both as a semiconductor and as a baseline thermoelectric material. We start by examining uniform silicon thin-films in order to obtain their anharmonic scattering constants (at

room temperature and as a function of thin-film thickness). These scattering constants will later be used for the pillared thin-film models since the pillars (being external to the main cross section of the nominal thin-film) are in principle not expected to significantly alter the phonon scattering within the underlying thin-film base structure.

The atomic structure of bulk silicon consists of a two-atom primitive cell which is extended across a face-centered (non-orthogonal) lattice to form the crystal structure. In order to create an atomic-level unit cell model for a uniform thin-film, and later for our pillared nanophononic metamaterial, we resort to a conventional cell (cc) description, which consists of eight atoms and is shaped as a simple cube with side length a = 0.54 nm. Due to this simple box-like structure, the conventional cell will be conveniently used as our building block which we will replicate along an orthogonal simple cubic lattice to generate a supercell for the thin-film structure, in either its uniform form or later when a pillar is added to the surface (or a pillar added to each of the free surfaces). For the uniform thin-film, the supercell consists of a vertical strip constructed by stacking M conventional cells on top of each other along the out-of-plane z-direction. The dimensions of this supercell will be denoted by $A_x \times A_y \times A_z$, where $A_x = A_y = a$ and $A_z = Ma = t$, where t is the thin-film thickness.

We obtain the phonon band structure for a set of uniform silicon thin-films by running lattice dynamics (LD) calculations [31, 32] in which the three-body Tersoff potential is used for the Si-Si bonds with only the first nearest neighboring interactions considered [33, 34]. We perform our LD calculations using the General Utility Lattice Program (GULP) [35]. Prior to calculating the phonon dispersion curves, the interatomic potential energy is minimized at constant pressure to relax the structure and ensure stability. This is especially relevant at the nominal boundary surfaces of the thin film. The Broyden-Fletcher-Goldfarb-Shanno (BFGS) optimization method [36] is used to accommodate these free boundaries.

For the thermal conductivity prediction, we use the Callaway-Holland model [37, 38] which integrates the contribution of each phonon mode in each dispersion branch over a given wavevector path, sums over all available branches and integrates across all other directions to cover the total volume of the supercell's Brillouin zone. Given that a thin-film represents a two-dimensional material (i.e., phonon wave motion is permitted only in the in-plane direction), the Callaway-Holland model takes the form of

$$k = \frac{1}{A_z \pi} \sum_{\lambda} \int_0^{\pi / A_x} C_{ph}(\kappa, \lambda)\, v_g^2(\kappa, \lambda)\, \tau(\kappa, \lambda)\, \kappa \, d\kappa \tag{5.1}$$

where κ, ω, C_{ph}, v, τ are the phonon's wavenumber, frequency, specific heat, group velocity and scattering time, respectively. The specific heat, group velocity and scattering time parameters are dependent on the phonon dispersion, i.e.,

$$C_{ph}(\kappa, \lambda) = k_B \left(\frac{\hbar \omega(\kappa, \lambda)}{k_B T} \right)^2 \frac{\exp(\hbar \omega(\kappa, \lambda)/k_B T)}{\left[\exp(\hbar \omega(\kappa, \lambda)/k_B T) - 1\right]^2} \tag{5.2}$$

$$v_g(\kappa, \lambda) = \frac{\partial \omega(\kappa, \lambda)}{\partial \kappa} \tag{5.3}$$

$$\begin{aligned} \tau(\kappa, \lambda) &= \left(\frac{1}{\tau_U(\kappa, \lambda)} + \frac{1}{\tau_I(\kappa, \lambda)} + \frac{1}{\tau_B(\kappa, \lambda)} \right)^{-1} \\ &= \left(AT\omega^2(\kappa, \lambda) \exp(-B/T) + D\omega^4(\kappa, \lambda) + \left| v_g \right| / A_z \right)^{-1} \end{aligned} \tag{5.4}$$

where T is temperature, k_B is the Boltzman constant, $\hbar$ is the adjusted Plank's constant, a is the lattice spacing, A and B are the Umklapp scattering parameters and D is the scattering impurity parameter. The Umklapp scattering properties accounts for the phonon-phonon interactions. For bulk systems, these parameters are usually fitted to bulk empirical measurements as a function of temperature. Upon constricting the lattice to a 2D thin-film with finite surfaces, the bulk scattering parameters are no longer

valid. As a result, the scattering parameters are necessarily fitted to empirical thin-film measurements. Due to the high sensitivity of these parameters to the film thickness (especially for very low thicknesses), we fit the parameters for a variety of thin-film thicknesses. Due to the availability of empirical data, we fit for the thicknesses measuring t = 20, 30, 50, 100, 420 nm around a temperature of T = 300K. Figure 5.1a shows the empirical data (marked with dots) as well as the fitted results for thin-films of various

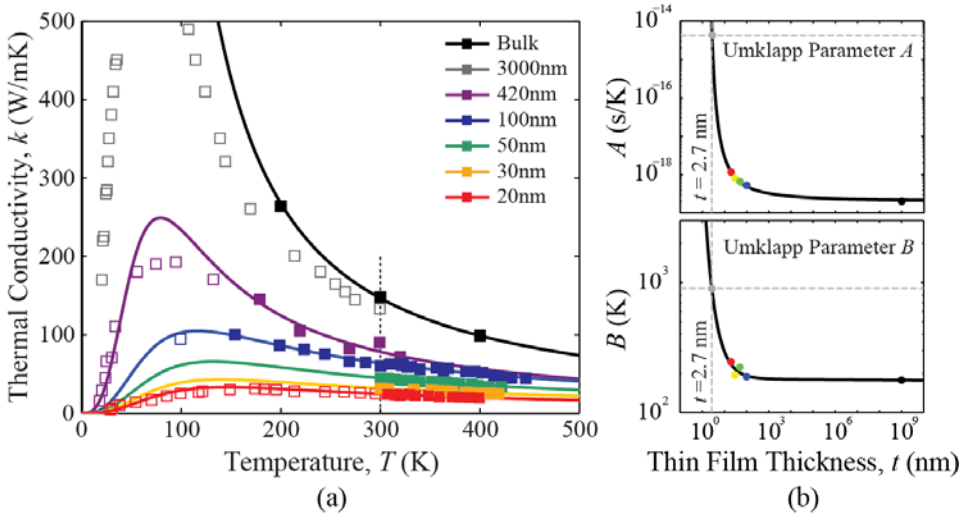

Figure 5.1: (a) Thermal conductivity as a function of temperature for various thin-films and (b) Umklapp scattering parameters, A and B, as a function of thin-film thickness. These parameters are determined by fitting the thermal conductivity predictions with the empirical data point shown (left). Here the squares are measurements and the solid lines represent the fitted model. We find that the Callaway-Holland 2D thermal conductivity formulation well represents the experimental thermal conductivity values for various thicknesses and temperatures. For thin-films beyond the thickness which is empirically available, we extrapolate (right) as demonstrated for the thickness value of t = 2.7 nm.

thicknesses. It is noted that due to the limited availability of data across a wide temperature range, only the solid dots were considered for the fitting to ensure the expected trends at T = 300K. Upon obtaining the parameter values for an adequate number of thin-film thicknesses, a second level of curve fitting was performed to harness scattering parameters for a wide range of thin-films as shown in Figure 5.1b. In preparation for investigating a pillared thin-film with pillars (which is done later), we consider a uniform

thin-film with a thickness of t = 2.7 nm; the selected Umklapp parameters for this thickness are marked in Figure 5.1b.

The background concerning the crystal structure and modeling of silicon, the formulation of lattice dispersion for thin-films, as well as the 2D derivation and calculation of thermal conductivity are discussed extensively in Chapters 3 and 4. In addition, the fitting process used to determine the scattering parameters is outlined in Chapter 4.

5.3 Introduction of Pillars to Form a Nanophononic Metamaterial

We now turn to the main focus of this work which is to determine how the presence of nanostructured resonating pillars reduces the thermal conductivity in a thin-film. Our baseline study consists of a supercell cell with a square base of 6×6 conventional cells (A_x = A_y = 3.26 nm) and a thickness of M = 5 conventional cells (A_z = t = 2.72 nm); this corresponds to a rectangular solid containing of 1440 atoms. Here the top and bottom of the unit cell are free surfaces with the phonon wave motion only enabled along the in-plane directions. The pillar is placed at the top of the thin-film and has a square base of 2×2 conventional cells (side length of D = 1.09 nm) and a height of 3 conventional cells (H = 1.63 nm) and itself contains 96 atoms. This geometrical configuration can be seen in Fig 5.2 (far right, top).

The phonon dispersion is shown in the same figure (Fig. 5.2) for both the uniform thin-film (far left) and the thin-film with the presence of the pillar (far right). The dispersion curves themselves are colored in a manner that reflects the contribution of thermal conductivity for each particular branch and wave number. The colors are normalized so that the branch and corresponding wave number with the highest contribution to the thermal conductivity is equal to one (independently for each plot). We note that per our previous discussion, the Umklapp scattering parameters are set for t = 2.7-nm thin-film as shown in

Fig 5.1b. We sum the cumulative contribution of thermal conductivity as a function of frequency (center). We note several observations from Fig. 5.2: (1) the lower branches (acoustical) contribute to a

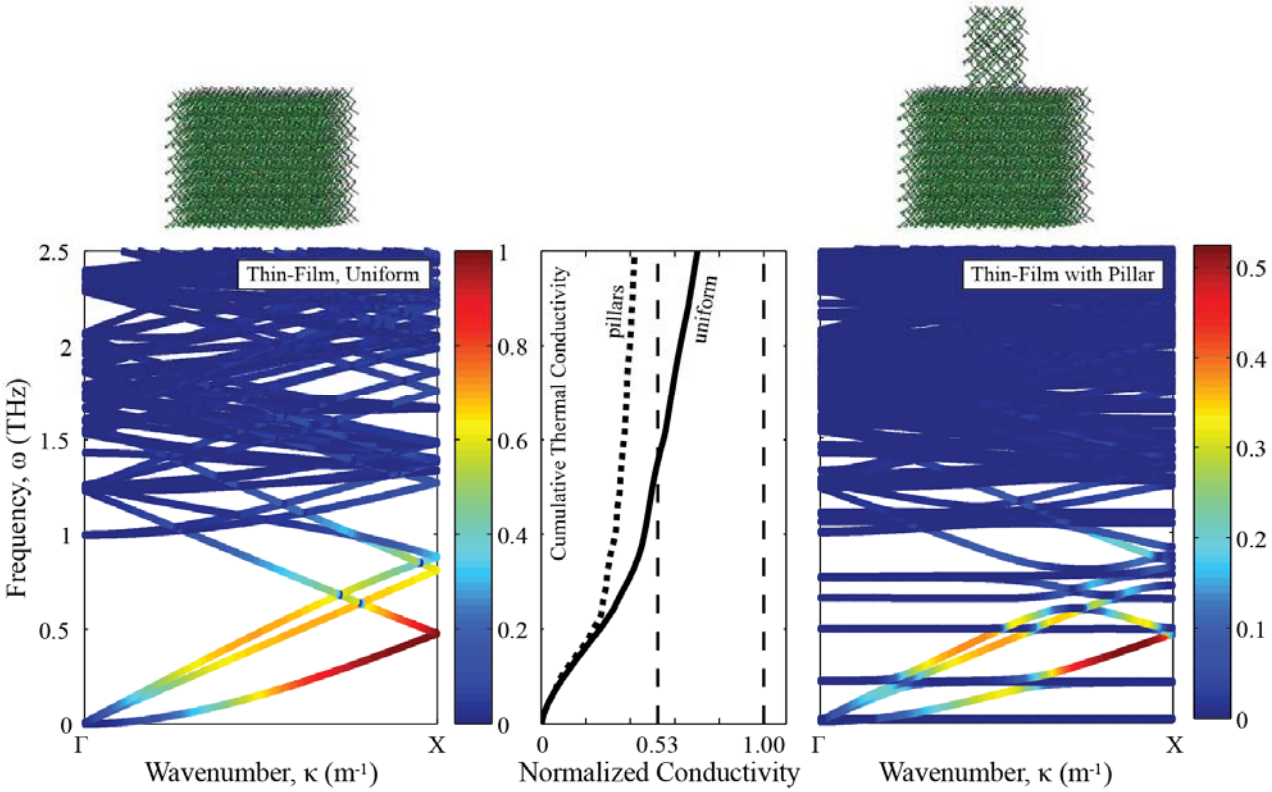

Figure 5.2: Comparison of the dispersion and thermal conductivity of uniform silicon thin-films with the case of a thin-film with pillars. Dispersion is colored in a manner which reflects the normalized contribution to thermal conductivity. We note the dramatic change to the dispersion and the resulting reduction in thermal conductivity, which occurs due to the addition of the pillar.

significant portion of the thermal conductivity in the thin-film. In addition, we see that the higher wavenumbers (contrary to the bulk case) also significantly contribute to the thermal conductivity. One factor to note here is that the boundary scattering term is being based on a very small value of minimum feature size, L, as this is set to be equal to the thin-film thickness of t = 2.7 nm. When L is very small, the long waves (i.e., those near the Γ-point in the band diagram) are effectively eliminated and hence we get the low contribution at the lower end of the acoustical branches. (2) The presence of the pillar causes a

series of flat locally resonant phonon modes to appear. These modes interact with the underlying acoustic phonons and form a hybridization of the dispersion curves; this leads to a flattening of the branches and as such a reduction in the group velocities and hence the thermal conductivity. (3) We note that the acoustic branches (first three branches > 1THz) for the uniform case contributes approximately 40% of the thermal conductivity. The presence of the pillars significantly modifies both the magnitude and prominence of these acoustic branches, which now contributes > 50% of the thermal conductivity. With the pillar, nearly 80% of the thermal conductivity is below 2.5 THz while for the uniform case this around ~70% is below this frequency.

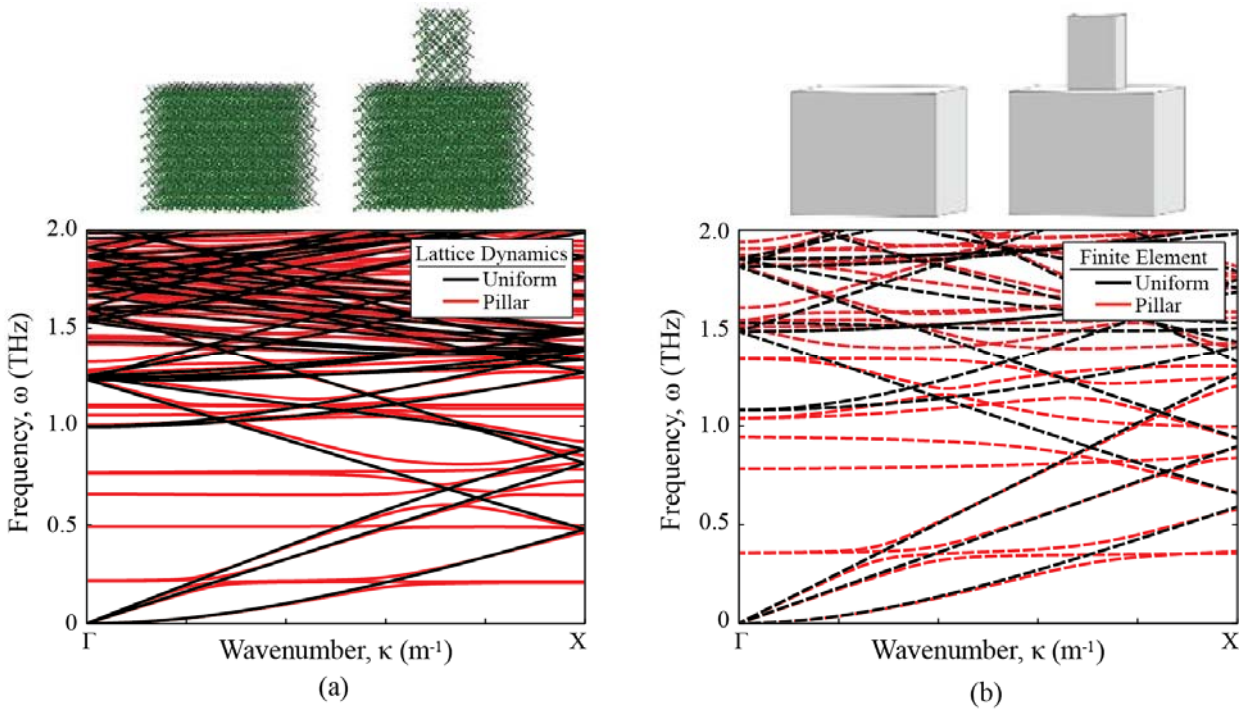

Figure 5.3: Dispersion curves of the thin-film, with and without pillars. The dispersion is found using the atomic lattice dynamics model (left) and the continuum-based finite element model (right).

For the cases considered thus far, we have modeled the dispersion of the thin-film with pillars utilizing lattice dynamics. The clear benefit of LD is that it enables us to model the motions in the thin-film and the pillars with atomic resolution, and hence enable an accurate depiction of the wave properties

in the nanostructured material. Due to limited computational resources, however, this type of model is limited to very small sizes (roughly up to where the feature length of a supercell cell is 5 nm). Given that current technologies in nanostructured manufacturing are limited to minimum feature sizes roughly an order of magnitude larger, we turn to a continuum-based finite-element (FE) model, albeit we pay special attention to the finite element resolution with respect to the number of elements per conventional cell. In Figure 5.3, we compare the first few branches of dispersion between the LD and FE formulation for unit cells with and without the pillar. For this comparison we use a supercell with identical dimensions to our previous case study. For the FE model, we utilize 12×12×10 elements to form the thin-film and 4×4×6 elements for the pillar. This resolution was selected to approximately match the total degrees-of-freedom between the FE and LD models. Here the model size for the FE case is 5202/4752 degrees-of-freedom [with/without the pillar] and 4608/4320 for the LD case. In addition, the FE mesh was selected to ensure cubic elements. We find that there are key similarities between the two models: For the uniform thin-films we observe three unique acoustic branches, one of which is flat near the Γ-point indicating plate-like motion. In addition, we see similar branch folding and degeneracy in the dispersion. With the addition of the pillar, we see flat horizontal branches appear that intersect the acoustic branches. Adjacent to these intersections, the slope is dramatically reduced causing a lower group velocity; this occurs in the higher branches as well. There are some variances however between these LD and FE models with the most noteworthy being the differences in slope of the acoustic branches at high wavenumbers and the slightly higher frequency for the optical and resonant branches of the FE model. On the other hand, the long wave slopes of the acoustic branches are almost identical, which provides an important verification.

As discussed above, the main benefit of using the continuum-based FE model for formulating dispersion is the ability to reduce the size of the computational model. As a result, unlike the LD formulation, discretion is given to select a finite-element resolution that adequately captures, at least qualitatively, the nanoscale effects. To understand the sensitivity of the FE resolution on the thermal

conductivity prediction, we directly compare with the thermal conductivity formulation on a series of unit cells utilizing both FE and LD models. To take advantage of the relatively simple geometry, we vertically stack a series of conventional cells on top of each other (i.e., a 1×1 conventional cell base) which allows us to model relatively thick thin-films by lattice dynamics without exceeding the computational limitations. These supercell 'strips' have a base length of $A_x = a = 0.54$ nm and a thickness of $A_z = t$. For each thickness, the Umklapp scattering parameters are adjusted per the curve fit technique in Figure 5.1 to ensure the appropriate phonon-phonon interactions are met.

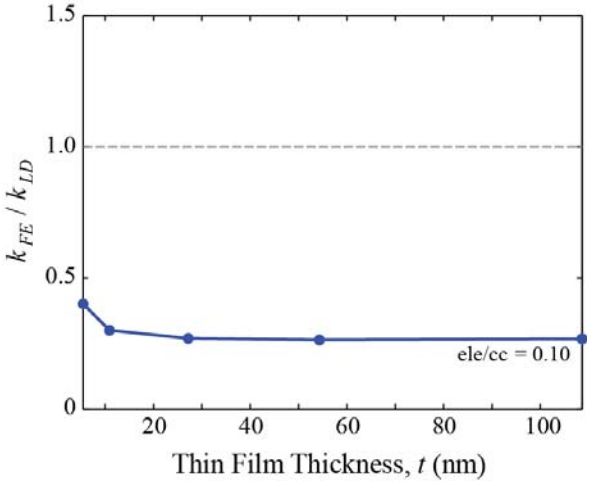

Figure 5.4: Comparison between the prediction of the thermal conductivity utilizing lattice dynamics (LD) and the finite element method (FE). The FE resolution is described in terms of number of finite elements per a conventional cell (cc). The results show that the performance of the FE model is independent of thickness for thicknesses between 20 and 100 nm. Both models are based on a thin unit cell 'strip' of finite thickness t and periodic boundaries along the in-plane directions.

In Figure 5.4, the ratio of the thermal conductivity prediction of the FE model compared to the lattice dynamics model is plotted as a function of thin-film thickness. The number of elements used in the FE model is reported as a ratio to the number of equivalent conventional cells in the LD model. Along the *x-y* directions (in-plane), three elements were used for each case resulting in a resolution of 3 n_{el}/cc while along the vertical direction the resolution considered was 0.1 n_{ele}/cc. We note that across a prescribed

thickness the relative prediction of the thermal conductivity using LD versus the FE method converges to a constant value and becomes relatively flat. This enables us to directly correlate (with a ratio offset) the thermal conductivity by these two modeling techniques for a prescribed n_{ele}/cc resolution. When utilizing FE methods it is important to ensure that the resolution is high enough to effectively capture the effects of the overall unit cell configuration on the general dispersion picture and subsequently on the nanoscale mechanism of thermal transport. In Figure 5.5 we directly compare the reduction in thermal conductivity for a thin-film with and without the pillars for various element resolutions and wavenumber step sizes. We select a cubic supercell with a side length of a_{NPM} = 3.26 nm and a pillar with a base side length of D = 1.08 nm and a height of H = 2.17 nm. These dimensions were selected to enable comparison with the LD model where the base length is equivalent to A_x = 6 conventional cells and a pillar base and height of 2 and 4 nm, respectively.

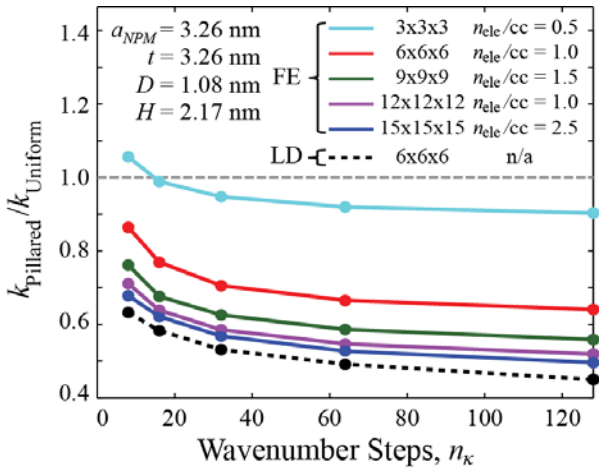

Figure 5.5: Comparison of thermal conductivity of thin-films with and without the presence of a pillar utilizing FE of varying n_{ele}/cc and n_κ resolutions (solid lines). The unit cell dimensions of the FE are equivalent to the LD formulation (dashed lines) to enable a direct comparison. Here the thin-film thickness is set to t = 3.26 nm.

We find that as we increase the number of n_κ points or the wavenumber discretization resolution, which numerically improves the prediction of the Callaway-Holland model, the thermal conductivity converges to a constant value. In addition, when the number of elements is increased, the reduction in

thermal conductivity due to the presence of the pillar also converges to constant value. This is evident in Figure 5.5 as the number of elements is increased for a fixed number of wavenumber steps, n_κ. Finally, we note that with increased finite-element resolution, the FE model maintains a consistent trend and approaches the LD model. This spurs further confidence that, for the selected resolutions, the FE model appears to be adequately capturing the nanoscale phonon dynamics behavior as far as the effects of the pillars on the overall dispersion, and hence the thermal conductivity reduction, are concerned.

It should be noted however that while the n_{ele}/cc resolution in Figure 5.5 is set at a level which is adequate, the notion of scalability (which exits in the FE treatment of macroscale low-frequency problems) needs to be first verified before proceeding further. Consequently, a similar convergence study is applied for a thin-film with a thickness of t = 60 nm as shown in Figure 5.6; this corresponds to a base

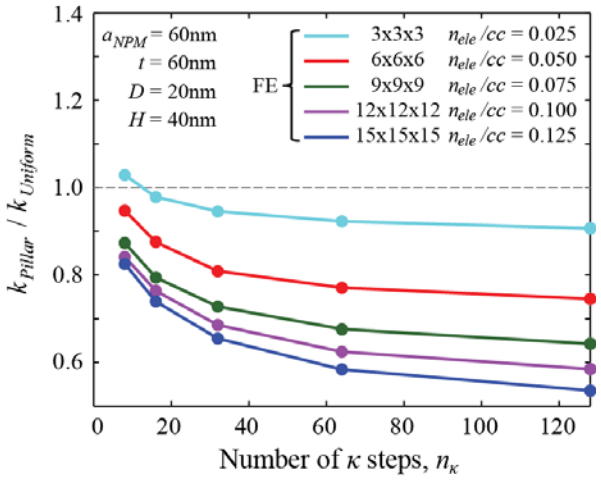

Figure 5.6: Comparison of thermal conductivity of thin-films with and without the presence of a pillar utilizing FE of varying n_{ele}/cc resolution and n_κ resolutions (solid lines). Here the thin-film thickness is set on the order of t = 60 nm.

length of a_{NPM} = 60 nm, pillar width of D = 20 nm and a pillar height of H = 40 nm. Here we consider coarser resolutions than before, yet we observe that the reduction in the thermal conductivity has similar convergence trends with those shown in Figure 5.5. Upon evaluating Figures 5.4 through 5.6, we set

n_κ = 129 and n_{ele}/cc = 0.109 for all remaining cases within this study. This resolution sets the base length of each cubic finite element to be fixed to 5nm in length.

Finally, we plot the full dispersion with the chosen finite element and n_κ step resolutions for a thin-film with a thickness of t = 50 nm, a_{NPM} = 60 nm and D = 20 nm, with and without the presence of a pillar of H = 80nm, in Figure 5.7. We note that upon comparing full dispersion we see a few distinctive traits: (1) that the maximum frequency remains consistent regardless of the extra branches present due to added degrees of freedom of the pillar, and (2) despite additional degrees of freedom, the thin-film with the pillar has a reduced thermal conductivity due to the introduction of the local resonance branches to the phonon spectrum and the subsequent hybridization with the underlying thin-film dispersion.

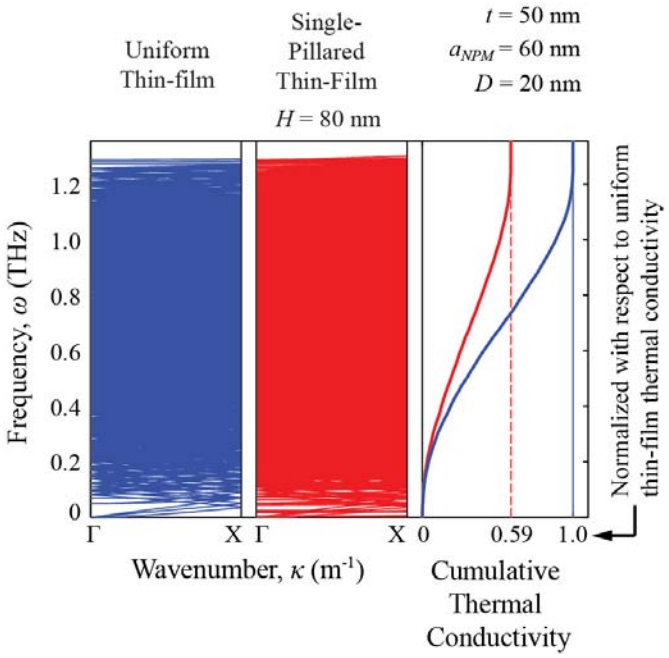

Figure 5.7: Full dispersion and thermal conductivity comparison of a thin-film with (blue) and without (red) the presence of a pillar, utilizing the high-resolution FE model.

5.4 Parametric Study

We have demonstrated the general reduction in the thermal conductivity of thin-films with the presence of a pillar. We next take a closer look at how the height and spacing of the pillar on the thin-

film surface impacts the contribution to the thermal conductivity. Figure 5.8 (top) shows the dispersion of a thin-film with varying pillar height H. For this case we utilize the parameters of $t = a_{NPM} = 60$ nm and $D = 20$ nm. We see that as the pillar height is increased the density of dispersion branches at lower frequencies is increased, primarily due to the lowering of the fundamental resonance frequency and its harmonics. This description is illustrated in Figure 5.8 (top) by looking at the horizontal branches corresponding to the local resonance frequencies and their interaction with the underlying dispersion branches. This effect of the local resonances takes place throughout the entire frequency spectrum and therefore has a significant effect on the thermal conductivity.

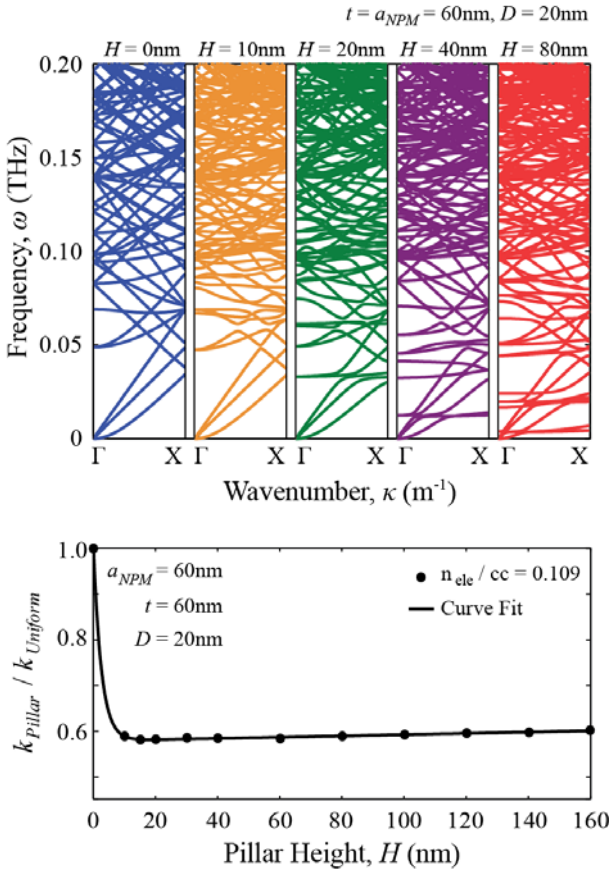

Figure 5.8: Dispersion comparison of a $t = 60$ nm thin-film with the presence of a pillar of varying height H (top) and the computed reduction in thermal conductivity with an exponential curve fit to capture the trend (bottom).

When evaluating thin-films with a varying pillar height, we compute the thermal conductivity utilizing all branches while recognizing that the taller the pillar, the more branches are available and incorporated. We find in Figure 5.8 (bottom) that for small pillar heights, an increase in pillar height causes the thermal conductivity to decrease further (in line with a lowering of the resonant frequencies), reaching a value of 60% of the uniform thin-film thermal conductivity. However above a particular value, the reduction becomes less profound, and in fact reverses, as the pillar height increases. This may be attributed to the increase in coupling between the pillar motion and that of the thin-film itself, considering the increasing ratio of the pillar height with respect to the thin-film thickness.

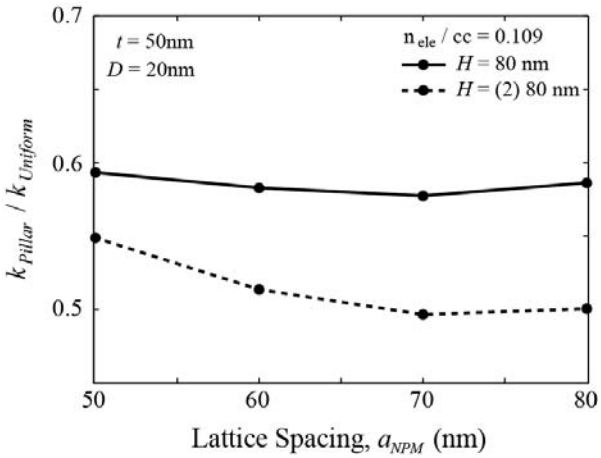

Figure 5.9: Computed reduction in thermal conductivity for a thin-film of t = 50 nm with a periodic array of pillars of varied lattice spacing, a_{NPM}. The dashed line indicates a double pillar.

This effect can be further illustrated in Figure 5.9 where for a fixed pillar height, the lattice spacing a_{NPM} (i.e., supercell length) is adjusted to vary the spatial density of the pillars erected on the thin-film. For the case of high lattice spacing, an increased spacing reduces the density of the pillars on the thin-film surface which adversely impacts the thermal conductivity reduction. On the contrary when the lattice spacing is small, an reduction in lattice spacing increases the coupling between the resonator and the thin film and hence also adversely affects the thermal conductivity reduction. As a result, for the case of a

pillar height of H = 80nm (the solid black line in Figure 5.9) we see a minimum thermal conductivity reduction at a_{NPM} = 70nm.

Finally, under the circumstances where the thin-film is suspended, the ability to implement pillars on both free surfaces may be realized. As a result, we can effectively double the number of pillars present on the thin-film. In Figure 5.9 we find that there is an even greater reduction in the thermal conductivity, to 50% of the uniform thin-film value, when utilizing double pillars (dashed black line). Upon investigating the dispersion of the double pillar thin-films, we see in Figure 5.10 that additional branches around the resonant frequencies. Although this addition has caused a further reduction in the thermal conductivity, the relative improvement is not as significant as adding just a single pillar.

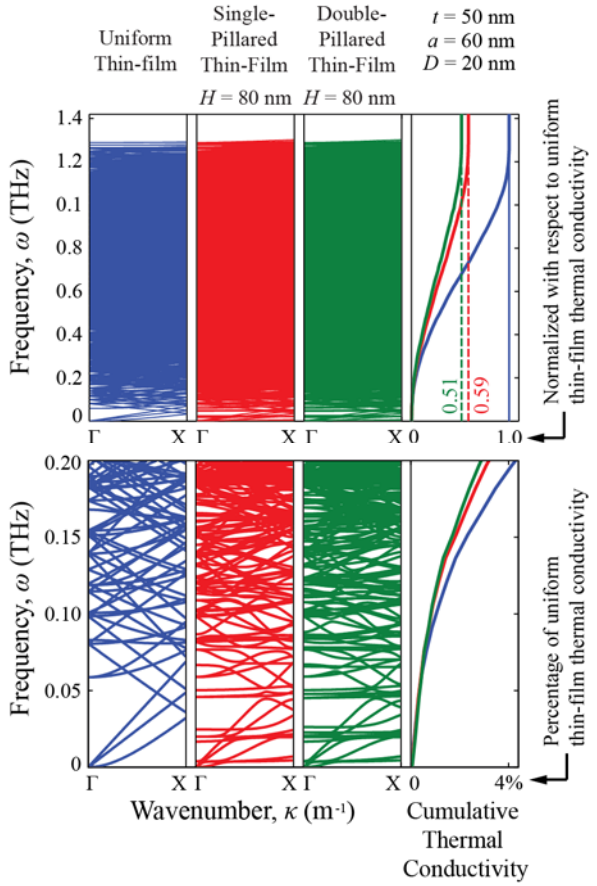

Figure 5.10: Dispersion comparison of a uniform t = 50 nm thin-film (left), with an 80 nm single pillar (center) and an 80 nm double pillar (right). The first few dispersion branches are shown as well as the cumulative thermal conductivity as a function of frequency.

5.5 Conclusion

In this work, we investigated the concept of augmenting thin-films with nanostructured pillars as an approach to reducing thermal conductivity. In principle, the introduction of the pillars renders the thin-film a nanophononic metamaterial. We utilized both lattice dynamics and finite-element based formulations to model the phonon dispersion. Upon directly comparing the frequency spectra of a thin-film with pillars versus one without pillars, it was noted that there are key favorable changes in the dispersion due to the presence of the pillars. By using the Callaway-Holland model to compute the thermal conductivity (utilizing phonon dispersion), we found that the predicted reduction in the thermal conductivity by the FE model converged to a constant offset value compared to the LD results for thin-films with a thickness-pillar spacing on the order of ~5nm. For a larger model (in the order of 50nm thickness-pillar spacing), the FE results converged with increasing resolution. We note that unlike the LD formulation, a finite-element resolution has to be selected to ensure that the nanoscale effects are properly represented while staying within the bounds of available computational resources. It was found that for the selected unit-cell sizes, the presence of a pillar on the thin-film enabled a noticeable reduction in the thermal conductivity to approximately 60% and 50% of the uniform thin-film value for a single and double pillar, respectively.

The results of this work yield a favorable outcome for thermoelectric materials. Utilizing thin-films with nanostructured resonators has been shown to significantly lower the thermal conductivity without altering the core material and hence having a minimal effect on the electrical conductivity, leading to a scenario that is ripe for improvement in the thermoelectric figure-of-merit. A follow-on investigation to confirm our assumption that electron transport is uninhibited by the pillars is an important next step in analytically determining the true thermoelectric energy conversion gains from the inclusion of the pillars.

5.6 Acknowledgements

The authors would like to thank Dr. Eduardo A. Misawa and the National Science Foundation for their support for this research under Grant No. CMMI 0927322. In addition, the authors would like to thank Osama R. Bilal for his assistance in setting up the finite element meshes used in this study.

5.7 References

[1] Balandin A. A. and Wang K. L., Significant Decrease of the Lattice Thermal Conductivity Due to Phonon Confinement in a Free-Standing Semiconductor Quantum Well, *Phys. Rev. B*, **58**, 1544 (1998).

[2] Balandin A., Thermal Properties of Semiconductor Low-Dimensional Structures, *Phys. Low-Dimens. Str.*, **1–2,** 1 (2000).

[3] Chen G., Heat Conduction in nanostructures, *Int. Jour. Therm. Sci.*, **39**, 471 (2000).

[4] Chen G., Particularities of Heat Conduction in Nanostructures, *J. Nanoparticle Research*, **2**, 199 (2000).

[5] Li D., Wu Y., Kim P., Shi L., Yang P. and Majumdar A., Thermal Conductivity of Individual Silicon Nanowires, *Appl. Phys. Lett.*, **83**, 14 (2003).

[6] Chen G., Narayanaswamy A. and Dames C., Engineering Nanoscale Phonon and Photon Transport for Direct Energy Conversion, *Superlattice. Microst.*, **35**, 161 (2004).

[7] Balandin A. A., Nanophononics: Phonon Engineering in Nanostructures and Nanodevices, *J. Nanosci. Nanotechnol.*, **5**, 1015 (2005).

[8] Dresselhaus M. S., Chen G., Tang M., Yang R., Lee H., Wang D., Ren Z., Fleurial J. and Gogna P., New Directions for Low-Dimensional Thermoelectric Materials, *Adv. Mater.*, **19**, 1043 (2007).

[9] Snyder G. J. and Toberer E. S., Complex Thermoelectric Materials, *Nat. Mater.*, **7**, 105 (2008).

[10] Vineis C. J., Shakouri A., Majumdar A. and Kanatzidis M. G., Nanostructured Thermoelectrics: Big Efficiency Gains from Small Features, *Adv. Mater.*, **22**, 3970 (2010).

[11] Li J., Liu W., Zhao L. and Zhou M., High-Performance Nanostructured Thermoelectric Materials, *NPG Asia Mater.*, **2**, 152 (2010).

[12] Sigalas M. and Economou E. N., Band Structure of Elastic Waves in Two Dimensional Systems, *Solid State Commun.*, **86**, 141 (1993).

[13] Kushwaha M. S., Halevi P., Dobrzynski L. and Djafari-Rouhani B., Acoustic Band Structure of Periodic Elastic Composites, *Phys. Rev. Lett.*, **71**, 2022 (1993).

[14] Cleland N., Schmidt D. R. and Yung C. S., Thermal Conductance of Nanostructured Phononic Crystals, *Phys. Rev. B*, **64**, 172301 (2001).

[15] McGaughey A. J. H., Hussein M. I., Landry E. S., Kaviany M. and Hulbert G. M., Phonon Band Structure and Thermal Transport Correlation in a Layered Diatomic Crystal, *Phys. Rev. B*, **74**, 104304 (2006).

[16] Laundry E. S., Hussein M. I. and McGaughey A. J., Complex Superlattice Unit Cell Designs for Reduced Thermal Conductivity, *Phys. Rev. B*, **77**, 184302 (2008).

[17] Gillet J. N., Chalopin Y. and Volz S., Atomic-Scale Three-Dimensional Phononic Crystals With a Very Low Thermal Conductivity to Design Crystalline Thermoelectric Devices, *J. of Heat Trans.*, *ASME* **131**, 043206 (2009).

[18] Tang J., Wang H-T., Lee D. H., Fardy M., Huo Z., Russell T. P. and Yang P., Holey Silicon as an Efficient Thermoelectric Material, *Nano Lett.*, **10**, 4279 (2010).

[19] Yu J., Mitrovic S., Tham D., Varghese J. and Heath J., Reduction of Thermal Conductivity in Phononic Nanomesh Structures, *Nat. Nanotechnol.*, **5**, 718 (2010).

[20] Hopkins P. E., Reinke C. M., Su M. F., Olsson III R. H., Shaner E. A., Leseman Z. C., Serrano J. R., Phinney L. M. and El-Kady I., Reduction in the Thermal Conductivity of Single Crystalline Silicon by Phononic Crystal Patterning, *Nano Lett.*, **11**, 107 (2011).

[21] He Y. P., Donadio D., Lee J. H., Grossman , J. C. and Galli G., Thermal Transport in Nanoporous Silicon: Interplay Between Disorder at Mesocopic and Atomic Scales, *ACS Nano*, **5**, 1839 (2011).

[22] Davis B. L. and Hussein M. I., Thermal Characterization of Nanoscale Phononic Crystals using Supercell Lattice Dynamics, *AIP Advances*, **1**, 041701 (2011).

[23] Robillard J. F., Muralidharan K., Bucay J., Deymier P. A., Beck W. and Barker D., Phononic Metamaterials for Thermal Management: An Atomistic Computational Study, *Chinese J. Phys.*, **49**, 448 (2011).

[24] Liu Z., Zhang Z., Mao Y., Zhu Y. Y., Yang Z., Chan C. T. and Sheng P., Locally Resonant Sonic Materials, *Science*, **289**, 5485 (2000).

[25] Pennec Y., Djafari-Rouhani B., Larabi H., Vasseur J. O. and Hladky-Hennion A. C., Low-Frequency Gaps in a Phononic Crystal Constituted of Cylindrical Dots Deposited on a Thin Homogenous Plate, *Phys. Rev. B*, **78**, 104105 (2008).

[26] Wu T. T., Huang Z. G., Tsai T. C. and Wu T. C., evidence of Complete Band Gap and Resonances in a Plate with Periodic Stubbed Surface, *Appl. Phys. Lett.*, **93**, 111902 (2008).

[27] Liao C. N., Chen C. and Tu K. N., Thermoelectric Characterization of Si Thin Films in Silicon-on-Insulator Wafers, J. Appl. Phys., **86**, 32014 (1999).

[28] Venkatasubramanian R., Siivola E., Colpitts T. and O'Quinn B., Thin-Film Thermoelectric Devices with High Room-Temperature Figures of Merit, *Nature*, **413**, 597 (2001).

[29] Hochbaum A. I., Chen R., Delgado R. D., Liang W., Garnett E C., Najarian M., Majumdar A. and Yang P., Enhanced Thermoelectric Performance of Rough Silicon Nanowires, *Nature Lett.*, **45**, 163 (2008).

[30] Boukai A. I., Bunimovich Y., Tahir-Kheli J., Yu J-K., Goddard III W. A. and Heath J. R., Silicon Nanowires as Efficient Thermoelectric Materials, *Nature Lett.*, **451**, 168 (2008).

[31] Dove M. T., Introduction to Lattice Dynamics, (*Cambridge University Press,* Cambridge, 1993).

[32] Maradudin, A. A., Montroll, E.W. and Weiss, G. H., Theory of Lattice Dynamics in the Harmonic Approximation, (Academic Press, New York, New York 1963).

[33] Tersoff J., New Empirical Approach for the Structure and Energy of Covalent Systems, *Phys. Rev. B*, **37**, 6991 (1988).

[34] Tersoff J., Empirical Interatomic Potential for Silicon with Improved Elastic Properties, *Phys. Rev. B*, **38**, 9902 (1988).

[35] General Utility Lattice Program, https://www.ivec.org/gulp.

[36] Shanno D. F., Conditioning of Quasi-Newton Methods for Function Minimization, *Math. Comput.*, **24**, 647 (1970).

[37] Callaway J., Model for lattice Thermal Conductivity at Low Temperatures, *Phys Rev.*, **113**, 1046 (1959).

[38] Holland M. G., Analysis of Lattice Thermal Conductivity, *Phys. Rev.*, **132**, 2461 (1963).

6 CONCLUSION

6.1 Summary of Dissertation

In Chapter 1, the concept of thermoelectric energy conversion was introduced emphasizing the potential that this technology has in changing the way we approach common challenges in energy generation and heat management. The limitations of this technology were outlined and the different approaches in the literature to surmount this challenging problem, at the material-level, were briefly reviewed. Motivated by the potential impact of a successful solution to the problem of increasing the values of *ZT*, this dissertation aims to utilize nanoscale phononic materials as a means for reducing the thermal conductivity with little alteration of the electrical conductivity-an outcome that will inevitably increase the values of the figure-of-merit. Two types of nanoscale phononic materials were studied in this work: 3D bulk NPCs and 2D thin-film nanoscale phononic metamaterials. The former is formed by drilling a periodic array of cubic voids in bulk silicon, and the latter by erecting a periodic array of pillars on the surface of a flat plate-like thin-film also composed of silicon. For comparison, the nominal cases of 3D uniform bulk and 2d uniform thin-films were also investigated (as these provided bench-mark reference configurations to which the properties of new nanoscale phononic materials were compared). The remainder of this chapter introduced the tools needed and current challenges for computing the thermal conductivity for the various nanostructured material systems considered. Finally, an in-depth literature search was provided on current research topics in thermoelectric devices, periodic materials, lattice dynamics and nanoscale heat transfer.

6.1.1 Lagrangian Lattice Dynamics

Chapter 2 focused on the process of utilizing lattice dynamics to calculate wave propagation in a crystalline nanoscale phononic material. It was noted that atomic scale dynamic motion is commonly modeled following Newtonian mechanics where the exerted inter-atomic forces applied on each atom are

balanced to form the equations of motion. In this work, a Lagrangian mechanics-based formulation was implemented to simplify the formation of the equations of motion; enabling fewer force constants to represent the atomic interactions. In addition, this formulation enables for practical means for incorporating other physical phenomenon such as damping, non-linearity and truncation of periodicity. This method was implemented for a simple cubic lattice nanoscale phononic crystal (not based on a realistic constituent material) and found to be consistent with the Newtonian formulation. As a case study, the phonon dispersion was generated for a supercell containing 5×5×5 atoms one of which was 'defected' and set to have a higher mass. The defect caused the phonon dispersion to exhibit a band gap or a frequency range where wave propagation is inhibited. The frequency range of the band gap increased as the mass of the defected atom was increased in value. The ability to control the size and location of a band gap at the nanoscale leads to opportunities in engineering materials with desired thermal transport properties.

6.1.2 Nanoscale Phononic Crystals

The next natural step was to model the phonon wave propagation of a practical crystalline material-based NPC and to compute its thermal conductivity. For the remainder of the work in this dissertation, silicon was selected due to its widespread availability and potential to serve as a thermoelectric material. In Chapter 3, the conventional silicon unit cell was used as a building block for the creation of a 3D bulk NPC, and the corresponding dispersion was used to compute the thermal conductivity utilizing the Callaway-Holland formulation. First, however, a modeling approach had to be established since a NPC may only be represented by a supercell, and there are limited studies in the literature concerned with supercell lattice dynamics and thermal conductivity prediction. Using the primitive cell as a model for bulk, unpatterned silicon as a reference, the thermal conductivity was calculated for a uniform supercell with a cubic form factor. It was found that the thermal conductivity of the uniform supercell converges to

that obtained by the primitive cell as the supercell size and wave-vector resolution are increased. With a thorough understanding of the dynamics and thermal transport behavior of the uniform supercell, the next step was to reduce the thermal conductivity by creating a 3D NPC. This was enabled by removing clusters of atoms in the supercell to create a cubic void (i.e., a hole). When comparing dispersion, a significant difference can be seen between a 3D uniform crystal and NPC crystal, mainly a general reduction in frequency and flattening of the branches occurs. For the thermal conductivity prediction, the phonon scattering rate was determined by fitting with empirical bulk data–which is a rather rough approximation but still useful in providing initial insights on the comparative roles of dispersion and Umklapp scattering. Upon investigating the contribution of each phonon branch to the thermal transport, it was found that the acoustic branches contribute to the majority of the thermal conductivity, even when these branches are flattened due to the added periodicity. In addition, the role of the material and boundary scattering phenomenon were illustrated, and it was observed that the dispersion associated with the NPC plays a noticeable role in affecting the thermal conductivity even in the presence of sever boundary scattering.

6.1.3 Nanoscale Phononic Metamaterials

The final focus area of this dissertation investigated 2D uniform thin-films both with and without the presence of pillars. The latter case provided a novel application of the theory of metamaterials–currently widely studied in acoustics–to the problem of nanoscale phonon transport. But before this prime contribution is discussed further, it is noteworthy to elaborate on the modeling benefits of moving from a 3D NPC to a 2D thin-film, regardless of the presence of pillars. Although the 3D NPC case provided unique insights in modeling the thermal conductivity of supercells as well as the treatment of material and boundary scattering, there was an uncertainty in the model setup that was resolved upon moving to unvoided thin-films. This involved the treatment of the scattering parameters which needs to be fitted to

empirical data. Contrary to a 3D NPC, the thermal conductivity of thin-films has been extensively studied for a variety of thicknesses. This allowed us to use proper boundary scattering parameters, obtained directly from temperature-dependent experimental data. This advantage carried through the modeling of the NPM because the pillars are placed external to the main skeleton of the thin-film rather than in its internal body. In the following paragraphs, we provide the details of the uniform and pillared thin-film investigations.

In Chapter 4, lattice dynamics was utilized to model the wave propagation of silicon thin-films across various thicknesses. The resulting dispersion exhibited traits of plate-like motion which is particularly visible in the acoustic branches at low thicknesses. Due to the 2D nature of the material, the thermal conductivity formulation was modified to incorporate the finiteness in the out of plane direction. The thermal conductivity for several film thicknesses were acquired empirically and used to fit the phonon scattering parameters. The thermal conductivity of the thin-film was computed in three ways: 1) with bulk dispersion (i.e., a primitive unit cell with just six branches) and bulk phonon scattering parameters, 2) with bulk dispersion and thickness adjusted thin-film scattering parameters and finally 3) with supercell thin-film dispersion and thickness adjusted thin-film scattering parameters. It was found that incorporating thickness-dependent scattering parameters led to better predictions of thermal conductivity with further insights into the specific mechanisms which impact thermal transport. Upon incorporating the full dispersion, there was a significant improvement in the prediction, especially for lower temperatures and in the thin-films of ~15-20nm or lower in thickness.

In chapter 5, the work with uniform thin-films was expanded to include periodic features to reduce the thermal conductivity. It was determined that placing pillars on the top surface of the thin-film was more advantageous then creating a 2D NPC by punching holes though thin-film due to uncertainties of the phonons and electrons interactions with the void surfaces. More importantly, including pillars at the nanoscale enables a new class of materials called *nanoscale phononic metamaterials* which utilizes local

resonators to manipulate the propagation of phonon waves at subwavelength frequencies. Upon utilizing lattice dynamics to calculate dispersion, unique branches appeared which were flat and low in frequency; these are attributed to the local resonating motion of the pillars. The thermal conductivity calculations found that the presence of the pillars led to a ~50% reductions in thermal conductivity. The computational limitations of lattice dynamics prevent this pillar study from extending beyond a film thickness of ~3nm; a size too small for practical manufacturing capabilities. As a result, a finite element formulation was used to model thin-films with a thickness of ~50nm. It was found that certain finite element mesh resolutions adequately captured the nanoscale effects and converged with the lattice dynamics formulation. The finite-element prediction of the thermal conductivity with the pillars included was consistent with the lattice dynamics model despite the thicker thin-film. The thermal conductivity reduction in the 50nm-thick NPMs (predicted by the finite element models) improved as the height and the density of the pillars were increased. In the case where pillars were present on both sides of the thin-film, a further reduction to 0.35 was of the nominal thin-film value was noted.

6.2 Outlook and Future Research

The idea of incorporating nanostructured materials into thermoelectrics has led to a global resurgence in the perusal of high efficiency solid state energy conversion. The record breaking values of *ZT* reported for silicon nanowires and thin-films holds promise that thermoelectrics may soon be economical and integrated into the commercial industry. The final hurdle that still lies ahead, however, is the challenge of integrating these nanostructured devices into a medium that provides efficient energy conversion, but that is also practical, robust and reliable. Upon engineering materials with desired *ZT* levels, the focus needs to shift into incorporating these features into practical material and device systems that can be easily manufactured.

One of the unique aspects of the work performed in this dissertation is the calculation of full supercell dispersion via lattice dynamics for the different unit cell geometries considered. It was found that incorporating every dispersion branch led to a more accurate depiction of the thermal conductivity of the material. One obstacle however is the limiting connection between the maximum unit cell size that can be analyzed and the computational resources available. In this dissertation, unit cells on the length scales of ~50nm were desired (for practical manufacturing purposes), however the sheer number of atoms involved at this scale limited the size to >5nm. The remedy presented utilized finite element analysis, which was somewhat effective in providing an indication of the phenomenological response, yet it certainly does not capture atomic-scale effects. Future work should focus on the development of novel multi-scale modeling techniques that would allow us to capture the benefits of lattice dynamics and obtaining the full dispersion of an atomic-scale supercell with available computational resources.

7 BIBLIOGRAPHY

Ashcroft N. W. and Mermin N. D., Solid State Physics, (*Saunders College Publishing,* Fort Worth, Texas 1976).

Asheghi M., Touzelbaev M. N., Goodson K. E., Leung Y. K. and Wong S. S., Temperature-Dependent Thermal Conductivity of Single-Crystal Silicon Layers of SOI Substrates, *J. of Heat Trans.*, *ASME* **30**, 30 (1998).

Asheghi M., Leung Y. K., Wong S. S. and Goodsoon K. E., Phonon-Boundary Scattering in Thin silicon Layers, *Appl. Phys. Lett.*, **71**, 1798 (1997).

Balandin A. A. and Wang K. L., Significant Decrease of the Lattice Thermal Conductivity Due to Phonon Confinement in a Free-Standing Semiconductor Quantum Well, *Phys. Rev. B*, **58**, 1544 (1998).

Balandin A., Thermal Properties of Semiconductor Low-Dimensional Structures, *Phys. Low-Dimens. Str.*, **1–2,** 1 (2000).

Balandin A. A., Lazarenkova O. L. and Boechat R. T., Thermoelectric Phonon Stop Band Materials, *Proceedings of 22nd International Conference on Thermoelectrics (ICT'22), IEEE* **03TH8726**, 399, La Grand-Motte, France, (2003).

Balandin A. A., Nanophononics: Phonon Engineering in Nanostructures and Nanodevices, *J. Nanosci. Nanotechnol.*, **5**, 1015 (2005).

Bilal O. R. and Hussein M. I., Topologically Evolved Phononic Material: Breaking the World Record in Band Gap Size, *Proc. of SPIE*, **8269**, 826911-1 (2011).

Bloch F., Zeifschrift für Physik, **52**, 555. (1928).

Brillouin L., Wave Propagation in Periodic Structures, (*2nd Ed., Dover Publications Inc,* New York, New York 1953).

Brizard, A. J., An Introduction to Lagrangian Mechanics, (*World Scientific Publishing Company*, Singapore, 2008).

Born M. and von Karman T., Über Schwingungen in Raumgittern, *Phys. Z.*, **13**, 297 (1912).

Boukai A. I., Bunimovich Y., Tahir-Kheli J., Yu J-K., Goddard III W. A. and Heath J. R., Silicon Nanowires as Efficient Thermoelectric Materials, *Nature Lett.*, **451**, 168 (2008).

Bux S. K., Nanostructured Bulk Silicon as an Effective Thermoelectric Material, *Adv. Funct. Mater.*, **19**, 2445 (2009).

Callaway J., Model for lattice Thermal Conductivity at Low Temperatures, *Phys Rev.*, **113**, 1046 (1959).

Cao, J. X., Yan, X.H., Xiao, Y., Tang, Y. and Ding, J. W., "Exact Study of Lattice Dynamics of Single-Walled Carbon Nanotubes", *Phys. Rev. B*, **67**, 045413 (2003).

Cleland N., Schmidt D. R. and Yung C. S., Thermal Conductance of Nanostructured Phononic Crystals, *Phys. Rev. B*, **64**, 172301 (2001).

Chantrenne P., Barrat J. L., Blase X. and Gale J. D., An Analytical Model for the Thermal Conductivity of Silicon Nanostructures, *J. Appl. Phys.*, **97**, 104318 (2005).

Chen G., Thermal Conductivity and Ballistic-Phonon Transport in the Cross-Plane Direction of Superlattices, *Phys. Rev. B*, **57**, 14958 (1998).

Chen G., Heat Conduction in Nanostructures, *Int. Jour. Therm. Sci.*, **39**, 471 (2000).

Chen G., Particularities of Heat Conduction in Nanostructures, *J. Nanoparticle Research*, **2**, 199 (2000).

Chen G., Dresselhaus M. S., Dresselhaus G., Fleurial J. P. and Caillat T., Recent Developments in Thermoelectric Materials, *Int. Mater. Rev.*, **48**, 45 (2003).

Chen G., Narayanaswamy A. and Dames C., Engineering Nanoscale Phonon and Photon Transport for Direct Energy Conversion, *Superlattice. Microst.*, **35**, 161 (2004).

Chen G., Nanoscale Energy Transport and Conversion, (*Oxford University Press*, New York, 2005).

Christensen J., Fernandez-Dominguez A. I., de Leon-Perez F., Martin-Moreno L. and Garcia-Vidal F. J., Collimation of Sound Assisted by Acoustic Surface Waves, *Nat. Phys.*, **3**, 851 (2007).

Cocemasov A. I. and Nika D. L., Phonons and Phonon Conductivity in Silicon Nanolayers, *J. Nanoelectronics and Optoelectronics*, **7**, 370 (2012).

Cowley, R. A., "Lattice Dynamics and Phase Transitions of Strontium Titanate," *Phys. Rev.*, **134**, A981 (1964).

Davis B.L. and Hussein M.I., A Three-Dimensional Lumped Parameter Model of Nanoscale Phononic Crystals, *Proceedings of 22nd ASME Biennial Conference on Mechanical Vibration and Noise*, San Diego, California (2009).

Davis B. L. and Hussein M. I., Thermal Characterization of Nanoscale Phononic Crystals using Supercell Lattice Dynamics, *AIP Advances*, **1**, 041701 (2011).

Davis B. L., Tomchek A. S., Flores E. A., Liu L. and Hussein M. I., Analysis of Periodicity Termination in Phononic Crystals, *Proceedings of 2011 ASME International Mechanical Engineering Congress and R&D Expo* IMECE2011-**65666**, 973, Denver, Colorado (2011).

Debye P., Zur Theorie der spezifischen Waerme, *Annalen der Physik*, **39**, 789 (1912).

Dolling G., Inelastic Scattering of Neutrons in Solids and Liquids, edited by S. Ekland, Vol. **II**, 37 (IAEA, Vienna, 1963).

Dove M. T., Introduction to Lattice Dynamics, (*Cambridge University Press,* Cambridge, 1993).

Dresselhaus M. S., Chen G., Tang M., Yang R., Lee H., Wang D., Ren Z., Fleurial J. and Gogna P., New Directions for Low-Dimensional Thermoelectric Materials, *Adv. Mater.*, **19**, 1043 (2007).

Dugas, R., History of Mechanics, (*Edition du Griffon*, Neuchatel, Switzerland, 1955).

Eichenfield M., Chan J., Camacho R. M., Vahala K. J. and Painter O., Optomechanical Crystals, *Nature*, **462**, 78 (2009).

Einstein A., Annalen der Physik, **22**, 180 (1907).

El-Kady I., Olsson III R. H. and Fleming J. G., Phononic Band-Gap Crystals for Radio Frequency Communications, *Appl. Phys. Lett.*, **92**, 233504 (2008).

Frazier, J. F. and Hussein, M. I., "Bloch-Theory-Based Analysis of Damped Phononic Materials," *Proceedings of the ASME 2011 International Mechanical Engineering Congress & Exposition* IMECE2011-**65662**, 1, Denver, Colorado (2011).

General Utility Lattice Program, https://www.ivec.org/gulp.

Gillet J. N., Chalopin Y. and Volz S., Atomic-Scale Three-Dimensional Phononic Crystals With a Very Low Thermal Conductivity to Design Crystalline Thermoelectric Devices, *J. of Heat Trans.*, *ASME* **131**, 043206 (2009).

Gillet J. N., Marked Thermal Exaltation in Hybrid Thin Membranous Nanomaterials Covered by Stretched Nanodots for Thermoelectrics and Passive Cooling, *Appl. Mat & Interfaces*, **2**, 3486 (2010).

Goldsmid H. J. and Douglas R. W., The Use of Semiconductors in Thermoelectric Refrigeration, *Brit. J. Appl. Phys.*, **5**, 386 (1954).

Goodson K. E. and Ju, Y. S., Heat Conduction in Novel Electronic Films, *Annu. Rev. Mater. Sci.*, **29**, 261 (1999).

Gorishnyy T., Ullal C. K., Maldovan M., Fytas G. and Thomas E. L., Hypersonic Phononic Crystals, *Phys. Rev. Lett.*, **94**, 115501 (2005).

Graff, K., Wave Motion in Elastic Solids, (*Dover Publications INC., Dover Edition*, Mineola, New York 1991).

Green, M. S., Markoff Random Processes and the Statistical Mechanics of Time-Dependent Phenomena. II. Irreversible Process in Fluids, *J. Chem. Phys*, **22**, 398 (1954).

Harman T. C., Walsh M. P., LaForge B. E. and Turner G. W., J. Nanostructured Thermoelectric Materials, *Electron. Mater.*, **34**, L19 (2005).

He Y. P., Donadio D., Lee J. H., Grossman , J. C. and Galli G., Thermal Transport in Nanoporous Silicon: Interplay Between Disorder at Mesocopic and Atomic Scales, *ACS Nano*, **5**, 1839 (2011).

Hepplestone S. P. and Srivastava G. P., Lattice Dynamics of Silicon Nanostructures, *Nanotechnology*, **17**, 3288 (2006).

Hepplestone, S. P. and Srivastava, G. P., "Hypersonic Modes in Nanophononic Semiconductors," Phys. *Rev. Letts.*, **101**, 105502 (2008).

Hladky-Hennion A. C., Allan G. and Billy M. D., Localized Modes in a One-Dimensional Diatomic Chain of Coupled Spheres, *J. Appl. Phys.*, **98**, 054909 (2005).

He Y. P., Donadio D., Lee J. H., Grossman , J. C. and Galli G., Thermal Transport in Nanoporous Silicon: Interplay Between Disorder at Mesocopic and Atomic Scales, *ACS Nano*, **5**, 1839 (2011).

Hicks L. D. and Dresselhaus M. S., Effect of Quantum-Well Structures on the Thermoelectric Figure of Merit, *Phys. Rev. B*, **47**, 12727 (1993).

Ho C. Y., Powell R.W. and Liley P.E., Thermal Conductivity of the Elements *J. Phys. Chem. Ref. Data*, **1**, 279 (1972).

Hochbaum A. I., Chen R., Delgado R. D., Liang W., Garnett E C., Najarian M., Majumdar A. and Yang P., Enhanced Thermoelectric Performance of Rough Silicon Nanowires, *Nature Lett.*, **45**, 163 (2008).

Holland M. G., Analysis of Lattice Thermal Conductivity, *Phys. Rev.*, **132**, 2461 (1963).

Hopkins P. E., Reinke C. M., Su M. F., Olsson III R. H., Shaner E. A., Leseman Z. C., Serrano J. R., Phinney L. M. and El-Kady I., Reduction in the Thermal Conductivity of Single Crystalline Silicon by Phononic Crystal Patterning, *Nano Lett.*, **11**, 107 (2011).

Hooke R., De Potentia Restitutiva, London, (1678).

Horton G. K., Selected Topics in Lattice Dynamics: A Critical Review (Including Breathers), *Chaos*, **13**, 667 (2003).

Horton, G. K. and Maradudin, A. A., Dynamical Properties of Solids, **1**, 1-82, (*Elsevier*, New York, New York 1974).

Hussein M. I., Hulbert G. M. and Scott R. A., Dispersive Elastodynamics of 1D Banded Materials and Structures: Analysis, *J. Sound Vib.*, **289**, 779 (2006).

Hussein M. I., Hulbert G. M. and Scott R. A., Dispersive Elastodynamics of 1D Banded Materials and Structures: Design, *J. Sound Vib.*, **307**, 865 (2007).

Hussein, M.I., Hamza, K., Hulbert, G. M. and Saitou, K., "Optimal Synthesis of 2D Phononic Crystals for Broadband Frequency Isolation," *Waves in Random and Complex Media*, **17**, 491 (2007).

Hussein M. I., Reduced Bloch Mode Expansion for Periodic Media Band Structure Calculations, *Proc. R. Soc. A*, **465**, 2825 (2009).

Incropera F. P. and DeWitt D. P., Fundamentals of Heat and Mass Transfer, (*Wiley*, Hoboken, New Jersey, 2002).

Jensen J.S., Phononic Band Gaps and Vibrations in One- and Two-Dimensional Mass-Spring Structures, *Jour. Sound and Vib.*, **266**, 1053 (2003).

Kern, G., Kresse, G. and Hafner, J., "Ab Initio Calculation of the Lattice Dynamics and Phase Diagram of Boron Nitride,' *Phys. Rev. B*, **59**, 8551 (1999).

Khelif A., Djafari-Rouhani B., Vasseur J. O., Deymier P. A., Lambin Ph. and Dobrzynski L., Transmissivity Through Straight and Stublike Waveguides in a Two-Dimensional Phononic Crystal, *Phys. Rev. B*, **65**, 174308 (2002).

Khelif A., Choujaa A., Benchabane S., Djafari-Rouhani B. and Laude V., Guiding and Bending of Acoustic Waves in Highly Confied Phononic Crystal Waveguides, *Appl. Phys. Lett.*, **84**, 4400 (2004).

Khitun A., Balandin A., Liu J. L. and Wang K. L., The effect of the long-range order in a quantum dot array on the in-plane lattice thermal conductivity, *Superlattice Microst.*, **30**, 1 (2001).

Kittel C., Introduction to Solid State Physics, 8th Edition, (*Wiley*, New York 2005).

Kleinke H., New Bulk Materials for Thermoelectric Power Generation: Clathrates and Complex Antimonides, *Chem. Mater.*, **22**, 604 (2010).

Klemens P.G., The Thermal Conductivity of Dielectric Solids at Low Temperatures (Theoretical), *Proc. R. Soc. Lond. A*, **208**, 108 (1951).

Klemens P.G., The Scattering of Low-Frequency Lattice Waves by Static Imperfections, *Proc. Phys. Soc. A*, **68**, 1113 (1955).

Kubo, R., Statistical-Mechanical Theory of Irreversible Processes. I. General Theory and Simple Applications to Magnetic and Conduction Problems, *J. Phys. Soc. Jpn.*, **12**, 570 (1957).

Kushwaha M. S., Halevi P., Dobrzynski L. and Djafari-Rouhani B., Acoustic Band Structure of Periodic Elastic Composites, *Phys. Rev. Lett.*, **71**, 2022 (1993).

Lagrange, J.L., Mechanique Analytique, (*Chez la Veuve Desaint*, Paris 1788).

Laundry E. S., Hussein M. I. and McGaughey A. J., Complex Superlattice Unit Cell Designs for Reduced Thermal Conductivity, *Phys. Rev. B*, **77**, 184302 (2008).

Lee E. H., Yang and Wei H., On Waves in Composite Materials with Periodic Structure, *SIAM J. of Appl. Mathematics*, **25**, 492 (1973).

Li D., Wu Y., Kim P., Shi L., Yang P. and Majumdar A., Thermal Conductivity of Individual Silicon Nanowires, *Appl. Phys. Lett.*, **83**, 14 (2003).

Li J., Liu W., Zhao L. and Zhou M., High-Performance Nanostructured Thermoelectric Materials, *NPG Asia Mater.*, **2**, 152 (2010).

Li X. F., Ni X., Feng L. A., Lu M. H., He C. and Chen Y. F., Tunable Unidirectional Sound Propagation through a Sonic-Crystal-Based Acoustic Diode, *Phys. Rev. Lett.*, **106**, 084301 (2011).

Li X.P., Chen G., Allen P.B. and Broughton J.Q, Energy and Vibrational spectrum of the Si(111) (7x7) Surface from Empirical Potentials, *Phys. Rev. B*, **38**, 3331 (1988).

Liu Z., Zhang Z., Mao Y., Zhu Y. Y., Yang Z., Chan C. T. and Sheng P., Locally Resonant Sonic Materials, *Science*, **289**, 5485 (2000).

Liu W. and Asheghi M., Phonon-Boundary Scattering in Ultrathin Single-Crystal Silicon Layers, *Appl. Phys. Lett.*, **84**, 3819 (2004).

Liu W. and Asheghi M., Thermal Conduction in Ultrathin Pure and Doped Single-Crystal Silicon Layers at High Temperatures, *J. Appl. Phys.*, **98**, 123523 (2005).

Lennard-Jones J. E., On the Determination of Molecular Fields, *Proc. R. Soc. Lond. A*, **106**, 738 (1924).

Maradudin, A. A., Montroll, E.W. and Weiss, G. H., Theory of Lattice Dynamics in the Harmonic Approximation, (Academic Press, New York, New York 1963).

Maldovan M., Micro to Nano Scale Thermal Energy Conduction in Semiconductor Thin Films, *J. Appl. Phys.*, **110**, 034308 (2011).

McGaughey A. J. H. and Kaviany M., Quantitative Validation of the Boltzmann Transport Equation Phonon Thermal Conductivity Model under the Single-Mode Relaxation Time Approximation, *Phys. Rev. B*, **69**, 094303 (2004).

McGaughey A. J. H., Hussein M. I., Landry E. S., Kaviany M. and Hulbert G. M., Phonon Band Structure and Thermal Transport Correlation in a Layered Diatomic Crystal, *Phys. Rev. B*, **74**, 104304 (2006).

McGaughey A. J. H. and Kaviany M., Phonon Transport in Molecular Dynamics Simulations: Formulation and Thermal Conductivity Predictions, *Adv. in Heat Trans.*, **39**, 169 (2006).

Mead D. J., Wave Propagation in Continuous Periodic Structures: Research Contributions from Southampton 1964-1995, *Jour. Sound Vib.*, **190**, 495 (1996).

Mingo N., Calculation of Si Nanowire Thermal Conductivity using Complete Phonon Dispersion Relations, *Phys. Rev. B*, **68**, 113308 (2003).

Minnich A. J., Dresselhaus M. S, Ren Z. F. and Chen G., Bulk Nanostructured Thermoelectric Materials: Current Research and Future Prospects, *Energ. Environ. Sci.*, **2**, 466 (2009).

Mohammadi S., Eftekhar A. A., Hunt W. D. and Adibi A., High-Q Micromechanical Resonators in a Two-Dimensional Phononic Crystal Slab, *Appl. Phys. Lett.*, **94**, 051906 (2009).

Newton I., Naturalis Principia Mathematica, Book **II**, (1686).

Nika D. L., Zincenco, N. D. and Pokatilov E. P., Engineering of Thermal Fluxes in Phonon Mismatched Heterostructures, *J. Nanoelectronics and Optoelectronics*, **4**, 180 (2009).

Nolas G. S., Morelli D. T. and Tritt T. M., Skutterudites: A Phonon-Glass-Electron Crystal Approach to Advanced Thermoelectric Energy Conversion Applications, *Annu. Rev. Mater. Sci.*, **29**, 89 (1999).

Peierls R., Zur kinetischen Theorie der Wärmeleitung in Kristallen, *Annalen der Physik*, **395**, 1055 (1929).

Pennec Y., Djafari-Rouhani B., Larabi H., Vasseur J. O. and Hladky-Hennion A. C., Low-Frequency Gaps in a Phononic Crystal Constituted of Cylindrical Dots Deposited on a Thin Homogenous Plate, *Phys. Rev. B*, **78**, 104105 (2008).

Pichanusakorn P. and Bandaru P., Nanostructured Thermoelectrics, *Mater. Sci. & Engr. R*, **67**, 19 (2010).

Poisson S. D., *Ann. Chim. Phys*. (eds Gay-Lussac L. J. & Arago F.), **36**, 384 (1827).

Rayleigh J.W.S., On the Maintenance of Vibrations by Forces of Double Frequency, and on the Propagation of Waves through a Medium Endowed with a Periodic Structure, *Philosophical Magazine*, **24**, 145 (1887).

Robillard J. F., Muralidharan K., Bucay J., Deymier P. A., Beck W. and Barker D., Phononic Metamaterials for Thermal Management: An Atomistic Computational Study, *Chinese J. Phys.*, **49**, 448 (2011).

Shanno D. F., Conditioning of Quasi-Newton Methods for Function Minimization, *Math. Comput.*, **24**, 647 (1970).

Sigalas M. and Economou E. N., Band Structure of Elastic Waves in Two Dimensional Systems, *Solid State Commun.*, **86**, 141 (1993).

Sigalas M. M., Defect States of Acoustic Waves in a Two-Dimensional Lattice of Solid Cylinders, *J. Appl. Phys.*, **84**, 3026 (1998).

Sigalas M. M. and García N., Theoretical Study of Three Dimensional Elastic Band Gaps with the Finite-Difference Time-Domain Method, *J. Appl. Phys.*, **87**, 3122 (2000).

Srivastava G. P., The Physics of Phonons, (*Adam Hilger*, Bristol, 1990).

Snyder G. J. and Toberer E. S., Complex Thermoelectric Materials, *Nat. Mater.*, **7**, 105 (2008).

Stillinger F. H. and Weber T. A., Computer Simulation of Local Order in Condensed Phase of Silicon, *Phys. Rev. B*, **31**, 5262 (1985).

Tamura S., Tanaka Y. and Maris H., Phonon Group Velocity and Thermal Conduction in Superlattices, *Phys. Rev. B*, **60**, 2627 (1999).

Tang J., Wang H-T., Lee D. H., Fardy M., Huo Z., Russell T. P. and Yang P., Holey Silicon as an Efficient Thermoelectric Material, *Nano Lett.*, **10**, 4279 (2010).

Thomas J. A., Turney J. E., Iutzi R. M., Amon C. H. and McGaughey A. J. H., Predicting Phonon Dispersion Relations and Lifetimes from the Spectral Energy Density *Phys. Rev. B*, **81**, 081411R (2010).

Thomson W.T., Transmission of Elastic Waves through a Stratified Solid Medium, *Jour. Appl. Phys.*, **21**, 89 (1950).

Telkes M., The Efficiency of Thermoelectric Generators, *J. Appl. Phys.*, **18**, 1116 (1947).

Tersoff J., New Empirical Approach for the Structure and Energy of Covalent Systems, *Phys. Rev. B*, **37**, 6991 (1988).

Tersoff J., Empirical Interatomic Potential for Silicon with Improved Elastic Properties, *Phys. Rev. B*, **38**, 9902 (1988).

Turney, J. E., Laundry, E. S. and McGaughey, A. J. H., "Predicting Phonon Properties and Thermal Conductivity from Anharmonic Lattice Dynamics Calculations and Molecular Dynamics Simulations," *Phys. Rev. B*, **79**, 064301 (2009).

Turney J. E., Mcgaughey A. J. H. and Amon C. H., In-Plane Phonon Transport in Thin Films, *Journal of Applied Physics*, **107**, 024317 (2010).

Torrent D. and Sánchez-Dehesa J., Acoustic Cloaking in two Dimensions: A Feasible Approach, *New J. Phys.*, **10**, 063015 (2008).

Torres M., Montero de Espinosa F. R., García-Pablos D. and García N., Sonic Band Gaps in Finite Element Media: Surface States and Localization Phenomena in Linear Point Defects, *Phys. Rev. Lett.*, **82**, 3054 (1999).

Venkatasubramanian R., Siivola E., Colpitts T. and O'Quinn B., Thin-Film Thermoelectric Devices with High Room-Temperature Figures of Merit, *Nature*, **413**, 597 (2001).

Vineis C. J., Shakouri A., Majumdar A. and Kanatzidis M. G., Nanostructured Thermoelectrics: Big Efficiency Gains from Small Features, *Adv. Mater.*, **22**, 3970 (2010).

Vining C. B., Desperately Seeking Silicon, *Nature*, **451**, 132 (2008).

Wei-Wei, Z., Hong ,Y., Shuang-Ying, L. and Qing-An, H., Modeling of the Elastic Properties of Crystalline Silicon using Lattice Dynamics, *J. Phys. D: Appl. Phys.*, **44** 335401 (2011).

Wu T. T., Huang Z. G., Tsai T. C. and Wu T. C., evidence of Complete Band Gap and Resonances in a Plate with Periodic Stubbed Surface, *Appl. Phys. Lett.*, **93**, 111902 (2008).

Yang S., Page J. H., Liu Z., Cowan M. L., Chan C. T. and Sheng P., Focusing of Sound in a 3D Phononic Crystal, *Phys. Rev. Lett.*, **93**, 24301 (2004).

Yu J., Mitrovic S., Tham D., Varghese J. and Heath J., Reduction of Thermal Conductivity in Phononic Nanomesh Structures, *Nat. Nanotechnol.*, **5**, 718 (2010).